NTNU – Trondheim
Norwegian University of
Science and Technology

Stability of Conductive Carbon Additives for High-voltage Li-ion Battery Cathodes

Benedicte Eikeland Nilssen

Chemical Engineering and Biotechnology
Submission date: June 2014
Supervisor: Ann Mari Svensson, IMTE
Co-supervisor: Ahmet Oguz Tezel, IMT

Norwegian University of Science and Technology
Department of Materials Science and Engineering

Declaration

I declare that the work described in this report has been performed independently and in accordance with the rules and regulations for examinations at the Norwegian University of Science and Technology, NTNU.

June 30th 2014, Trondheim

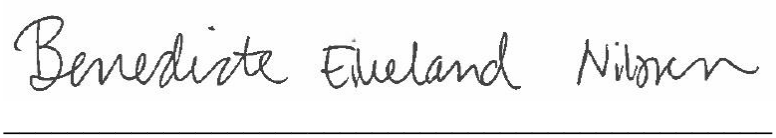

Benedicte Eikeland Nilssen

Preface

This master's thesis has been written in the course TMT4900 Materials Chemistry and Energy Technology, Master Thesis, spring 2014. The report is the final submission to complete the Master's Degree Program in Chemical Engineering and Biotechnology at the Norwegian University of Science and Technology, NTNU. The completed work is a part of the ongoing battery research at the Department of Materials Science and Engineering, and also an extension of a project conducted by the author in the course TMT4500 Materials Technology, Specialization Project, fall 2013. That project resulted in a report with the following title: "Stability of conductive carbon additive in high voltage lithium ion battery".

Most of the experiments and analysis provided in this report have been conducted by the author with the exception of Raman spectroscopy analysis, which was conducted by Marita Sætnan. In order to be able to present some of the results, a MatLab code programmed by Øyvind Ulvin Halvorsen has been used, and he needs to be acknowledged for that.

I would like to express my gratitude to my main supervisor Professor Ann Mari Svensson at NTNU for valuable guidance, feedback and for being really caring. Furthermore, I want to thank my co-supervisor PhD candidate Ahmet Oguz Tezel for lab advices and informative discussions. Senior Engineer Julian R. Tolchard deserves so many thanks for taking so much of his time to help me with the *in situ* X-ray diffraction measurements; we made it work in the end. In addition, I want to thank Staff Engineer Magnus Bentzen Følstad, Engineer Pei Na Kui and Scientist Luis César Colmenares Rausseo at SINTEF, for being helpful with all sorts of practical issues and potentiostat problems. I would also like to thank all the people making up the battery group for their feedback and always being very willing to help.

Last, but definitely not least, I have to send some really big hugs to my lovely friends and family for being such a great motivation and support in this period; you all have contributed to keep my "human batteries" being charged. Thank you!

Abstract

Conductive carbon additives are important constituents of the current state-of-the-art Li-ion battery cathodes, as the traditional active cathode materials are characterized by too low electronic conductivities. In high-voltage Li-ion batteries, these additives are subject for anion intercalation and electrolyte oxidation, which might cause changes in the conductive carbon network in the cathode, and hence the overall cycling performance of the electrode.

This thesis has focused on study the stability of three types of carbon additives operating at high voltages. Materials included were two conventional types of conductive additives, graphite, KS6, and carbon black, Super P Li, both provided from TIMCAL. In addition, a multilayer graphene powder, Graphene AO-2, provided from Graphene Supermarket has been investigated. The powder properties, size, shape and structure, were studied in a scanning electron microscope and by powder X-ray diffraction. Electrodes from these materials were cycled galvanostatically and with cyclic voltammetry to reveal their high-voltage behaviour, with respect to the two above mentioned electrochemical processes. More detailed investigations of anion intercalation in KS6 and Graphene AO-2 were conducted by *in situ* X-ray diffraction measurements and scanning electron microscopy.

For cycling in 30:70 vol% EC/DMC 1 M $LiPF_6$ to a voltage of 4.7 V vs. Li^+/Li, the results showed that Super P Li can be considered as the most stable conductive additive. At 4.7 V vs. Li^+/Li, both KS6 and Graphene AO-2 are electrochemically active, while Graphene AO-2 displays a more reversible behavior, and are more stable than KS6. For even higher operation potential, 5.0 V vs. Li^+/Li, Graphene AO-2 showed the least stable behavior of the three materials, due to large degree of electrolyte oxidation, unstable anion intercalation upon continuous cycling, and the suggestions of structural degradation of the electrode. However, a small increase in the electrolyte stability window was shown with Graphene AO-2 when changing to a more viscous electrolyte (1:1 vol% EC/DMC 1 M $LiPF_6$) or adding an anion receptor (tris(hexafluoroisopropyl)borate) to the electrolyte. The anion intercalation in KS6 was observed to form staged phases, starting at 4.83 V vs. Li^+/Li. The electrode structure was suggested to be affected in a smaller extent compared to Graphene AO-2. In addition, less electrolyte was oxidized at the KS6 electrode surface, compared to the two other materials. However, the film formed on the Super P Li electrodes did not seem to affect the carbon negatively, because stable anion intercalation was observed upon continuous cycling. Indicating that Super P Li was not strongly affected by the intercalation process.

Sammendrag

Ledende karbonadditiver utgjør en viktige bestanddel i katoden i "state-of-the-art" Li-ion batteri, da de typiske aktive katodematerialene karakteriseres med veldig lav elektrisk ledningsevne. I høy-spenning Li-ion batterier vil disse additivene inngå i de to elektrokjemiske prosessene, anioninterkalasjon og elektrolyttoksidasjon. Dette kan føre til endringer i det elektriske ledende karbonnettverket i katoden slik at den totale ytelsen til elektroden reduseres.

Denne avhandlingen har fokusert på å studere tre typer karbonadditiver som opererer ved høye spenninger. De materialene som ble inkludert i studien var de to typiske karbonadditivene grafitt, KS6, og "carbon black", Super P Li, begge produsert av TIMCAL. I tillegg ble også ett grafenpulver, Graphene AO-2, levert fra Graphene Supermarket, studert. Pulveregenskaper, størrelse, form og krystallstruktur, ble undersøkt med scanning elektronmikroskop og ved røntgendiffraksjon. Elektroder av disse karbonmaterialene ble deretter syklet galvanostatisk og analysert ved syklisk voltammetri, for å avdekke i hvor stor grad karbonmaterialene ble påvirket av de nevnte elektrokjemiske prosessene. For å oppnå en bedre forståelse av de strukturelle endringene knyttet til interkalasjonen av anioner, ble KS6 og Graphene AO-2 også analysert ved *in situ* røntgendiffraksjon og ved bruk av scanning elektronmikroskop.

Resultatene viser at Super P Li er den mest stabile av de tre typene additiver opp til et potensial lik 4.7 V vs. Li^+/Li, når følgende elektrolytt ble benyttet, 30:70 vol% EC/DMC 1 M $LiPF_6$. Ved samme potensial ble det observert at både KS6 og Graphene AO-2 var elektrokjemisk aktive, hvor Graphene AO-2 viste en mer reversible oppførsel og dermed også større grad av stabilitet. Da cellespenningen ble økt til 5.0 V vs. Li^+/Li, var det derimot Graphene AO-2 som var minst stabil, grunnet stor grad av elektrolyttoksidasjon på elektrodeoverflaten, lite reversibilitet, samt antydninger til stor strukturell ødeleggelse. Ved å benytte en mer viskøs elektrolytt (1:1 vol% EC/DMC 1 M $LiPF_6$), eller ved å tilsette anionreseptor (tris(hexafluoroisopropyl)borat) ble det observert en liten forbedring i stabiliteten til elektrolytten i kombinasjon med Graphene AO-2 elektrode. Resultatene antyder også endringer i KS6 elektrodestrukturen, men ikke i samme grad som for Graphene AO-2. I tillegg, ble det observert mye mindre elektrolyttoksidasjon på overflaten av KS6 sammenlignet med de to andre materialene. Derimot kan det virke som at filmdannelsen på Super P Li elektrodene resulterte i en stabil anioninteraksjon, og det var ingen tydelige indikasjoner på at elektrodestrukturen ble streket påvirket av interkalasjonen av anioner.

Table of contents

List of abbreviations

AR	Anion receptor
BET	Brunauer-Emmet-Teller (specific surface area measurement technique)
CE	Counter electrode
C_{eff}	Coulombic efficiency
CV	Cyclic voltammetry
DMC	Dimethyl carbonate
EC	Ethylene carbonate
EMS	Ethyl methyl sulfone
EV	Electric vehicle
FWHM	Full-width half-maximum
HEV	Hybrid electric vehicle
ICL	Irreversible capacity loss
NMP	1-methyl-2-pyrrolidone
OCV	Open circuit voltage
PVDF	Polyvinylidene fluoride
REF	Reference electrode
SEI	Solid electrolyte interface
SEM	Scanning electron microscopy
THFIPB	Tris(hexafluoroisopropyl)borate
WE	Working electrode
XRD	X-ray diffraction

List of symbols

Symbol	Unit	Designation
β	[rad]	Value of full-width half-maximum (FWHM)
θ_{00N}	[°]	Scattering angle related to (002) planes in a superstructure obtaining a stage index N
θ_{00N+1}	[°]	Scattering angle for additional diffraction peak in a superstructure obtaining a stage index N
θ_{hkl}	[°]	Scattering angle
λ	[nm]	X-ray wavelength
Ω	[Hz]	Angular frequency (=2πf where f is given in Hz)
C	[F]	Capacitance
C_{eff}	[%]	Coulombic efficiency
f	[Hz]	Frequency
j	[-]	Imaginary unit
K	[-]	Shape factor
L_a	[Å]	Crystallite height parallel to basal planes
L_c	[Å]	Crystallite height perpendicular to basal planes
L(hkl)	[Å]	Crystallite height perpendicular to basal planes (for hkl equal 002, 004 or 006)
N	[-]	Order of reflection
n	[-]	Stage index
Z	[Ω]	Impedance
Z''	[Ω]	Imaginary component of impedance
Q_{irr}	[$mAhg^{-1}$]	Charge related to irreversible reactions
Q_{rev}	[$mAhg^{-1}$]	Charge related to reversible reactions

1 Introduction

The lithium-ion battery has been commercially available since 1991, and is the dominating rechargeable battery for many applications. This is primarily related to the high energy density, high operating voltage, reasonable cycling stability and cycle life [1]. Figure 1.1 clearly illustrates the benefits of Li-ion batteries compared to other battery technologies, in terms of energy density. Today, the Li-ion battery has almost completely replaced nickel cadmium batteries and nickel metal hydride batteries in portable electronics [2].

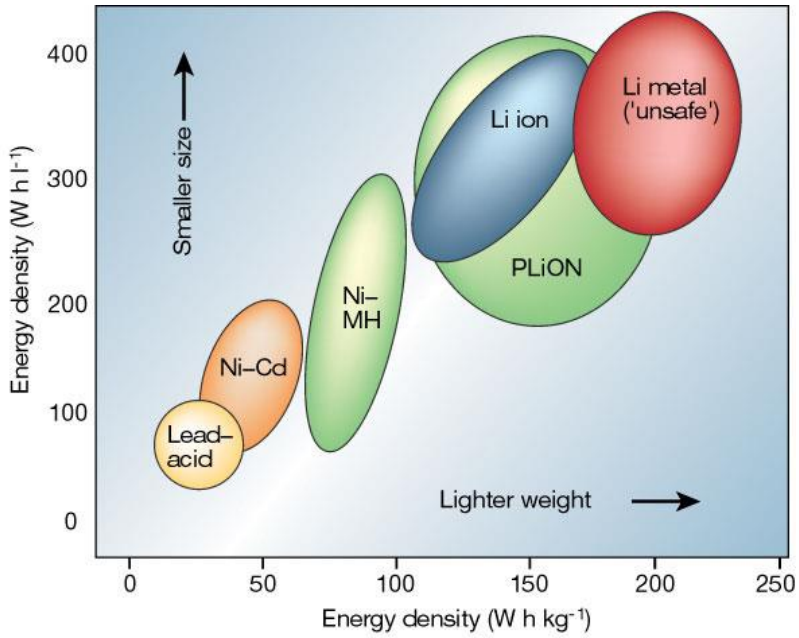

Figure 1.1: Comparison of different battery technologies with respect to their volumetric and gravimetric energy densities [3].

In the last decades, the world has become more globalized and many countries have developed and increased their wealth. This has resulted in a society where portable electronic devices are crucial for everyday life, hence creating a wide variety of markets and applications for Li-ion batteries, such as mobile phones, laptops, etc. However, the development also has some drawbacks that challenge the humanity today. Global warming, climate changes, air pollution; especially in large urban areas, are topics being intensively discussed and attempted to be solved. Rechargeable Li-ion batteries also play a key role in addressing these threats by their use in electric vehicles (EV) and hybrid electric vehicles

(HEV) [4]. Air pollution in large urban areas may actually only be solved by replacing the internal combustion engine cars with sustainable vehicles, like EV and HV [5]. However, the state-of-the-art (SOA) Li-ion batteries need improvement to make the EVs becoming competitive with gasoline cars.

There are great efforts in research and development of the Li-ion battery, where the main commercial goals are e.g. higher lifetime, lower maintenance, low cost, and above all for vehicle traction, higher energy density [6]. In the search of high-energy materials the exploration of high-voltage cathode materials has become an interesting perspective [7], for example the Li-rich layered NMC cathode materials has received a lot of attention, e.g. in the work of Li et al. [8]. In general, these cathode materials are rather poor electrical conductors so they are entirely dependent on a network structure consisting of carbon particles which facilitate fast current flow, hence enchanting the electrode performance. Different types of carbon materials are available on the market, operating well in the SOA Li-ion battery, like conventional graphite and carbon black [2]. However, in a high-voltage cell system, these conductive carbon additives are subject to electrolyte oxidation and anion intercalation. Previous research in the field of high-voltage Li-ion batteries report varying degree of structural changes in the conductive network upon cycling [7, 9-11], which might affect the overall composite cathode performance.

Aim of this work

The aim of this work is to investigate three different candidate materials as carbon conductive additive for high-voltage Li-ion battery cathodes. Two of them are commercially available conductive additives; a fine graphite powder, KS6 as well as a type of carbon black, Super P Li, both provided from TIMCAL. The third material is a multilayer graphene powder, Graphene AO-2 provided from Graphene Supermarket. For the electrochemical characterization, porous electrodes were made from each of the carbon powders. Even though the main purpose of adding carbon to the cathode is to create a conductive network in between the particles of active material, electrodes containing only carbon powder and binder will be studied in this work.

The first part of the study includes characterization of carbon powder properties. Particle morphology and size, and structure, will be assessed using scanning electron microscopy (SEM) and X-ray diffraction (XRD), respectively. The second part deals with

electrochemical testing at high voltages, where the three carbon materials are exposed to the same type of conventional Li-ion battery electrolyte. Reactions upon cycling to high voltages will be investigated in terms of capacity, reversibility and reaction voltages, using galvanostatic cycling (chronopotentiometry) and cycling voltammetry (CV). Further investigations of structural stability related to anion intercalation will be conducted by *in situ* XRD and SEM analysis. The third part deals with electrochemical testing at high voltages, using the same techniques just mentioned, in order to reveal any changes in cell system stability after modifying the electrolyte properties; increased viscosity and addition of an electrolyte additive.

2 Theory

This chapter gives an introduction to the current state-of-the-art Li-ion batteries and the next generation Li-ion batteries. The first section includes a detailed description of the Li-ion cell, intercalation process, and typical cell components; focusing on the conductive carbon additive in the positive electrode. The second section deals with the challenges appearing in the next generation Li-ion battery, with focus on the electrochemical reactions taking place at the cathode operating at high anodic potentials. The third section presents the principles electrochemical impedance spectroscopy (EIS) and XRD.

2.1 Lithium-ion battery technology

In a historical perspective, the first galvanic electrochemical cell was constructed by Alessandro Volta in 1800 [12]. A galvanic cell is characterized by spontaneous reactions in the system when the electrodes are connected, and battery is one type of such a cell. Since the redox reactions take place at two electrodes, which are electrically and spatially separated, chemical energy is directly converted into electrical energy [6]. Batteries are classified in two categories; primary (non-rechargeable) batteries and secondary (rechargeable) batteries. One example of the latter is the Li-ion battery.

2.1.1 Principles of a lithium-ion cell

A Li-ion cell is a complex system which rely on the cooperation of several components during operation, illustrated in Figure 2.1.

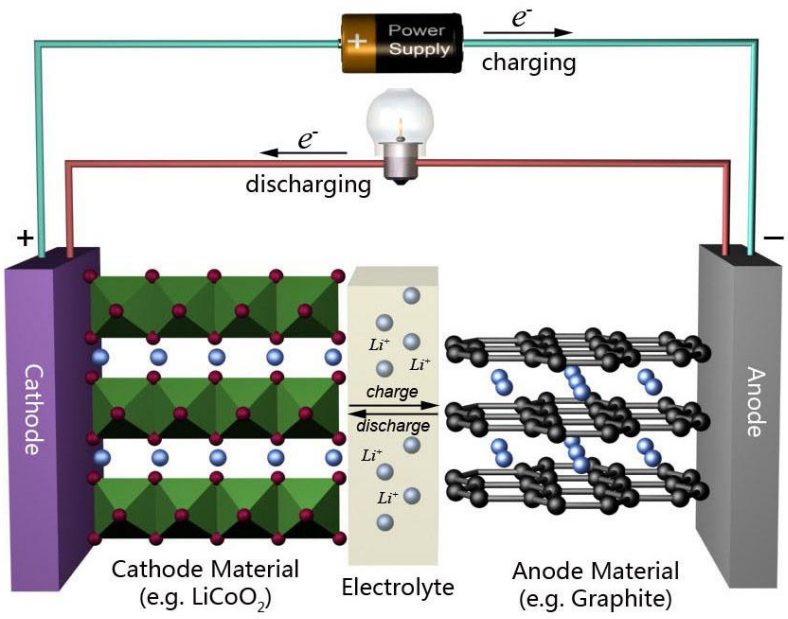

Figure 2.1: Illustration of a lithium-ion cell. The arrows given in the figure indicate the flow of electrons and lithium ions during charge and discharge of the cell [13].

For a conventional Li-ion battery, the cell contains a graphite anode and a cathode made from a lithium transition metal oxide, e.g. lithium cobalt dioxide, $LiCoO_2$ [5]. In addition, carbon is added to both electrodes to improve the electronic conductivity. The current collectors ensure electron transfer between the electrodes and external circuit, and also provide mechanical support to the electrode active layers. Adhesion of the active material on the current collector and the cohesion of the electrode components is achieved by a polymer binder. The electrodes are separated by a separator which allows ion transfer while preventing direct contact between the two electrodes and hence short circuit in the cell [2]. These components are all exposed to an electrolyte normally consisting of a lithium salt in mixed organic solvents [5]. When connecting several of these cells in either series or in parallel, determined by the needs of the equipment they are powering, this make up a rechargeable Li-ion battery [14].

2.1.2 Intercalation process

Like the name implies, the operation of a Li-ion battery is based on an electrochemical process involving Li^+-ions. Other names used for the same system is Li-ion transfer cell, rocking chair battery, swing and shuttlecock [15, 16]. In such a cell there is a transfer of Li^+-ions between the anode and the cathode due to the difference in electrochemical

potentials of lithium in the two electrodes [15]. During charging, the Li^+-ions originating from the lithium metal oxide and migrate through the electrolyte to the anode, while the electrons are transported in the same direction, thus through an external circuit. In order to maintain the charge balance in the cell the anions migrate in the opposite direction, to the cathode. When the battery is discharged, both the transport of Li^+-ions and electrons are reversed [2], as illustrated in Figure 2.1. The lithium transfer between the electrodes is accompanied by intercalation at the two electrodes. Intercalation refers to a host/guest solid-state redox reaction involving insertion of mobile guest ions from an electrolyte into the structure of a solid host combined with electrochemical charge transfer [15]. General description of the electrochemical processes in a Li-ion cell are presented with the reactions presented in equation (2.1) – equation (2.3) [2], written on the form of charging:

Positive electrode: $$LiMO_2 \rightleftharpoons Li_{1-x}MO_2 + xLi^+ + xe^- \quad (2.1)$$

Negative electrode: $$C_6 + xLi^+ + xe^- \rightleftharpoons Li_xC_6 \quad (2.2)$$

Total cell reaction: $$LiMO_2 + C_6 \rightleftharpoons Li_{1-x}MO_2 + Li_xC_6 \quad (2.3)$$

Equation (2.2) describes the intercalation reaction in the negative electrode. The amount of lithium ions inserted into highly crystalline graphitic carbon is one lithium atom per six carbon atoms, equals a specific capacity of 372 $mAhg^{-1}$, and results in an increase of the interlayer distance of the graphene layers by ca. 10% [2]. During intercalation the stacking order of the graphene layers transform into AAAA stacking, meaning that two neighboring graphene layers face each other [2], as illustrated in Figure 2.2.

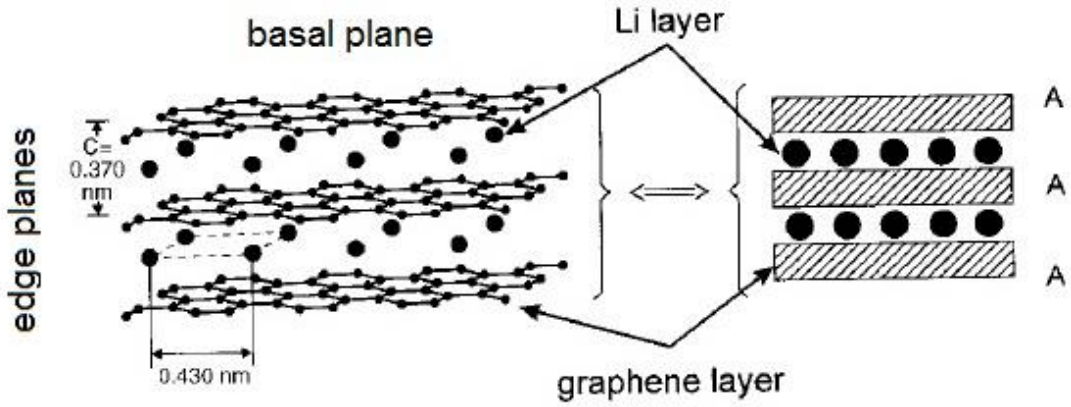

Figure 2.2: Structure of fully lithiated graphite, with the characteristic AAAA stacking sequence of the graphene layers, and the layers of intercalated lithium in between. With modifications from [15].

Intercalation into graphite is characterized by a stepwise formation of layers of lithium ions within the graphite matrix; energetically favorable compared to random distribution of lithium ions. It is named staged formation and characterized by a stage index, giving the number of graphene layers between the two nearest Li-layers [15]. For graphite, the Li^+-ions enter the carbon structure through edge planes, but for basal planes only through defect sites, before the ions diffuses into the structure.

This stage formation is easily observed when lithium ions are being intercalated into the carbon structure. Figure 2.3 displays an ideal potential curve for reduction of graphite, reaching stage 1. The plateaus represent coexisting phase regions, indicating the voltages where the intercalation processes are taking place in the electrode [17]. The right image in Figure 2.3 is an experimentally measured potential curve for Li^+ intercalation into graphite, showing a more smooth transition from one plateau to the other. The observable difference in curve shape is due to variations in the distribution of the active material in the real electrode, relative to the ideal one [15].

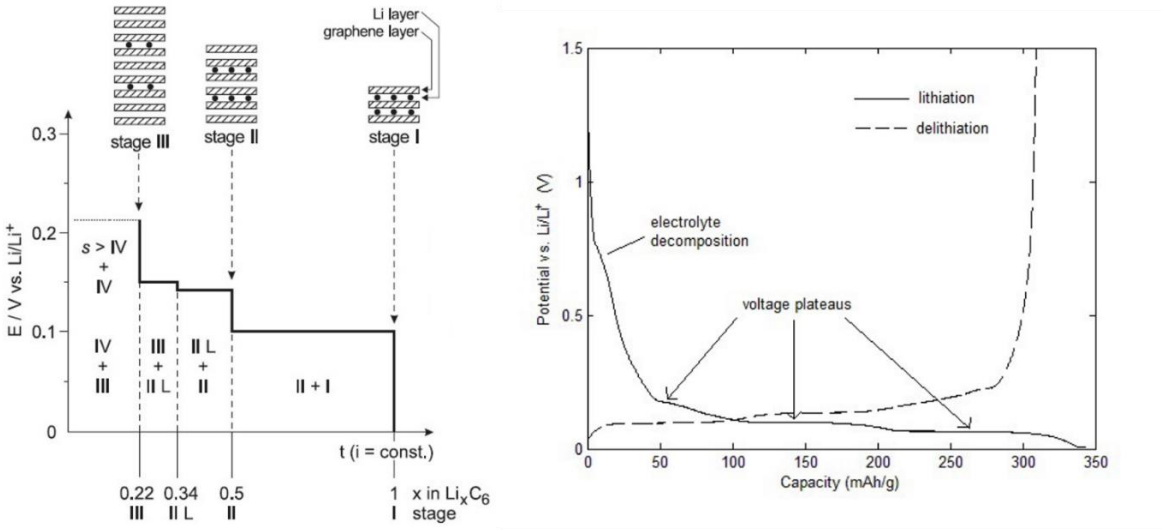

Figure 2.3: Potential curves illustrating the stage formation occurring when lithium intercalates the graphite structure. Left: ideal potential curve, with modifications from [15]. Right: experimentally measured potential curve [18].

2.2 Cell components

In the following sections, a more detailed description of some of the already mentioned cell components will be given. First, a review of the different components of conventional electrolytes is provided, in addition to a type of electrolyte additive. Then follows a detailed presentation of typical electrode materials, with main focus on the positive electrode components.

2.2.1 Electrolyte

Proper operation of the Li-ion cell system, allowing high transport of Li^+-ions between the two electrodes, sets some requirements for the properties of the solvent and salt.

2.2.1.1 Solvents

In case of the solvent, it has to obtain the following properties to be utilized in a Li-ion battery cell: i) dissolve the lithium salt, corresponds to a high dielectric constant, ii) ensure good ionic transport by obtaining low viscosity, iii) chemical and electrochemical stability, iv) liquid state in a wide temperature range, and v) economical, safe and nontoxic [19, 20]. In terms of dielectric constant and viscosity, cyclic and acyclic esters are completely

different compounds; the cyclic obtain high dielectric constants and high viscosity, while the linear obtain low dielectric constant and are more in a fluid state [20]. The solvents most commonly used are organic carbonates: ethylene carbonate (EC), propylene carbonate (PC), dimethyl carbonate (DMC), diethylene carbonate (DEC) and ethyl methyl carbonate (EMC) [20]. Their chemical structure is provided in Figure 2.4, clearly illustrating those being cyclic and linear carbonates.

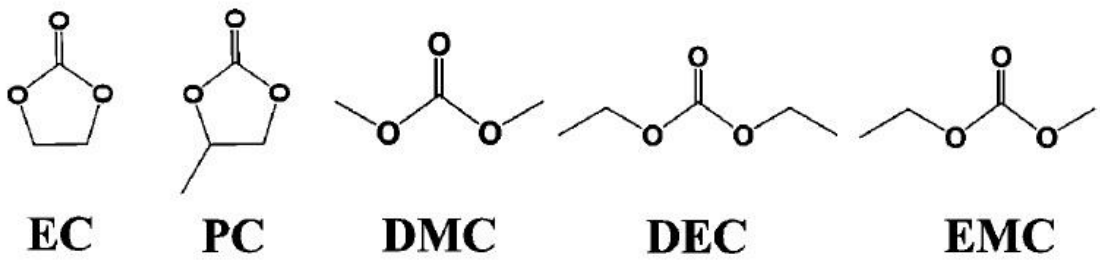

Figure 2.4: Chemical structure of ethylene carbonate (EC), propylene carbonate (PC), dimethyl carbonate (DMC), diethylene carbonate (DEC) and ethyl methyl carbonate (EMC), cyclic and linear organic carbonates used as solvents in lithium-ion battery electrolytes. With modification from [20].

Comparing the stability of the most common organic liquid electrolytes with operation voltages of the electrode materials, schematically illustrated Figure 2.5, indicate a thermodynamically unstable system. However, the current Li-ion batteries operates under kinetic stability by the formation of a solid electrolyte interface (SEI) at the anode [5]. During the initial cycles, small amounts of electrolyte sacrificially decomposes and form a protective film on the electrode surface. Composition of the SEI depends both on the electrolyte and the substrate, shown in the work by Peled et al. [21]. Their experimental results also revealed some general trends in the SEI formation; there are compositional and morphological differences between the SEI formed on the basal and the edge planes of graphite. The film on the basal planes was found to be enriched in organic compounds but was thinner compared to one found on the edge planes, which contained predominantly salt-reduction products. The SEI is an ionic conductor and electronic insulator, allowing Li^+-ions to continuously intercalate and deintercalate, while preventing further electrolyte decomposition [5].

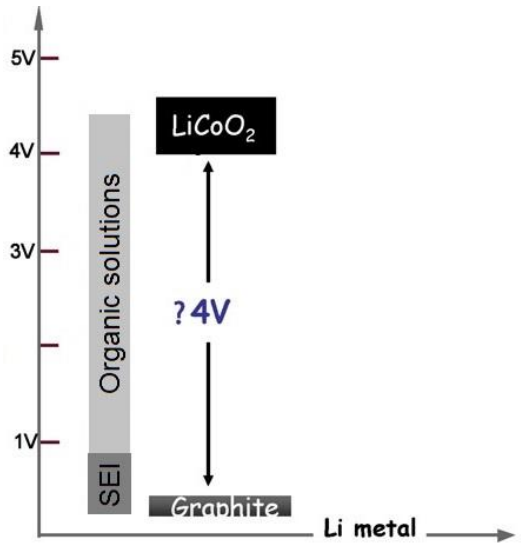

Figure 2.5: Schematic illustration of the electrochemical stability window for common organic electrolytes. With modifications from [5].

The intercalation reaction is affected by the type of solvent present; when EC forms a protective SEI layer on the electrode surface PC fails making this happen. The different behavior is due to co-intercalation of the PC molecules which leads to a destruction of the graphene structure, a process called exfoliation [20]. Since the Li-ion battery is operating outside the stability window of the organic solvents, the formation of SEI is essential for stable operation, which has led to the unique position of EC as solvent in Li-ion batteries.

Considering the requirements for a good solvent, EC displays a slightly higher dielectric constant compared to PC. However, EC has a relative high melting temperature of ~36°C [20], in addition it has too high viscosity. For EC based electrolytes, addition of linear carbonates is crucial to expand the limited liquid range and make the electrolyte solution less viscous. This electrolyte composition, combining linear solvents and EC is the current SOA Li-ion battery electrolyte [20].

2.2.1.2 Salt

The salt should meet the following properties for proper operation in Li-ion cells: i) completely dissolve and dissociate in the solvents, ii) the solvated ions should possess a high mobility, iii) anions should not undergo oxidative decomposition at the cathode, and v) be nontoxic, obtain chemical and thermal stability. Based on well balanced properties

obtained by lithium hexafluorophosphate, $LiPF_6$ compared to other possible candidates, this is the preferred salt for commercial cells. However, it has to be pointed out that $LiPF_6$ is highly moisture sensitive, forming hydrofluoric acid, HF which might cause cell degradation [20, 22].

2.2.1.3 Electrolyte additives – anion receptor

Adding an additive to the electrolyte solution is a very economic and effective method to enhance the Li-ion battery performance, e.g. improve the physical properties such as increased ionic conductivity [23]. One example of the latter is a compound named anion receptor (AR). This is a class of organic ligands that coordinate with anions from the lithium salt, where a part of the negative charge from the anion is delocalized to the anion receptor, leading to a decrease in the charge density of the anion and less electric field attraction between the cation and the anion [24]. Complexation of the anions helps to increase the dissociation of the electrolyte salts and thereby increasing the lithium transport number [25]. In their study of various anion receptors, Qin et al. [24], reported a slight improvement in the total cell performance (positive electrodes consisted of $Li_{1.1}[Ni_{1/3}Co_{1.3}Mn_{1/3}]_{0.9}O_2$, and the negative electrode of mesocarbon microbreads) using anion receptor; improved capacity retention and reduced interfacial impedance was achieved by adding tris(hexafluoroisopropyl)borate (THFIPB) to the EC/EMC based electrolyte.

2.2.2 Electrode materials

In battery science, the convention is to denote the electrodes by how they operate during discharge, defined in Figure 2.1. These terms thus shifts upon charging of the system, so an easier approach is to use the names positive and negative electrode. For research purposes and laboratory use, another cell configuration is introduced named half-cells. However, the use of this cell type challenges the electrode terminology of the negative electrode in a practical Li-ion cell. On the other hand, the positive electrode in Figure 2.1 also acts as the positive electrode in a half-cell.

The first Li-ion batteries being introduced to the market by Sony were based on the use of $LiCoO_2$ and a non-graphitizable, or hard carbon, as the positive and negative electrode

materials, respectively [2, 20]. Soft carbons are the second group obtaining the property of being graphititized upon heat treatment [26]. Today, the insertion materials used as active anode materials are roughly classified as graphitizable or non-graphitizable (soft and hard carbons) [15]. Examples of some commercial anode materials are hard carbon (pitch derived), graphititized mesocarbon, coated natural graphite and synthetic graphite [2]. Along with graphite and other carbon materials, some of the typical cathode materials being used in Li-ion batteries, are presented in Figure 2.6.

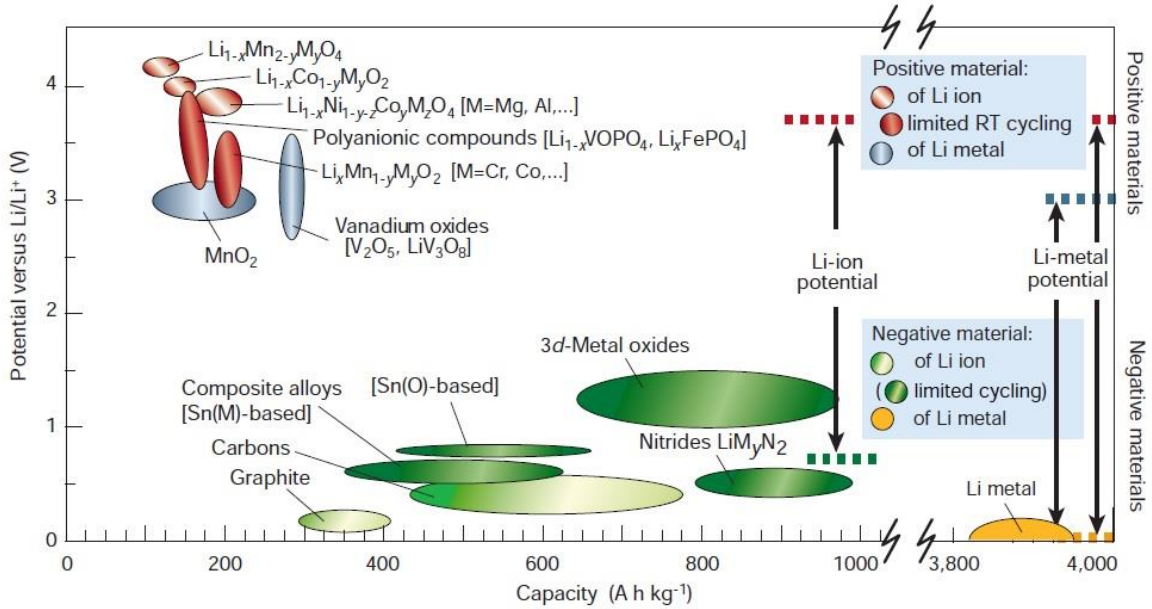

Figure 2.6: Overview of some typical materials for use in both positive and negative electrodes in lithium-ion batteries [3].

2.2.3 Positive electrode

Active materials commonly used in the positive electrode are $LiCoO_2$, $LiMn_2O_4$ and $LiFePO_4$ [27]. The electrical conductivity of these three materials are in the order of 1E-10 – 1E-3 Scm^{-1} [28, 29]. In comparison, graphite obtain, at room temperature, metallic behavior parallel to the graphene layers with a value of 2.6E4 Scm^{-1} [2]. The rather low electrical conductivity of the transition metal oxide materials results in poor battery cycleability for electrodes which contain only active cathode material [10]. A numerical study by Chen et al. [29], based on among other $LiMn_2O_4$ and $LiFePO_4$, concluded that neither surface nor bulk modifications of active material particle conductivities seem

realistic to improve in order to increase the electrode conductivity. However, the simulated results showed that the conductivity of the composite electrode was increased by a value of 25 times compared to the bulk conductivity of the active material when carbon black was added in the form of carbon coating of the active material particles.

2.2.4 Conductive carbon additives in the positive electrode

Current state-of-the-art Li-ion battery cathode consists of particles of active material and "inactive" materials, the latter referred to as polymeric binder and conductive additive. Illustration of how these components can be mixed in the electrode is given in Figure 2.7. Like the names implies, the binder plays the role of binding the active material, conductive additive and current collector together, while the conductive additive contributes to an increase in the electric conductivity. Both components contributes to the structural stability of the electrode, as well as to the electrochemical properties [30]. However, it should be noted that the role of the two "inactive" electrode components also is restrained by the others due to the competition between the ion blocking effect of the binder and the electronic conduction of the conductive additive [30]. Conductive carbons optimize the electrical conductivity of the positive electrode but are not involved in the electrochemical redox process in the state-of-the-art Li-ion battery. Consequently, to maximize the energy density of the Li-ion cell the amount of conductive carbon needs to be minimized. Nowadays the quantity of the conductive additive typically used in the positive electrodes of commercial batteries is below 10% of the total electrode mass [2]. In order to obtain a composite electrode with both high mechanical strength and high conductivity it is important to optimize the additive and binder ratio for the composite electrode to be utilized [30].

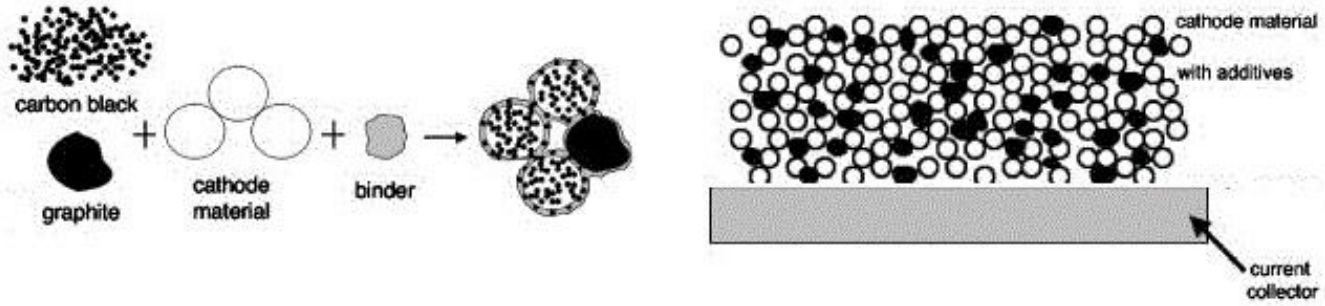

Figure 2.7: Schematic illustration of how conductive carbon additives, here represented with a binary mixture of carbon black and graphite, can be incorporated in the positive electrode. With modifications from [29].

The conductive additive contributes to enhancing the cathode cycleability by filling the free spaces in between the particles of active material, thereby increasing the electrode conductivity, see Figure 2.7. This network provides a low resistance path for the current between the current collector and particles of the active material; facilitating a fast current flow through the entire electrode, improving the utilization of active material and reducing polarization effects. In addition, the additive also absorb and retain electrolyte solution which allows an increased intimate contact between Li^+-ions and the insertion material, which lead to better utilization of the active material [2, 31, 32].

Carbon is the material of choice as conductive additive in the cathode due to properties like high electronic and thermal conductivity in addition to low weight, low costs, relatively high chemical inertness and nontoxicity [2].

2.2.5 Typical carbons used as conductive additive

Carbon black and graphite are commonly used as additives in the current SOA Li-ion battery cathodes, due to their properties like high electrical conductivity and chemical inertness. These carbon materials differ in crystallinity, texture, morphology, density, surface properties, particle size and purity, which depend on their sources and manufacturing process [31].

Graphite is included in the family of sp^2 bond carbons, which makes up the fundamental structural unit of layers of hexagons, named graphene layers. These are stacked in parallel in the order of ABAB, or the not so frequent ABCABC, as illustrated in Figure 2.8. Each

carbon atom also contribute with an electron to a delocalized π molecular orbital, creating weak van der Waals bonds which keeps the graphene layers stacked together. In addition, these electrons gives the graphite electrically and thermally conductive properties parallel to the planes, characterizing graphite as an anisotropic material. Ideal graphite has an interlayer spacing of 3.354 Å and large crystallites; characterized by large values of crystallite size parallel to basal plane, L_a, and crystallite size perpendicular to basal plane, L_c. One carbon particle consists of several of these crystallites, oriented relative to each other as illustrated in Figure 2.9. The types of graphitic carbon powders which primarily are applied as conductive additive in positive electrode is highly crystalline, with an average interlayer distance close to the ideal graphitic value, and have a particle size well below 10 µm [2, 15, 33].

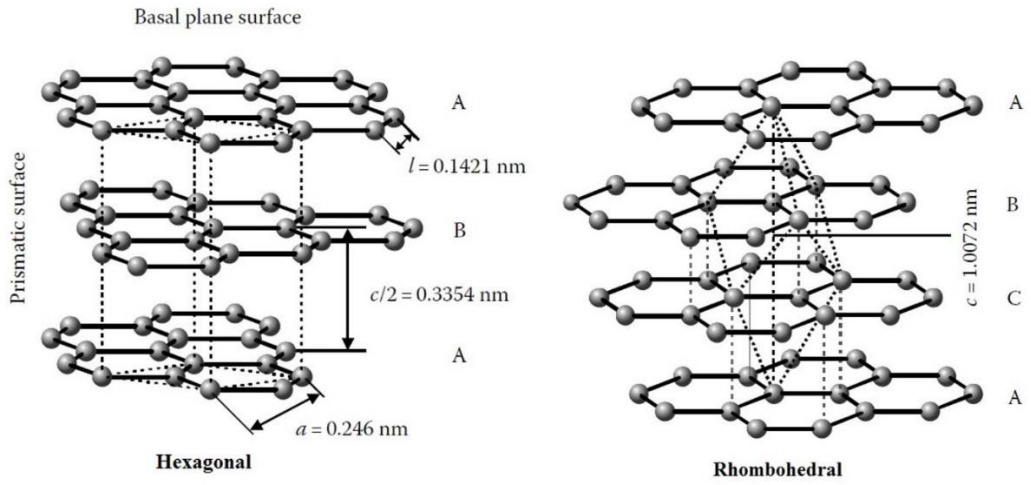

Figure 2.8: Graphite crystal structures. Left: Hexagonal. Right: Rhombohedral. With modifications from [2].

Amorphous carbon is also made up of the same structural units as graphite, but without the long range crystalline order [34]. There is a variety of types of amorphous carbons such as glassy carbon, activated carbon and carbon black. The latter characterized by aggregates of spherical primary particles having a diameter of 10-90 nm, and large surface areas [2, 29, 35]. The repeating carbon layers are forming a concentric structure making up the carbon particles, as seen in Figure 2.9. Compared to graphite, the layer spacing is larger and in the order of >3.50 Å, while the crystallites sizes are typically smaller having values of 10-20 Å for L_a and L_c [2, 35]. In the case of carbon black, only high-purity forms can be used, like Super P carbon black and Ketjen Black [2].

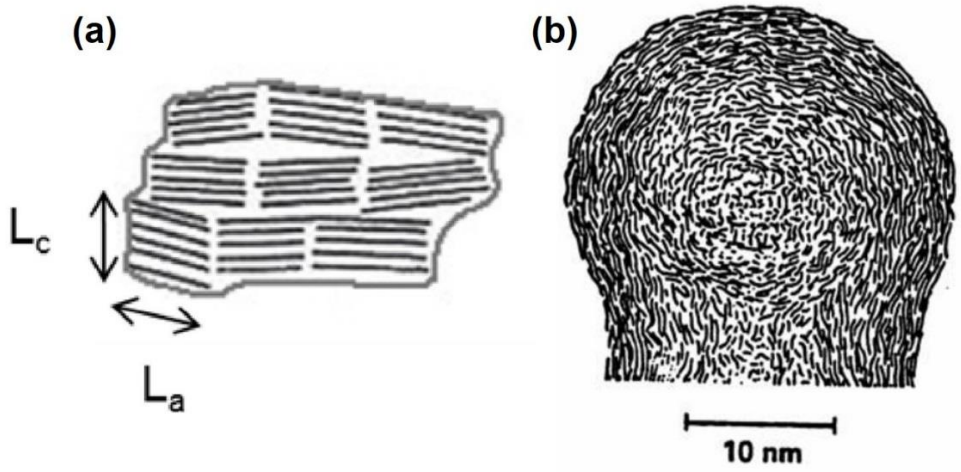

Figure 2.9: Illustrations of carbon particles, showing the arrangement of graphene layers: ***(a)*** *graphite, with crystallites defined by L_a and L_c [18]* ***(b)*** *carbon black [36].*

To summarize; carbon black displays large surface area and consists of aggregation of nano-sized primary spherical particles, while micro-sized flake-like graphite particles display moderate surface area and high anisotropy, indicating that the two materials have different but complementary properties [37, 38], and they fulfill the mentioned requirements for a good conductive carbon additive.

In a composite electrode, graphite and carbon black also show complementary electrical functions; graphite creates the electronic conductive path in the electrode whereas carbon black improves the contact between the particles of the active electrode material [2, 37]. This behavior is observed experimentally by Cheon et al. [39] in their optimization of $LiCoO_2$ composite electrode by the use of binary carbon mixture consisting of KS6 graphite and Super P. Additionally, Sphar and coworkers [40] observed that graphite and carbon black contribute to better mechanical stability, long-term stability, and increased specific charge. These observations clearly shows the benefits of combining the two types of conductive carbon additives to the Li-ion battery cathode.

As well as graphite and carbon black, graphene has also emerged as a conductive additive for Li-ion batteries [1, 32]. Compared to graphite, graphene possesses properties which makes it more favorable compared to graphite, like higher electrical conductivity and better mechanical stability. Studies like the one conducted by Jiang et al. [41] shows great improvement of the rate performance of a $LiMn_2O_4$ cathode by adding graphene, thus in

combination with acetylene black to the electrode. However, for commercial applications the use of graphene is limited because the synthesis procedure is rather complicated which results in a high cost [42].

2.3 High-voltage lithium-ion battery

Most of the Li-ion batteries being produced today still relies on the use of the same materials adopted in first commercial Li-ion battery cell [5]. In the field of electrical vehicles it is undesirable to use e.g. $LiCoO_2$, due to the low energy density, high cost and safety concern [1]. There are intensive research to improve both electrolyte and electrode materials, and Figure 2.10 illustrates the next generation Li-ion battery relative to the current one in terms of voltage and energy density. One attempt is to replace the commercial $LiCoO_2$ cathode material with a new high-voltage cathode material, operating at a potential of 5.0 V vs. Li^+/Li. Higher operation potential of the cathode results in higher total cell voltage, which in turns means increased energy density, and also increased driving range for electrical vehicles; an improvement which is necessary in order to make it more competitive towards the conventional gasoline-powered car.

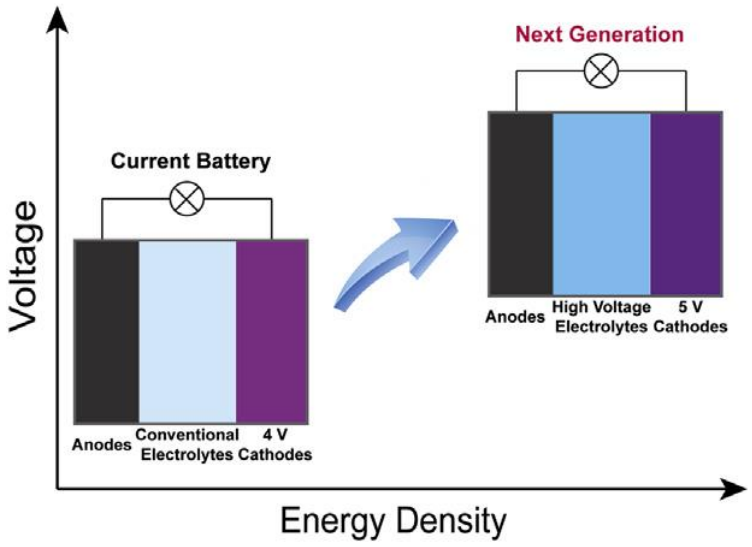

Figure 2.10: Graphical illustration of the next generation Li-ion battery cell compared to the current system in terms of voltage and energy density [1].

Great efforts are being made to develop next generation cathode materials. One promising candidate is Li(Ni,Mn,Co)O_2 (NMC) materials, obtaining various stoichiometric compositions, e.g. Li[$Li_{0.2}Mn_{0.56}Ni_{0.16}Co_{0.08}$]$O_2$, as synthesized in the work by Li et al. [8]. Operation at high voltages introduce some additional electrochemical reactions in the cell; anion intercalation and electrolyte oxidation, which need to be considered in the evaluation of the electrode performance. Although the active material has the possibility of operating at 5.0 V vs. Li^+/Li, the ”inactive” conductive carbon additive in the current state-of-the-art Li-ion battery, become active towards these high-voltage processes.

Investigations need to be made in order to reveal whether the conductive carbon network will sustain the changes due to these two processes. In the following two sections, a more detailed description of the already mentioned high-voltage electrochemical reactions will be presented, based on previous studies. The last part of this chapter summarizes how the conductive carbon additive might be affected by these high-voltage processes.

2.3.1 Anion intercalation – literature review

Upon charging of the Li-ion cell to potentials higher than the current state-of-the-art battery, which equal 4.3 V vs. Li^+/Li, anions from the lithium salt, e.g. PF_6^- starts to intercalate the structure of the carbon. Märkle et al. [10] used in their study a simple approach, assuming that the total charge current was fully related to anion intercalation. Evaluation of the capacity values obtained in their system operating at 5.5 V vs. Li^+/Li, clearly stated that this simplified approach was not sufficient. They pointed out that electrolyte oxidation reactions cannot be neglected. While anion intercalation is an reversible reaction, electrolyte oxidation is an irreversible decomposition process being oxidative in nature [20]. Meaning that upon charging to high voltages, the charge current is related to both electrolyte oxidation and anion intercalation, while the following discharge current is only related to anions leaving the carbon structure. An expression of the system reversibility, and also an indication of the anion deintercalation, is expressed by the Coulombic efficiency given in equation (2.4). Here Q_{rev} and Q_{irev} is the specific charge capacity related to reversible and irreversible reactions, respectively.

$$C_{eff} = \frac{Q_{rev}}{Q_{rev} + Q_{irr}} \cdot 100\% \tag{2.4}$$

The mechanism describing PF_6^- intercalation in graphite has been extensively studied by Seel and Dahn [11], using an ethyl methyl sulfone (EMS) based electrolyte. From their galvanostatic cycling results, they suggested that PF_6^- intercalates into graphite forming different staged phases; indicated by the appearance of plateaus in the potential curve, starting at around 4.6 V vs. Li^+/Li. They verified that the reaction mechanism was one of anion intercalation by conducting *in situ* XRD experiments, with focus on the changes in diffraction pattern related to the (002) planes in the graphite structure. During cycling they observed a shift in the 002 peak towards lower scattering angles while an additional diffraction peak appeared at higher scattering angles. They claimed that the appearance of this new peak was a clear indication of staged intercalation, forming a superstructure with stage index given in equation (2.5). The scattering angle related to the (002) planes for stage index N is given by $2\theta_{00N}$, while the scattering angle for the additional diffraction peak is $2\theta_{00N+1}$, for a N stage superstructure. They observed that upon full charging a stage 2 intercalated graphite was formed, resulting in a specific capacity of 140 Ahg^{-1} and a composition of $(PF_6)_{0.5}C_8$. While the carbon structure obtained an average interlayer spacing of 3.910 Å, corresponding to an increase of 16.7 % from the initial state. Upon the following discharge step, the anion intercalation was observed to be only partly reversible, due to the observation of a broader discharge peak relative to the initial one, indicating that anions were remaining in the carbon structure.

$$N = \frac{1}{\left[\frac{\sin(\theta_{00N+1})}{\sin(\theta_{00N})} - 1\right]} \tag{2.5}$$

In the same study, Seel and Dahn [11] also investigated the reversibility of the anion intercalation in graphite exposed to a more conventional electrolyte based on EC and DEC. A striking difference in the XRD measurements was observed compared to the results from the experiments with EMS. The initial peak did not start to reappear before at very low potentials, and they claimed that the carbon structure got damaged due to possible electrolyte decomposition or co-intercalation of solvent molecules. The same behavior was

observed in the work of Märkel et al. [7], where they studied graphite cycled in a PC based electrolyte. Structural degradation of electrode due to exfoliation was confirmed by SEM analysis. Not all types of graphite electrodes are subjected to exfoliation. In the same study by Märkle and coworkers [7] they showed that differences in crystallinity of the carbon additive had a great influence on the degree of anion intercalation, which is one of the factors that determine the structural impacts. The highly crystalline particles were shown to be favorable for PF_6^- intercalation at high positive potentials. These observations were also confirmed by other researchers. Ishihara et al. [43] revealed that the types of carbon materials with the highest degree of crystallinity, close to ideal graphite, exposed to 1 M $LiPF_6$ in 1:2 vol% EC/DMC, obtained the highest 1st discharge capacity.

While anion intercalation into graphite might result in a specific capacity of 140 $mAhg^{-1}$, reported by Seel and Dahn [11], the results of Zheng et al. [32] presented a completely different results for high surface area carbon black cycled in a conventional electrolyte. Upon long term cycling, the material displayed a very low capacity, equal to approximately 5 $mAhg^{-1}$. This indicates a stable but rather limited anion intercalation into carbon blacks. As a results of this short range crystal structure found in carbon blacks, there is reason to believe that even smaller amounts of anions, when comparing with graphite, can intercalate before being entrapped and cause structural damage on the electrode. This was shown in the work conducted by Syzdek and coworkers [9] in their study of carbon blacks additives in an electrolyte composed of 30:70 vol% EC/DEC 1 M $LiPF_6$. They observed electrode degradation after cycling at high voltages, a behavior similar to what was observed for graphite [10, 11]. SEM analysis after prolonged cycling revealed substantial changes of the particles and electrode surface morphology which was claimed to be due to entrapping of PF_6^--ions, which again was confirmed by both *in situ* Raman spectroscopy and *in situ* XRD [9].

2.3.2 Electrolyte oxidation – literature review

The current state-of-the-art electrolytes used in Li-ion batteries have a stability window that does not include operation at high-voltages, as illustrated in Figure 2.5. Upon charging to voltages beyond 4.5 V vs. Li^+/Li, the cathode interface cannot stabilize the carbonate-based electrolytes and oxidation of the electrolyte will occur. This make it challenging to develop high-voltage cathode materials [1, 44, 45]. The appearance of electrolyte decomposition

products on both basal and edge planes of graphite particles, have been observed in the work of Märkle et al. [7] using SEM. However, in comparison with the extensive work devoted to the interfacial characterization of the SEI layer on carbon anodes, researchers are unsure whether the decomposition products forms a similar stable interphase at the positive electrode [1, 15, 38, 44, 46].

Attempts have been done in order to characterize these electrolyte decomposition products to some extent. On example is the work of Joho and Novak [47] in their investigation of oxidative decomposition of organic-carbonate-based electrolytes. They proposed that EC and DMC most likely decompose by their own reaction mechanisms; EC being preferably oxidized over DMC (higher dielectric constant for EC means increased concentration of that solvent molecule close to the cathode surface when a positive voltage is applied to the system), forming polycarbonates based on EC, and carbon dioxide, CO_2. Both theoretical investigations [48] and experimental studies of a high-voltage cathode materials containing graphite [49], have supported their results.

The thickness of the film formed on the cathode has also been a subject of controversy, but in general it has been considered to be much thinner compared to the SEI on the anode [44]. This was also shown experimentally in the work of Malmgren and coworkers [50] in their study to compare the SEI and film formed on the cathode. Their results revealed that smaller amounts of electrolyte decomposition products were found on the cathode surface compared to the cycled anode. The SEI layer on the anode was estimated to be in the order of two tens of nanometers while the cathode interface thickness was estimated to be no thicker than a few nanometers.

Defining the onset potentials for electrolyte oxidation is rather challenging, cause upon charging in the vicinity of 4.5 V vs. Li^+/Li, anion intercalation needs to be taken into consideration [50]. Several studies have thus provided information about onset oxidation potentials, especially in the case of carbon black exposed to various electrolytes. Syzdek et al. [9] in their study of carbon black additives, the initial cycle showed a sharp current rise at 4.7 V, for a carbon electrode consisting of Shawinigan Black in an electrolyte with the composition of 30:70 vol% EC/DEC 1 M $LiPF_6$. The authors stated in their report that the same behavior was observed for Super P Li. Zheng et al. [32] reported an onset oxidation potential of 4.65 V vs. Li^+/Li for a pure carbon electrode which contained Super P (Brunauer-Emmet-Teller (BET) specific surface area of 76.4 m^2g^{-1}) in an electrolyte with

the composition of 1:2 vol% EC/DMC 1 M $LiPF_6$. Their study also investigating other high surface area carbons, having BET surface areas in the order of 10-20 times larger than for Super P. These materials showed an onset oxidation potential of approximately 3.7 V vs. Li^+/Li. The observed difference was explained by the fact that higher specific surface area provides more active sites for electrolyte oxidation. Differences in BET surface area have also been related to differences in specific irreversible charge, as shown in the work of La Mantia et al. [38].

2.3.2.1 Summary: How can high-voltage processes affect the stability of the conductive carbon additive?

One possible approach is to assume that carbon additives sustain the high-voltage operation, meaning that the conductive network is maintained even though anions are intercalating the carbon structure and electrolyte decomposes at the particle surface. This is thus the best case scenario in terms of cycling performance of the composite electrode. Additional anion intercalation will then contribute to an increase in total specific capacity for the composite electrode while the stability is maintained.

Taking into consideration previous research in the field of high-voltage Li-ion batteries a more realistic approach is to assume the conductive carbon additive will be affected in some degree of the operation at high voltages. In a study of local degradation phenomena in composite cathodes, Kerlau and coworkers [51] adopted a simple theoretical model. Their observations confirmed that local increase of the contact resistance between the particles of active material and carbon additive will alter the distribution of the conductive paths in the electrode, being responsible for an overall degradation of electrochemical performance of the composite electrode. This local increase of contact resistance and loss in electrical conductivity might happen due to anions remaining in the carbon structure, leading to exfoliation, creation of cracks and the formation of a more porous electrode structure. Reduction in mechanical integrity of the electrode might also be a consequence of this degradation processes. In addition, electrolyte decomposition products might from a film possessing the properties of being both electronically isolating (as in the case of SEI) and preventing ions from leaving the carbon particles; possible leading to loss of electrical contact among active material, carbon additive and current collector, also resulting in an impedance rise and capacity loss in the composite electrode [7, 9, 10, 32, 51, 52].

Summarizing both approaches, Figure 2.11 provide a schematic illustration of how conductive carbon additive operating at high-voltages might be affected by the electrochemical processes taking place at the composite electrode; anion intercalation and electrolyte oxidation.

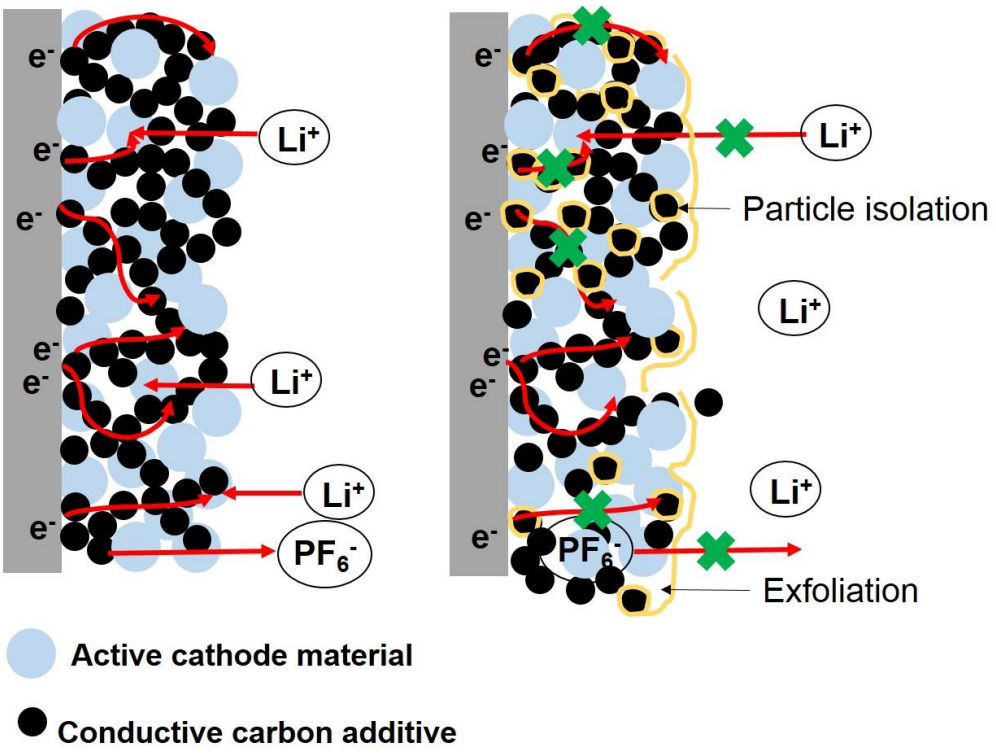

Figure 2.11: Schematic illustration of a composite cathode operating at high voltages, given in the state of discharge. Left: initial state of the electrode. Right: conductive carbon additive network has been negatively affected by anion intercalation and electrolyte oxidation, leading to a loss of electric conductivity and overall performance of the electrode.

2.4 Electrochemical impedance spectroscopy

Electrochemical impedance spectroscopy (EIS) is an electrochemical technique used to study the kinetics of electrode reactions. It has the advantage of being a fast and non-destructive technique, since the system is just slightly moved away from its original state during analysis [53].

The impedance of an electrochemical cell or electrode may be understood as generalized resistance. The measurements are performed by applying a sinusoidal potential with varying frequencies and a small amplitude (~5 mV), while the current response is

measured. The current will also be a sinusoidal function, but not necessarily in-phase with the potential. This phase shift depends on the electrochemical processes in the system, and may be represented by equivalent electrical circuit elements, like resistors, capacitors and inductors [54]. The resulting impedance, Z, is usually represented as a complex number and can be shown graphically in a Nyquist plot, see Figure 2.12. In this type of plot, the imaginary part of the impedance is given as a function of the real part of the impedance.

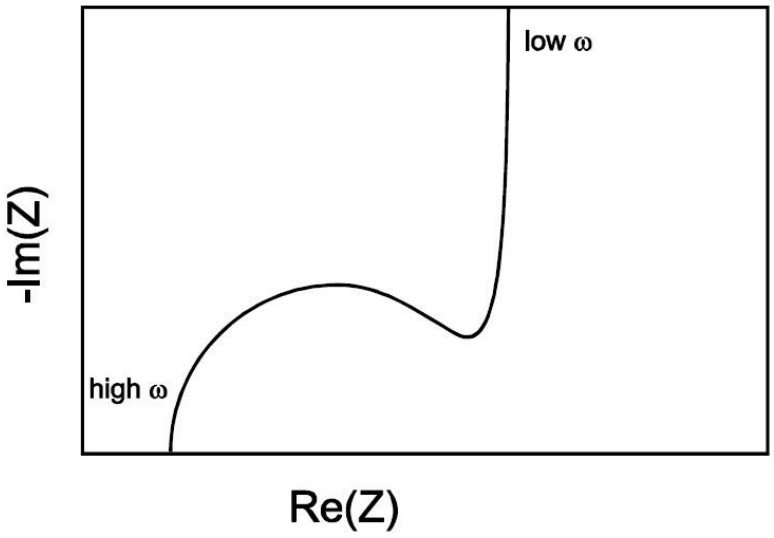

Figure 2.12: Nyquist plot for an electrode with a capacitive response in series with a faradaic response [55].

In the case of a pure capacitor behavior, the current is phase shifted 90 degrees with respect to the voltage. The capacity impedance decreases with increasing frequency and obtain only an imaginary impedance component, expressed with equation (2.6). Here j is the imaginary unit, ω is the angular frequency, and C is the capacitance [56].

$$Z = \frac{1}{j\omega C} \tag{2.6}$$

2.5 X-ray diffraction

X-ray diffraction is a technique used to characterize the crystal structure of materials, e.g. interlayer spacing related to (002) planes, and crystallite sizes in carbon powders. In addition, this technique can be combined with galvanostatic cycling to investigate the structural changes in the carbon structure upon intercalating anions, mainly by studying the changes in interlayer spacing, d_{002}.

This technique is based on the use of X-rays, a type of electromagnetic radiation with high energy and wavelengths in the range of 0.01-10 nm. By exposing a crystalline sample for an incident beam consisting of monochromatic and parallel X-rays, the atomic planes will cause the waves to interfere with each other as they leave the crystal, a phenomenon called X-ray diffraction [57]. This occurs only when the atoms are capable to scatter the beam, as well having a spacing that is comparable in magnitude with the wavelength [58], which is the case e.g. for ideal graphitic carbon having an interlayer spacing of 3.35 Å. An illustration of a how X-rays are diffracted in a crystalline sample is given in Figure 2.13, where the blue dots might represents carbon atoms in two adjacent graphene layers named A and B, representing the characteristic (002) planes.

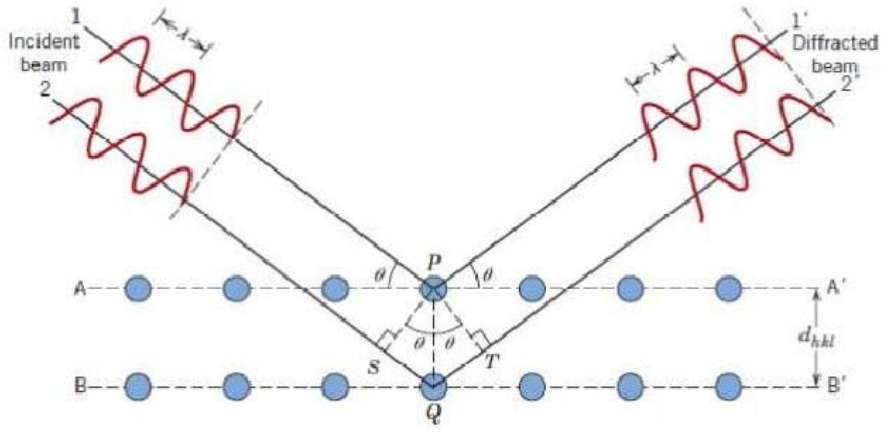

Figure 2.13: Illustration of how an incident X-ray beam is diffracted in a crystal structure consisting of the two atomic layers A and B, and the resulting reflected beam [58].

Only the diffracted beam consisting of constructively interfering waves is detected. Based on the illustration in Figure 2.13 a relation between the angle of diffraction for constructive

interference, the X-ray wavelength and the interatomic spacing can be derived. This expression is also known as Bragg's law and stated in equation (2.6), where n is the order of reflection, λ is the X-ray wavelength, d_{hkl} is the interplanar spacing and θ_{hkl} is the diffraction angle. The two latter parameters both correlated to planes with the Miller indices (hkl) [58].

$$n\lambda = 2d_{hkl}\sin\theta_{hkl} \tag{2.6}$$

The detected beam will appear as peaks in a XRD spectra, presented with the diffraction intensities as a function of scattering angle. The number of peaks and the parameters characterizing the peak shape; position, intensity and width, all provides information about the sample crystal structure. The number of peaks in the diffraction pattern is related to the symmetry of the crystal, while the peak position is related to the spacing between adjacent atomic layers in the structure, and the intensity of the peaks is related to the type of atoms located in the layers [59]. Peak width and position also reveal information about strain in the structure, illustrated in Figure 2.14. Non-uniform lattice strain will results in peak broadening, while there is a shift in peak position towards lower 2θ angles when the strain is uniform [60].

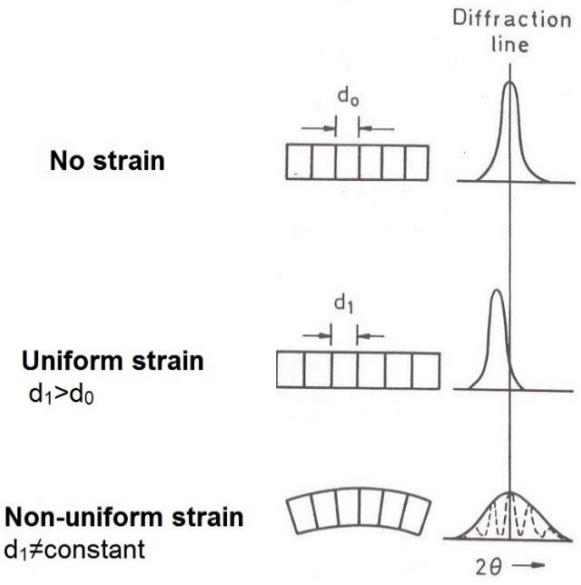

Figure 2.14: Effect of lattice strain on the diffraction peak position and width [60].

Based on the information from the peak width and intensity; measuring the full width at half maximum intensity (FWHM) from the diffraction profile, the crystallite size can be calculated [61]. This is done by implementing the measured FWHM into Scherrer's equation, given in the following expression, assuming no structural strain in the carbon materials [33]. In this formula L(hkl) is the thickness of a crystallite, K is the shape factor set to have a value of 1.0 for carbon materials [61], and β is the value for FWHM given in radians. For (hkl) obtaining the values of 002, 004 or 006 the thickness is found along the c-axis; perpendicular to the basal planes in the carbon structure.

$$L(hkl) = \frac{K\lambda}{\beta \cos\theta_{hkl}} \tag{2.7}$$

3 Experimental

This chapter gives a detailed description of the procedures, equipment and techniques used for testing the carbon materials. The first section provides technical data on the carbon powders. Secondly, the procedures used to prepare electrodes and electrolytes will be presented, followed by a description of the different cells configurations used for electrochemical characterization. The third section will present characterization techniques conducted to test the carbon powders and electrodes, and the condition for each experiment and analysis. Techniques included are galvanostatic cycling, CV, EIS, XRD and SEM. At the end, an experimental matrix will be presented to summarize all cells studied.

3.1 Carbon materials

Three types of carbon powder have been studied: KS6 (KS 6 L graphite, Timcal), Graphene AO-2 (graphene nanopowder 8 nm flakes: AO-2, Graphene Supermarket), and Super P Li (Super P Li, Timcal). KS6 is a well graphitized graphite powder, Graphene AO-2 is a multilayer graphene powder, and Super P Li is a carbon black. Technical data on each material is provided in Table 3.1.

Table 3.1: Technical data for the three carbon powders: KS6, Graphene AO-2 and Super P Li.

	Particle shape	**Particle size [nm]**	**BET [$m^2 g^{-1}$]**	**d_{002} [Å]**	**L_c [Å]**	**L_a [Å]**
KS6	Isometric, irregular spheroids [37]	6500 ($d_{90\%}$) [37], 3000 ($d_{50\%}$) [37]	20 [37]	~ 3.35[1)]	275 (XRD) [62]	475 (XRD) [62], 210 (Raman) [62]
Graphene AO-2	Flakes [63]	~550 (150-3000) [63]	100 [63]	< 4.21 [2)]	-	-
Super P Li	-	40 [37]	62 [37]	> 3.35[3)]	-	-

[1)] Assumed to possess almost ideal graphitic behavior.
[2)] Calculated based on flake thickness and number of monolayers provided from Graphene Supermarket [63].
[3)] Based on the characteristics properties of Super P Li, the interlayer distance is assumed to be larger than for ideal graphitic carbon.

3.2 Slurry preparation and electrode casting

Independent of the type of carbon powder, the electrode composition was set to 90 wt% carbon powder and 10 wt% binder. As the powders display different powder properties, various amounts of solvent had to be used in the electrode preparation, and an overview of the actual amounts added for each slurry are given **Appendix A**. The procedure for electrode preparation does not differ, and a detailed description will be given in the following sections.

The electrode slurries were prepared by starting out mixing polyvinylidene fluoride (PVDF/Kynar, fine powder, Arkema) as the binder, with 1-methyl-2-pyrrolidinone (NMP, anhydrous, 99.5%, Sigma-Aldrich) as the solvent. In order to dissolve the PVDF, the mixture was left for stirring in one hour while being covered up to reduce solvent evaporation. The PVDF/NMP mixture was then transferred to an Al_2O_3 jar together with five 30 mm Al_2O_3 balls and the carbon powder. The jar was left in a planetary mill (PM100, Retsch) at a rotation speed of 150 rpm for two hours in order to make sure that the carbon and the binder were distributed homogeneously. Thereafter, the slurry was transferred to an Erlenmeyer flask, being connected to an aspirator and left for stirring under vacuum in approximately one hour for removal of air bubbles.

The prepared slurry was then cast onto a current collector using a tape caster (model K101, The K control coater) where the height of the blade was adjusted to around 200-220 µm. Pre heating of the electrodes at 60 °C for one hour in a fume hood was conducted in order to evaporate most of the NMP before being introduced into a vacuum furnace (Vacuum drying oven VD23, Binder) for overnight heating at 120 °C and vacuum, to remove the remainder of the solvent. The last step of the electrode preparation process was then to transport the cast electrodes to the big antechamber in the glove box (Labmaster SP, MBraun) for a second overnight heating at 120 °C under vacuum. The total heating time was 28 hours. The electrode casts were then introduced into the glove box and stored under argon atmosphere, with H_2O and O_2 contents less than 0.1 ppm.

Depending on the technique conducted to study the electrode behavior, different current collector materials were adopted. For the electrochemical testing purposes, aluminum foil (0.025 mm thick, 99.45 %, Alfa Aesar) was used. However, Al material cannot be used in the analysis using X-rays. As a replacement, kapton based current collectors were used for

this purpose, since kapton is a commonly used X-ray window material. Two types of kapton current collectors were tested: 1) two-layer film consisting of a conductive carbon layer on top of an isolating polymeric film (Kapton®200RS100, 50 µm thick, DuPont) – *kapton/carbon*, 2) kapton thin-film (SpectroCertified®Thin-Film, 7.5 µm thick, Chemplex) being sputtered with gold using a sputter coater (5150B, Edwards) for approximately three minutes – *kapton/gold*. In the case of kapton based electrodes, the kapton film was pre shaped into circles with a diameter of approximately 40 mm before casting, and during the casting procedure a polymer film with a 17 mm diameter hole was used as a mask. For the Al based electrodes, these were prepared as one large electrode sheet and punched into circular electrodes during cell assembly. Photographs of the three types of carbon electrodes are given in Figure 3.1.

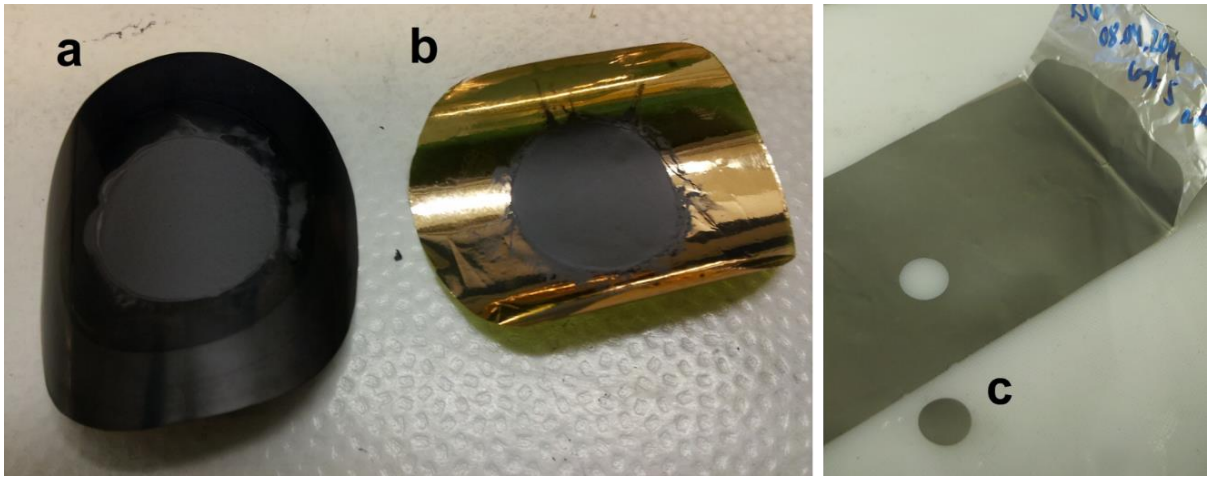

*Figure 3.1: Photographs of three different types of carbon electrodes consisting of various current collector materials: **a** kapton/carbon, **b** kapton/gold, and **c** aluminum.*

3.3 Electrolyte preparation

Four types of electrolytes have been used for all cells assembled. They are all based on the solvents: ethylene carbonate (EC, anhydrous, 99 %, 1 L, Sigma-Aldrich) and dimethyl carbonate (DMC, anhydrous ≥99 %, Sigma-Aldrich), in addition to the salt: lithium hexafluorophosphate ($LiPF_6$, battery grade, ≥99.99 %, Sigma-Aldrich). They differ in the ratio between solvents, and if they contain the anion receptor tris(hexafluoroisopropyl)borate (THFIPB, > 95.0 %, TCI). An overview of the different electrolyte compositions is given in Table 3.2.

Table 3.2: Different electrolyte compositions, given by the relative amounts of the fours species: ethylene carbonate (EC), dimethyl carbonate (DMC), lithium hexafluorophospahte ($LiPF_6$) and tris(hexafluoroisopropyl)borate (THFIPB).

Electrolyte name	Composition
30/70	30:70 vol% EC/DMC 1 M $LiPF_6$
1/1	1:1 vol% EC/DMC 1 M $LiPF_6$
AR30/70	30:70 vol% EC/DMC 1 M $LiPF_6$ 1 wt% THFIPB
AR1/1	1:1 vol% EC/DMC 1 M $LiPF_6$ 1 wt% THFIPB

Electrolyte named 1/1 was ordered premixed from the company BASF – The Chemical Company, while the three others were prepared by the author. An overview of the actual amounts of each component used in the preparation, is given in **Appendix B**, while the procedure for the electrolyte preparation is described in the following paragraph.

The electrolytes were prepared in a glove box (LabMaster SP, MBraun) filled with purified argon and O_2 and H_2O contents less than 0.1 ppm. While the EC was heated to 40 °C in order to be melted, the DMC and $LiPF_6$ were added to a beaker, and EC was added to the end, to prevent the solvent to become solid. The DMC/EC/$LiPF_6$ mixture was covered up to prevent solvent evaporation and left for stirring for four hours to obtain a homogeneously mixed solution. The electrolyte was then transferred to a bottle with cap, and stored in the glove box. Electrolytes containing THFIPB required an extra step in order to obtain the right composition. They were prepared based on the mixed 30:70 vol% EC/DMC 1 M $LiPF_6$ or the premixed 1:1 vol% EC/DMC 1 M $LiPF_6$. An additional amount of the THFIPB powder was added to these electrolytes in order to obtain the right concentration of 1 wt%. The mixture was then left for stirring for four hours before being transferred to another bottle with cap.

3.4 Cell assembly

Three types of electrochemical cells were assembled in this work: i) coin cell, ii) three-electrode (3-E) cell and iii) *in situ* XRD cell. Common for these type of cells is that the carbon electrode acts as the working electrode (WE) and lithium metal is the counter electrode (CE). Whereas the coin cell and *in situ* XRD cell operate in a two-electrode

configuration, the 3-E cell have an additional reference electrode (REF) allowing for assessment of the potential for the WE. All electrochemical cells were assembled in a glove box with argon atmosphere and H_2O and O_2 contents less than 0.1 ppm, while cycled in air. After assembly, the cells were left overnight to ensure that the porous carbon electrode and separator were properly soaked with electrolyte, and equilibrium had been established in the system. The cell voltage was then measured and verified to be in the potential region of 2.5-3.5 V vs. Li^+/Li, otherwise the cell was not connected to the potentiostat and tested.

3.4.1 Coin cell

Coin cells produced by Hohsen Corp. (CR2016/SUS316L, 20.25 mm diameter and 1.6 mm height) were assembled. An image of all the coin cell components is provided in Figure 3.2, while the next paragraph gives a detailed description of each step in the cell assembly.

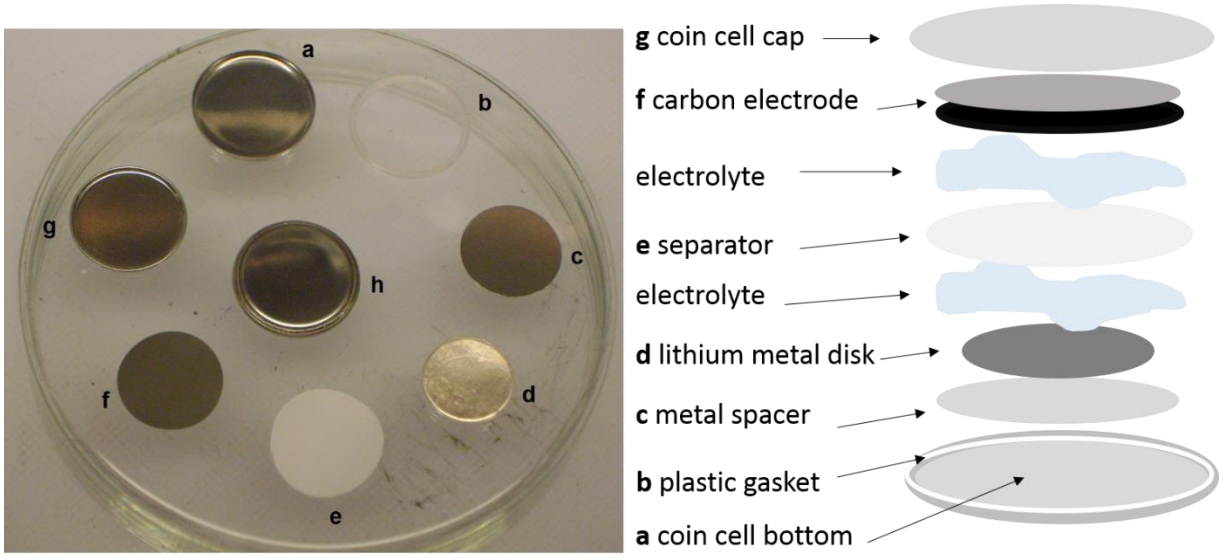

*Figure 3.2: Left: a photograph of the different cell components. Right: an illustration of the stacking order. Cell components included in a coin cell are: **a** cell bottom, **b** plastic gasket, **c** metal spacer, **d** lithium metal disc, **e** separator, **f** carbon electrode, **g** coin cell cap, and **h** assembled coin cell.*

A Li metal disc with 14 mm diameter was cut from a lithium foil (0.75 mm thick, 99.9 %, Alfa Aesar) and brushed on both sides for removal of any surface film. This Li disc was then attached to a 16 mm diameter stainless steel spacer (SUS316L alloy) of 0.3 mm

thickness. The purpose of adding this spacer was to fill the internal space of the cell, and also to provide good contact between electrode, electrolyte and separator. Together with a plastic gasket, the spacer and the Li disc were placed in the coin cell bottom. A 17 mm diameter microporous trilayer polymer membrane (Celgard 2320, 20 µm thick, Celgard®) was put on top of the Li disc and electrolyte was applied on both sides of the separator; 10 µL before and 20 µL after. Carbon electrode of 16 mm diameter was punched from the tape casted electrodes, and both thickness and weight were measured, and placed on top of the separator, followed by the cell cap. The different cell components were fixed together and the cell case hermetically sealed using a crimping machine (Automatic crimping machine, Hohsen Corp.).

3.4.2 Three-electrode cell

3-E cells provided from the company EL-CELL (ECC-REF) were assembled, and an image of the different cell components is given in Figure 3.3. Prior to cell assembly, the REF electrode was prepared. A small piece of Li foil (0.75 mm thick, 99.9 %, Alfa Aesar) was made by using a special tool (ECC-RefLoad, EL-CELL), and then pressed into the feed-through hole of the REF sleeve until the Li just became visible in the inner face of the sleeve.

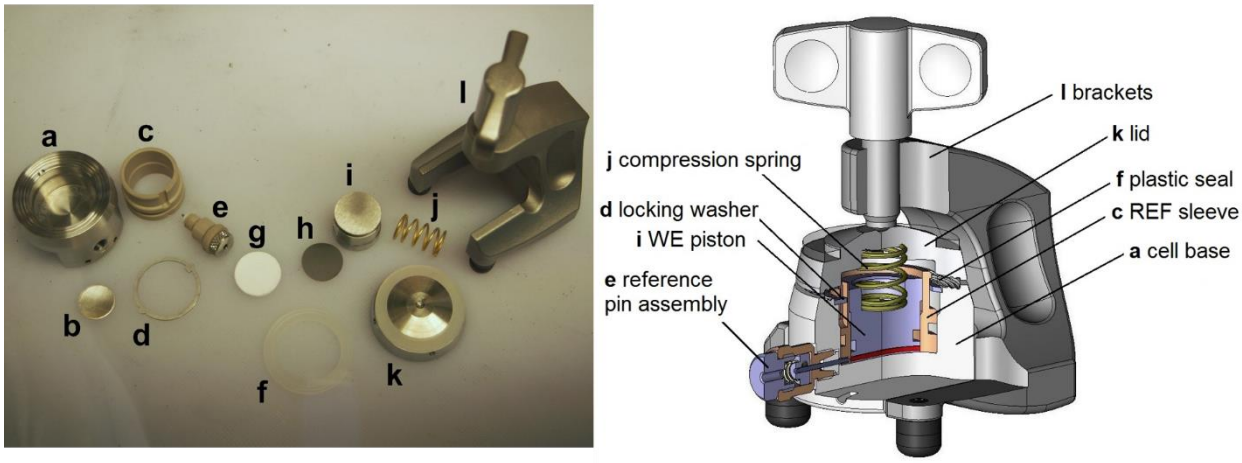

*Figure 3.3: Left: Photograph of the different cell components. Right: Illustration of the interior of an assembled cell, with modification from [64]. Cell components included in a 3-E cell are: **a** cell base, **b** lithium metal disc, **c** REF sleeve, **d** locking washer, **e** reference pin assembly, **f** plastic seal, **g** separator, **h** carbon electrode, **i** WE piston, **j** compression spring, **k** lid, and **l** brackets.*

In the cell assembly the first step was to cut a 14 mm diameter Li metal disc (0.75 mm thick, 99.9 %, Alfa Aesar). The disc was brushed on both sides for removal of any surface film before being placed into the cell base. The prepared REF sleeve was placed in the cell base in such a way that the feed-through hole matched the REF hole in the base and fixed in that position using the locking washer. The reference pin assembly was then attached to the side opening of the cell base. A 18 mm diameter glass fiber separator (Glass fiber separator, 1.55 mm thick, EL-CELL) was placed on top of the Li disc in order to avoid direct contact between the two electrodes. The plastic seal was put on top of the base part. Electrolyte was added to the separator until it was completely soaked with electrolyte; the total electrolyte volume was 440-460 µL. Carbon electrode of 16 mm diameter were punched from the tape casted electrodes, and both thickness and weight were measured. The carbon electrode was placed on top of the separator. To obtain good contact between electrolyte, separator and electrode, the WE piston was placed on top of the current collector, and compressed by the compression spring, the lid was attached, and the whole cell was placed into the brackets and tightened.

3.4.3 *In situ* XRD cell

A special designed cell was assembled for the *in situ* XRD measurements. The cell is the same as Zhou et al. [65] used in their study of *in situ* XRD and EIS of a nanoporous Li_2FeSiO_4/C cathode during the initial charge/discharge cycle of a Li-ion battery, and was designed based on the cell design of Leriche et al. [66]. A photograph and a principal sketch of the *in situ* XRD cell is given in Figure 3.4.

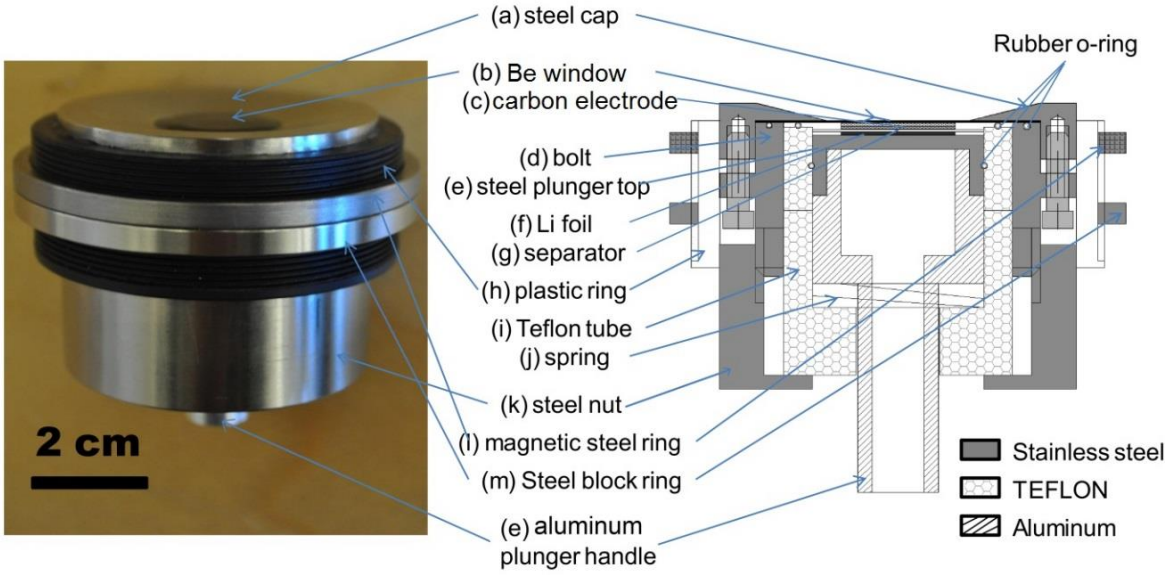

Figure 3.4: Left: Photograph of the in situ XRD cell. Right: Illustration of the cell interior showing the stacking order of the different cell components, with arrows indicating the position of each. With modifications from [67].

First step in the cell assembly was to take the steel cap containing a hole in the middle and cover it up with a 40 mm diameter beryllium window, which contribute to the mechanical stability of the cell and acts as the X-ray window. With the carbon coated side facing way from the Be window, the kapton electrode was placed on top of the Be disc. It was then fixed using a steel bolt with an O-ring, and four screws. The steel bolt also ensures electrical contact between carbon electrode and the potentiostat, through wires which were in contact with the steel nut using copper tape. Another purpose of this steel bolt is to make sure that no air is getting into the cell, while the Teflon tube with an O-ring facing the carbon electrode prevents the electrolyte to get in contact with both the Be window and the steel bolt.

The electrolyte was then added in two portions, 20 µL on top of the carbon, and 10 µL onto a 24 mm diameter microporous trilayer polymeric membrane (Celgard 2320, 20 µm thick, Celgard®). A 16 mm diameter Li metal disc was cut out from a lithium foil (0.75 mm thick, 99.9 %, Alfa Aesar), brushed on both sides before being placed on the steel top of the aluminum plunger handle. In order to make sure that the different components were in good contact with each other a spring was added to the Al plunger handler. Direct contact between the aluminum plunger handle and the steel nut, which is in direct contact with the carbon electrode and Li metal disc, respectively, was avoided by adding a second Teflon

tube to cover up the spring before placing the steel nut on top. In the end the cell was tightened by rotating the plastic rings while avoiding toughing the magnetic steel ring and the steel blocing ring, since these are only used for adjusting the height of the cell for XRD instrument alignment purpose.

The conducted *in situ* XRD measurements, combining galvanostatic cycling and XRD will be described in a later section. The specification of cycling conditions and equipment used will be presented in the section called Powder X-ray diffraction *and in* situ X-ray diffraction while the following section only deals with pure electrochemical cycling, presenting the different test programs.

3.5 Electrochemical techniques

Each of the presented cells have been used in combination with different electrochemical techniques. Coin cells were cycled galvanostatically using a Maccor computer controlled potentiostat (Model 4200), and the cell impedance was measured using ZAHNER-Elektrik® IM6e potentiostat. For the assembled 3-E cells, two different computer controlled potentiostats were utilized: 1) Parstat 4000 (Ametek), and 2) BioLogic VMP3 (Versatille Mulitchannel Potentiostat) multichannel potentiostat.

Since the Parstat potentistat was connected to a temperature chamber the cells cycled using this potentiostat were operated at a constant temperature of 25 °C while all the other cells were cycled at room temperature, assumed to be approximately 25 °C.

3.5.1 Galvanostatic cycling

In order to verify the reproducibility of the data obtained from the galvanostatic testing, at least three parallels of each cell composition were cycled. Since there are some uncertainties regarding maximum capacity related to anion intercalation in carbon materials, the following *high-voltage current program* adopts specific current instead of C-rates (a measure of the current required to charge the cell completely in one hour). The specific current increases with increasing cycle number, corresponding in some extent with the current in a practical Li-ion battery where the negative carbon electrode requires initially low current in order to form a stable SEI.

High-voltage current program:

1. Initial charging step at 10 mAg^{-1} from open-circuit voltage (OCV) to 5.0 V vs. Li^+/Li
2. Discharge step at 10 mAg^{-1} from 5.0 V vs. Li^+/Li to 3.0 V vs. Li^+/Li
3. One additional cycle at 10 mAg^{-1} in the potential range of 3.0-5.0 V vs. Li^+/Li
4. Two cycles between 3.0 – 5.0 V vs. Li^+/Li at rate 20 mAg^{-1}
5. Two cycles between 3.0 – 5.0 V vs. Li^+/Li at rate 50 mAg^{-1}
6. Two cycles between 3.0 – 5.0 V vs. Li^+/Li at rate 100 mAg^{-1}

3.5.2 Cyclic voltammetry

The program used to test the 3-E cells using CV are provided in the following test procedure named *high-voltage CV program*.

High-voltage CV program:

1. Start potential for the testing procedure equaled the cells OCV
2. Voltage was changed in anodic direction to a cut-off voltage equal 5.5 V vs. Li^+/Li at a sweep rate of 0.1 mVs^{-1}
3. In the reverse scan (cathodic direction) the voltage was changed until it reached the cut-off voltage of 3.0 V vs. Li^+/Li using a sweep rate of 0.1 mVs^{-1}
4. Four additional cycles at a sweep rate of 0.1 mVs^{-1} in the potential range of 3.0 – 5.5 V vs. Li^+/Li
5. End potential was set equal to 3.0 V vs. Li^+/Li

Two 3-E cells with either KS6 or Graphene AO-2 as the positive electrode were cycled to an anodic cut-off voltage set to 4.7 V vs. Li^+/Li, while one cell containing Super P Li electrode was cycled to a lower cathodic cut-off voltage, equal 1.5 V vs. Li^+/Li compared to the ones presented in *high-voltage CV program*. Other parameters remained the same.

3.5.3 Electrochemical impedance spectroscopy

High frequency impedance measurements were conducted in order to reveal the coin cell impedance, only those displaying low impedance (~5 Ω) were cycled galvanostatically. 3-E cells were tested at OCV using a potentiostatic impedance spectroscopy technique; a

potential wave with the amplitude of 5.0 mV were impressed on the system in a frequency range of 10 mHz – 1 MHz.

3.6 Characterization techniques

Two different techniques were used to characterize the carbon materials, in the state of powder and carbon electrodes.

3.6.1 Powder X-ray diffraction and *in situ* X-ray diffraction

The analysis of the carbon powders were conducted to reveal information about interlayer spacing and crystallite height perpendicular to the basal plane. The data were obtained using a Bruker D8 DaVinci diffractometer equipped with a Cu-Kα source having a wavelength equal 1.54060 Å. The samples were scanned in a region of 2θ equal 10-90° using a Bragg-Brentano collection mode, and evaluated using TOPAS Rietveld analysis software.

Structural behavior of the carbon electrode containing either KS6 or Graphene AO-2 as the active material was examined *in situ* during galvanostatic cycling, using a Bruker D8 Advance diffractometer. Data were mainly collected in a short 2θ range of 10-45° for KS6 and 7-45° for Graphene AO-2, the time was set to two minutes for one scan. The diffractometer was equipped with a Cu-Kα source having a wavelength equal to 1.54060 Å, Våntec PSD, and was run in Bragg-Brentano collection mode.

For the galvanoststic cycling, the current program used was the same as previously described, *high-voltage current program*, except from the addition of an extra rest step of one second between each charge and discharge step, in order for the potentiostat to correspond to the current change.

3.6.2 Scanning electron microscopy

The carbon materials were studied using a Zeiss Supra, 55 VP low vacuum field emission scanning electron microscope (LVFESEM); powders of all three types of carbon, pristine electrodes, and analysis of kapton based electrodes studied by *in situ* XRD. Prior to study,

the cycled electrodes were washed in DMC in order to remove some of the cycling products on the electrode surface, before being dried in air.

The sample holder was prepared in air by attaching the powders or electrode cast onto a conductive adhesive carbon tape. In the case of cycled electrodes additional carbon tape had to be placed in contact with the carbon cast onto the electrical isolating kapton film in order to avoid sample charging. For study of Super P Li particle shape, a pristine cast was used instead of pure powder in order to eliminate the large differences in sample height. In addition, the sample was gold coated using an Edwards Sputter Coater S150B. The prepared sample holder was transported to the instrument and the operating parameters were adjusted. The micrographs were taken using a secondary electron detector, accelerating voltage in the range of 3.0-5.0 kV, aperture diameter equal 20-30 µm, and a working distance of 6.1-6.5 mm.

3.7 Experimental matrix

In the following table, a summary of all cycled cells are given in terms of carbon electrode material, electrolyte composition and type of cell.

Table 3.3: Experimental matrix providing an overview of all cycled cells.

		Electrolyte composition			
Carbon material		*30:70 vol% EC/DMC 1 M $LiPF_6$*	*30:70 vol% EC/DMC 1 M $LiPF_6$ 1 wt% THFIPB*	*1:1 vol% EC/DMC 1 M $LiPF_6$*	*1:1 vol% EC/DMC 1 M $LiPF_6$ 1 wt% THFIPB*
	KS6	**KS6_30/70 cells**: coin cell x3 3-E cell x1 *in situ* XRD cell x3	**KS6_AR30/70 cells:** coin cell x3 3-E cell x1	**KS6_1/1 cells:** coin cell x3	**KS6_AR1/1 cells:** coin cell x3
	Graphene AO-2	**AO-2_30/70 cells**: coin cell x3 3-E cell x2 *in situ* XRD cell x1	**AO-2_AR30/70 cells:** coin cell x3 3-E cell x1	**AO-2_1/1 cells:** coin cell x3 3-E cell x1	**AO-2_AR1/1** cells: coin cell x3
	Super P Li	**SP_30/70 cells:** coin cell x3 3-E cell x2	**SP_AR30/70 cells:** coin cell x3 3-E cell x1	-	-

4 Results

This chapter provides the results obtained from the carbon powder characterization, electrochemical cycling and *in situ* XRD measurements, in this order. In the first section scanning electron micrographs and XRD results of the carbon powders are presented. The second chapter will provide results from the galvanostatic cycling and CV analysis of carbon electrodes in various electrolyte compositions. In the last section, *in situ* XRD measurements will be presented as the combination of potential curves and XRD spectra. To get a better understanding of the electrode performance additional SEM images are also given.

4.1 Carbon powder characterization

Particle shape and size of the three carbon materials were studied and estimated based on scanning electron micrographs, provided in Figure 4.1. Additional XRD analysis of the powders were conducted, and full scan XRD spectra for each type of carbon powder are presented in the same plot with a fixed y-offset in Figure 4.2.

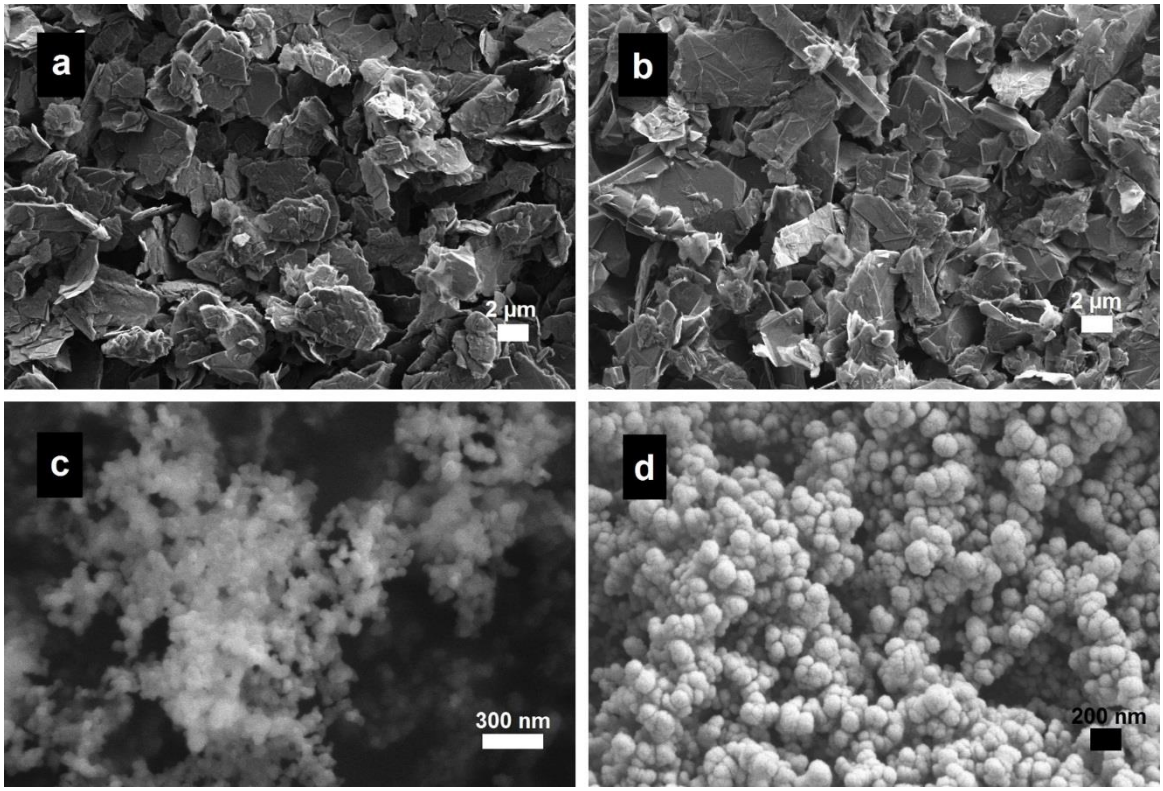

*Figure 4.1: Scanning electron micrographs of various carbon powders: **a** KS6, **b** Graphene AO-2, and **c** Super P Li. Image **d** shows a gold sputtered electrode cast containing 90 wt% Super P Li + 10 wt% PVDF. All micrographs were taken using secondary electron detector, working distance equal 6.2 mm, and an accelerating voltage of 3.0 kV in the case of KS6 and Graphene AO-2 and 5.0 kV for images of Super P Li.*

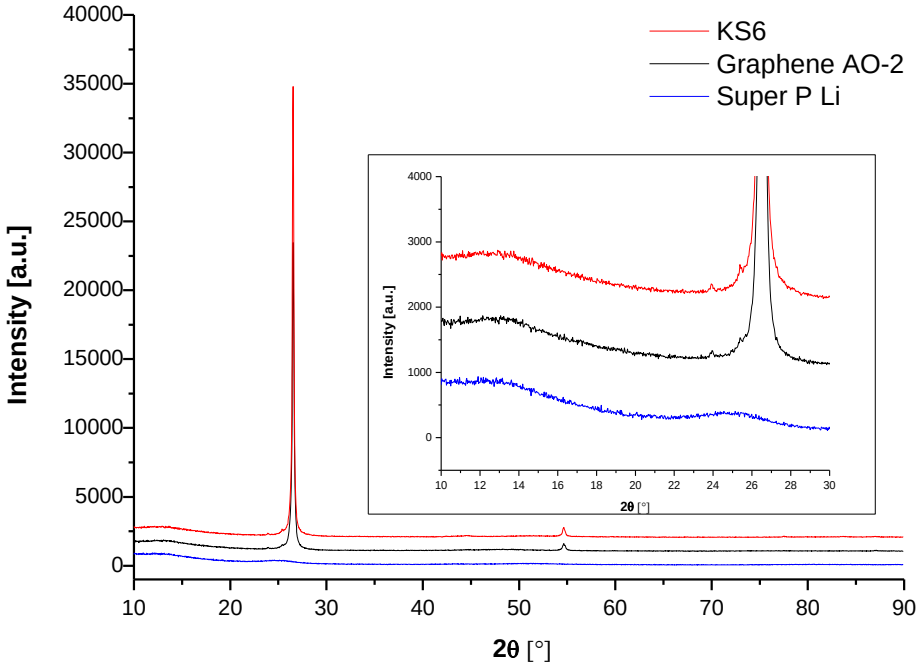

Figure 4.2: XRD spectra for Super KS6, Graphene AO-2, and Super P Li powder in the scattering angle region of 10-90°. The insert display the spectra in the scattering angle region of 10-30°.

Based on the above micrographs named *a-c*, particle size was estimated to be 4 µm for KS6, 3 µm for Graphene AO-2 and 48 nm for Super P Li. The technical data provided in Table 3.1 indicating a broad particle size distribution for Graphene AO-2. The estimation of a relatively large particle size might be due to that mainly the larger particles are visible in the micrograph. In the case of particle shape, image *d* clearly shows that Super P Li consists of spherical particles, while the Graphene AO-2 particles are more flaky with shaper edges compared to the KS6 powder particles.

The full scan XRD spectra clearly shows a high intensity peak for both KS6 and Graphene AO-2 appearing at the scattering angle related to the (002) planes. The inset displays only the scattering angles below the high intensity peak. At these scattering angles there is no observable differences between the spectra for KS6 and Graphene AO-2. In contrast, only broad peaks with low intensities are observed in the XRD spectra for Super P Li.

In addition, quantitative analysis of the carbon powder structure were based on the XRD measurements, estimating both the values for interlayer spacing and crystallite size perpendicular to the basal plane. The values were calculated using equation (2.7) and equation (2.8), respectively and are given in Table 4.1. Included are also the measured values for scattering angle and full-width half-maximum intensity (FWHM) for diffraction peak corresponding to the (002) planes. Both the peak position and values for FWHM were obtained by curve fitting using TOPAS software. The raw data along with the fitted curve and the difference between the two curves, are plotted for each carbon powder and given in **Appendix C**. It has to be stressed that the measured values obtain uncertainties due differences in sample preparation and instrument alignment.

Table 4.1: Measured values for scattering angle and FWHM (β), and calculated values for interlayer spacing and crystallite height along the c-axis.

	$2\theta_{002}$ [°]	**β [°]**	**d_{002}[4] [Å]**	**L_c (002)[5] [Å]**
KS6	26.527	0.140	3.357	649
Graphene AO-2	26.531	0.168	3.357	539
Super P Li	25.194	3.020	3.532	30

[4] Parameters used in the calculations: λ=1.54060 Å and n=1.
[5] Parameters used in the calculations: λ=1.54060 Å and K=1.00.

4.2 Electrochemical techniques

This section provides data obtained from the electrochemical testing, included are galvanostatic cycling and cyclic voltammetry at different current densities and in various potentials ranges.

The experimental matrix given in Table 3.3 presents all cell combinations tested. Since three parallels have been cycled galvanostatically, these results will mainly be given as an average with standard deviation, while the CV results are based on single measurements. Before the results are presented, the next section will give an overview of electrode characteristics for Al based electrodes. In the case of kapton based electrodes, these will be presented in the section named ***In situ* X-ray diffraction**.

4.2.1 Carbon electrodes

Parameters describing the three types of carbon electrodes based on Al current collector, in addition to estimation of active electrode surface based on EIS measurement will be presented in the following two sections.

4.2.1.1 Electrode characteristics

Table 4.2 provide information about the three types of cycled carbon electrodes. The values displayed are average of all electrodes cycled in the same electrolyte composition, including electrodes used in both coin cells and 3-E cells.

Table 4.2: Overview of electrode characteristics for carbon electrodes based on Al current collector, presented as average values.

Carbon material	Electrolyte composition	Thickness carbon layer [µm]	Active material loading [mgcm^{-2}]	Pore fraction[6] [%]
KS6	30/70	83	5.1	68.8
	1/1	81	5.1	68.0
	AR30/70	85	5.2	69.1
	AR1/1	83	5.3	67.7
Graphene AO-2	30/70	78	3.0	80.4
	1/1	46	1.9	78.8
	AR30/70[7]	78	3.0	80.7
	AR1/1	45	1.9	78.1
Super P Li	30/70	44	1.2	84.8
	1/1	38	1.1	84.5

The values given in the above table state that there is a clear difference between the electrode characteristics. Electrodes containing KS6 are thickest, the type of electrode with the largest active material loading, but has the smallest pore fraction. In contrast, electrodes containing Super P Li are the thinnest ones, have much lower active material loading, but the largest pore fraction. The electrode characteristics for Graphene AO-2 electrodes having values between those for KS6 and Super P Li. It should be noted that the electrode characteristics for Graphene AO-2 differs for different electrolyte compositions, due to the use of two different electrode casts prepared from two carbon slurries which obtained quite different viscosities. However, in case of galvanostatic cycling, when comparing the effect of the addition of anion receptor to the electrolyte, electrodes were always chosen from the same cast.

4.2.1.2 Electrochemical impedance spectroscopy – active electrode area

The active surface area of Super P Li and KS6 electrodes have been estimated based on the observation of almost capacitive behavior of the Nyquist plot at low frequencies (neglected the intercalation reaction since the analysis were conducted at open-circuit voltage (OCV)),

[6] In the estimation of pore fraction, both carbon powder and PVDF were taken into consideration by using the following density values: $\rho_{Graphene\ AO\text{-}2} \approx \rho_{KS6} = 2.27$ gcm^{-3} [2] , $\rho_{Super\ P\ Li} = 2.1$ gcm^{-3} [68], and $\rho_{PVDF} = 1.74$ gcm^{-3} [69].
[7] One type of electrode cast was used for one of the cycled 3-E cells, while another electrode cast was used for rest of the cells cycled with the specific electrolyte composition. Since the electrode characteristics for the two Graphene AO-2 casts are so different, the one electrode which differs from the rest has been neglected in the calculations of the average electrode parameters.

as shown in Figure 4.3 and Figure 4.4, respectively. The values obtained are given in Table 4.3, calculated using equation (2.6).

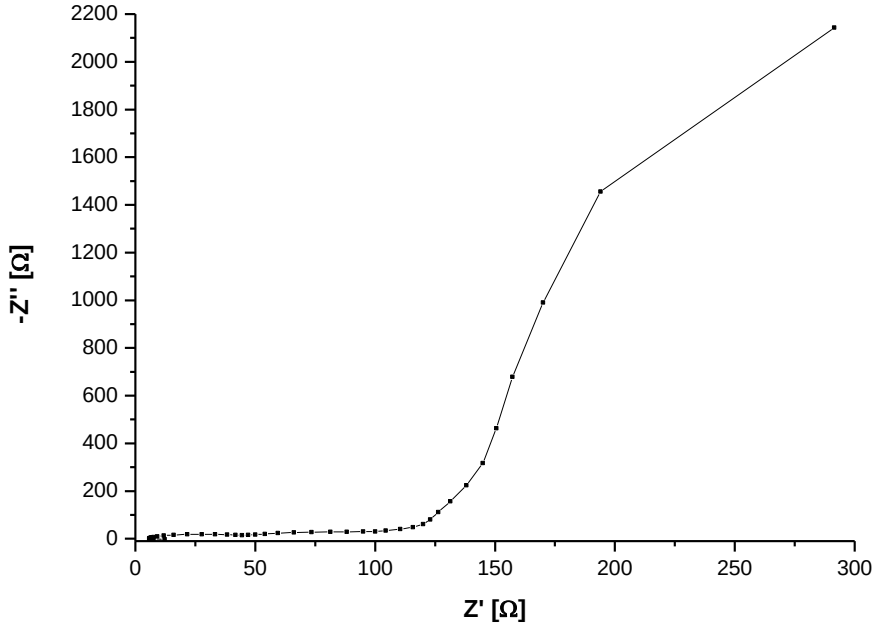

Figure 4.3: Nyquist plot for Super P Li electrode exposed to 30:70 vol% EC/DMC 1 M $LiPF_6$ (cell SP_30/70_2), measured at OCV in a frequency range of 0.01 Hz – 1 MHz.

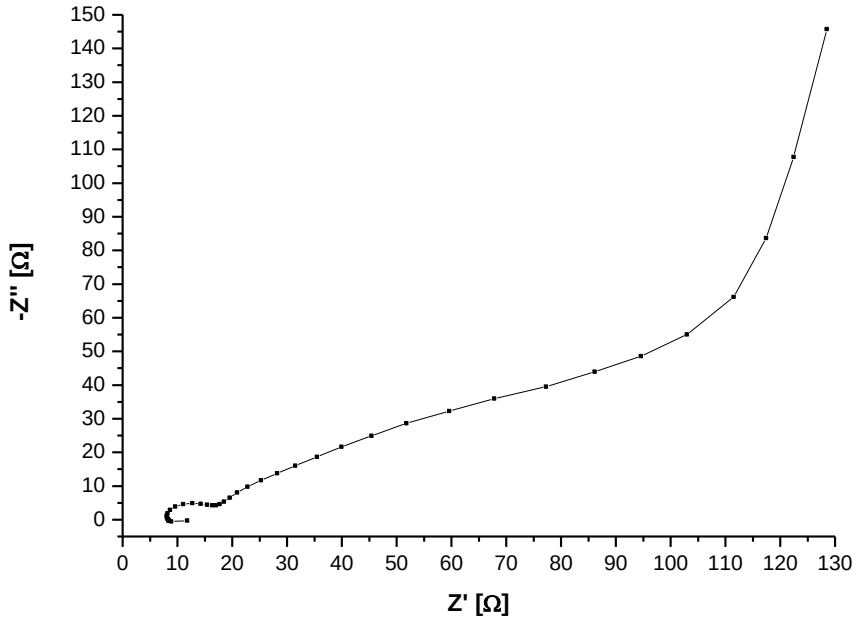

Figure 4.4: Nyquist plot for KS6 electrode exposed to 30:70 vol% EC/DMC 1 M $LiPF_6$ (cell KS6_30/70_2), measured at OCV in a frequency range of 0.1 Hz – 1 MHz.

Table 4.3: Measured and calculated values for frequency, imaginary impedance, capacitance and specific electrode surface area.

	KS6 + 30:70 vol% EC/DMC 1 M $LiPF_6$ (cell KS6_30/70_2)	**Super P Li + 30:70 vol% EC/DMC 1 M $LiPF_6$ (cell SP_30/70_2)**
f [Hz]	0.100	0.010
-Z'' [Ω]	145	2143
C [F]	0.0109	0.0074
A[8] [m^2g^{-1}]	13.95	40.71

4.2.2 Galvanostatic cycling

Several combinations of carbon electrode and electrolyte have been cycled galvanostatically. The results are divided into sections regarding the electrolyte composition. Potential curves, capacity diagrams, and tables with Coulombic efficiencies will be presented.

It should be noted that the standard deviation for C_{eff} at high current densities (50 mAg^{-1} and 100 mAg^{-1}) clearly display large uncertainties in some of the measured capacity values, caused by the collection of too few data points while cycling. These values are not included in the following tables presenting the values of C_{eff}.

4.2.2.1 30:70 vol% EC/DMC 1 M $LiPF_6$

Potential curves for the first three cycles of *high-voltage current program*, presented as voltage vs. specific capacity for KS6, Graphene AO-2 and Super P Li are given in Figure 4.5, Figure 4.6 and Figure 4.7, respectively. While the specific capacity values, both charge and discharge are given as capacity diagrams in Figure 4.8 for KS6, Figure 4.9 for Graphene AO-2 and Figure 4.10 for Super P Li.

[8] Estimation of electrode surface area is based on the observation of a pure capacitor-like behavior at low frequencies. In the calculations, the lowest measured frequency, with the corresponding -Z'' values were used in order to get an estimate of the capacitance related to charging of the electrical double layer. The electrode area was estimated assuming the same capacitance value measured in the work of Laheäär et al. [70], who investigated the electrochemical characteristics of micro porous titanium carbide derived carbon symmetrical supercapacitor in 1:1 vol% EC/DMC 1 M $LiPF_6$ electrolyte. They reported a capacitance value of approximately 7.597E-6 Fcm^{-2}.

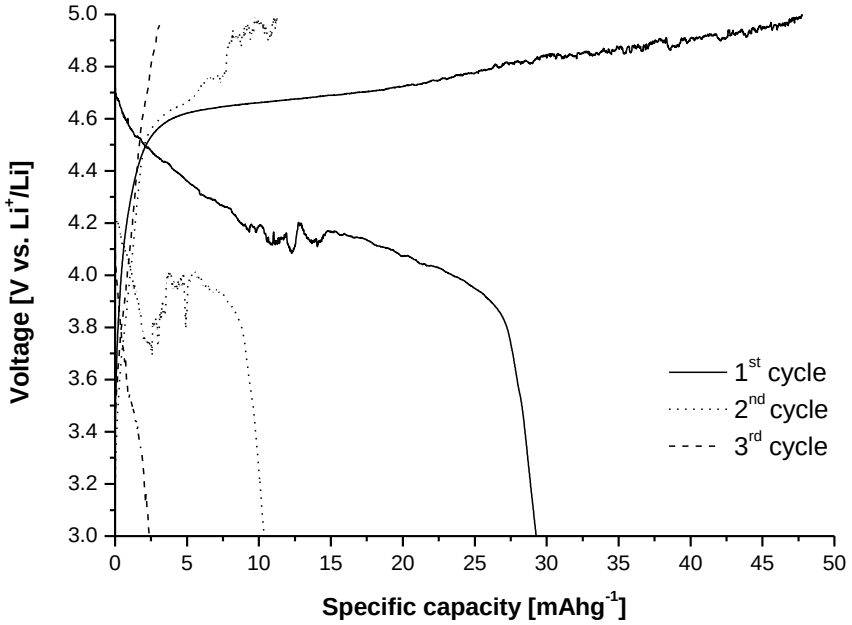

Figure 4.5: Potential vs. specific capacity during galvanostatic cycling of KS6 (cell KS6_30/70_4), in a potential range of 3.0-5.0 V vs. Li^+/Li with a current density of 10 mAg^{-1} for 1st cycle and 2nd cycle, and 20 mAg^{-1} for 3rd cycle.

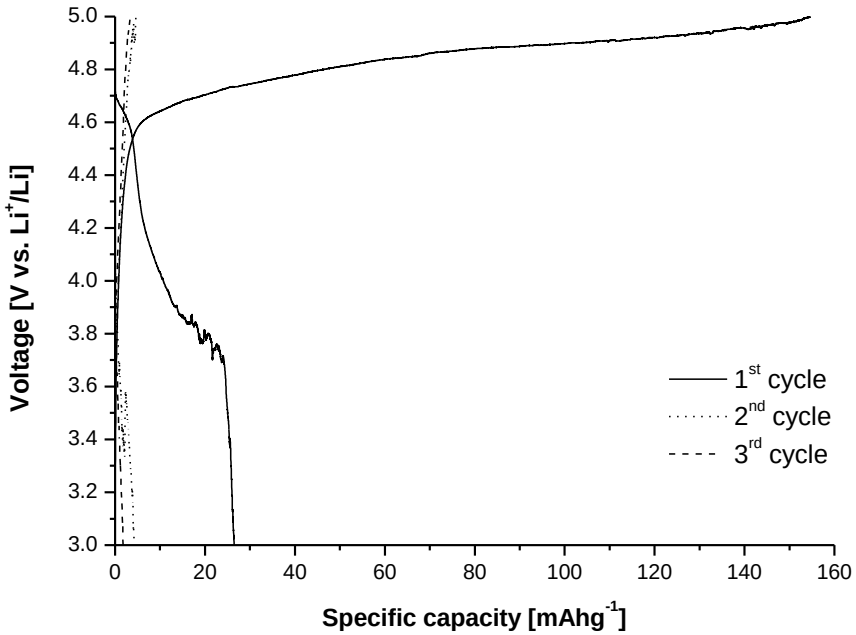

Figure 4.6: Potential vs. specific capacity during galvanostatic cycling of Graphene AO-2 (cell AO-2_30/70_2), in a potential range of 3.0-5.0 V vs. Li^+/Li with a current density of 10 mAg^{-1} for 1st cycle and 2nd cycle, and 20 mAg^{-1} for 3rd cycle.

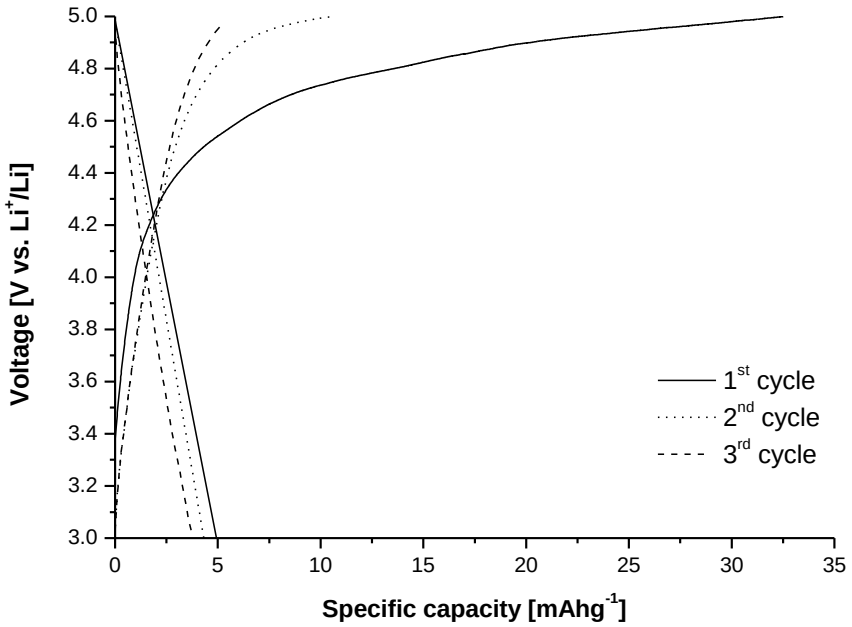

Figure 4.7: Potential vs. specific capacity during galvanostatic cycling of Super P Li (cell SP_30/70_5), in a potential range of 3.0-5.0 V vs. Li^+/Li with a current density of 10 mAg^{-1} for 1st cycle and 2nd cycle, and 20 mAg^{-1} for 3rd cycle.

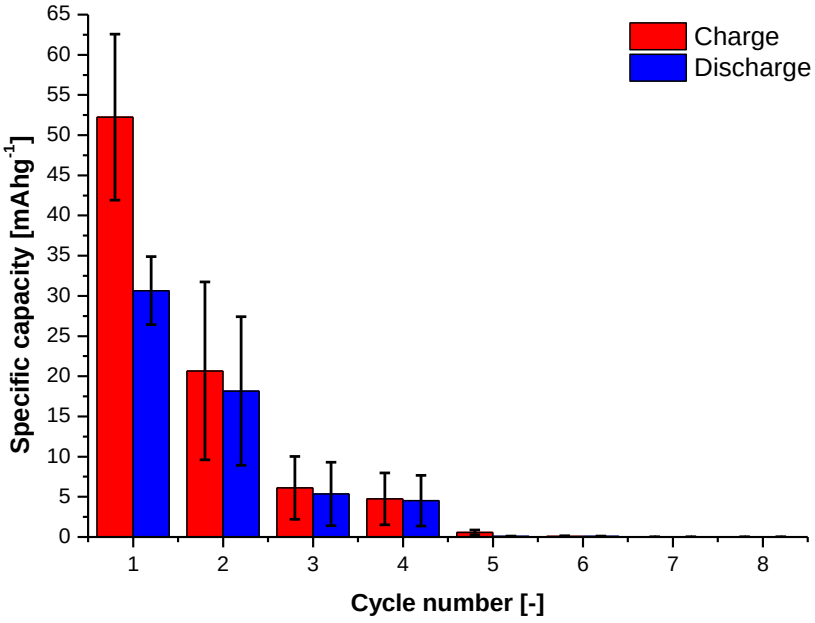

Figure 4.8: Specific capacity diagram presented as average specific charge capacity (red) and specific discharge capacity (blue) for cycled coin cell combinations of KS6 and 30:70 vol% EC/DMC 1 M $LiPF_6$ (KS6_30/70), using high-voltage current program.

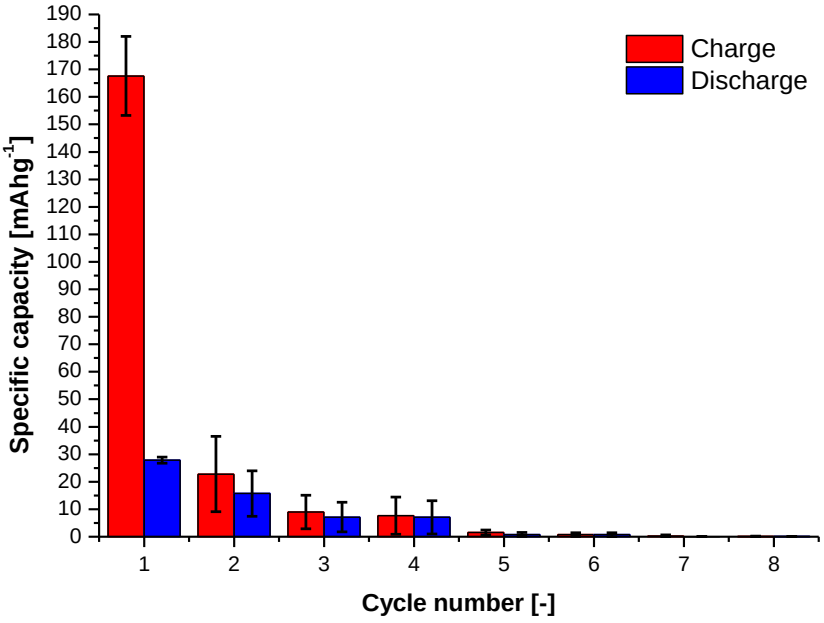

Figure 4.9: Specific capacity diagram presented as average specific charge capacity (red) and specific discharge capacity (blue) for cycled coin cell combinations of Graphene AO-2 and 30:70 vol% EC/DMC 1 M $LiPF_6$ (AO-2_30/70), using high-voltage current program.

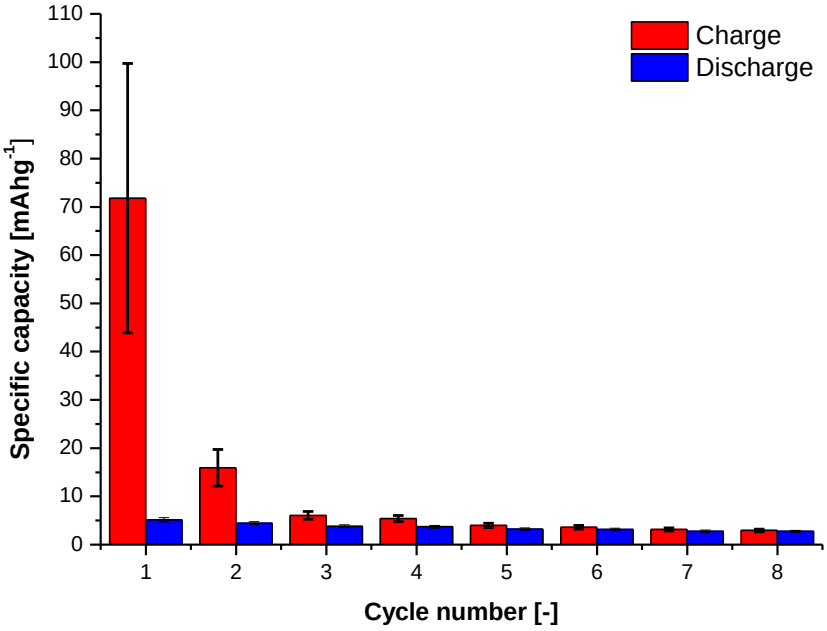

Figure 4.10: Specific capacity diagram presented as average specific charge capacity (red) and specific discharge capacity (blue) for all cycled coin cell combinations of Super P Li and 30:70 vol% EC/DMC 1 M $LiPF_6$ (SP_30/70), using high-voltage current program.

Neither of the presented potential curves show any clear defined potential plateaus, making it difficult to state whether anion intercalate in staged phases or not.

Comparison of the three specific capacity diagrams show a striking difference in the first cycle. Cells with Graphene AO-2 is the one obtaining the highest charge capacity with a value of 167.7±14.4 $mAhg^{-1}$, while the charge capacity for the two other carbon materials is 52.2±10.3 $mAhg^{-1}$ and 30.6±2.2 $mAhg^{-1}$ for KS6 and Super P Li, respectively. In the following discharge step, the capacity for Graphene AO-2 and KS6 are the ones being the most similar, with the values of 27.9±1.1 $mAhg^{-1}$ and 30.7±4.2$mAhg^{-1}$, respectively. These values are thus relatively large compared to 3.8±0.8 $mAhg^{-1}$ for Super P L. However, Super P Li displays relative stable discharge values in all eight cycles. Values for Ceff were calculated by using equation (2.4) and the just presented specific capacity values. The values obtained are presented in Table 4.4.

Table 4.4: Average values for C_{eff}, including standard deviation, for carbon electrodes containing KS6, Graphene AO-2 and Super P Li cycled in an electrolyte of 30:70 vol% EC/DMC 1 M $LiPF_6$.

	KS6	**Graphene AO-2**	**Super P Li**
Cycle number	C_{eff} *[%]*	C_{eff} *[%]*	C_{eff} *[%]*
1	59.3±3.3	16.7±0.7	8.9±4.5
2	89.1±2.4	76.2±12.1	29.8±7.9
3	82.5±8.3	73.5±14.0	63.3±3.6
4	93.6±6.0	94.1±4.7	68.7±3.3
5	NA	NA	80.6±2.2
6	NA	NA	87.4±2.1
7	NA	NA	87.6±2.2
8	NA	NA	93.7±1.5

Form the above table, there is some differences to be noticed. During the first charging step more than half of the charging (i.e. anodic) current in the system consisting of KS6 is related to anion intercalation. Most of the charge current in the cells consisting of Graphene AO-2 or Super P Li is related to irreversible reactions, probably electrolyte oxidation. While in the second cycle, irreversible reactions are still significant to Super P Li. However, for the cells with KS6 and Graphene AO-2 a much higher fraction of the charge current is related to anion intercalation compared to the first cycle.

4.2.2.2 1:1 vol% EC/DMC 1 M $LiPF_6$

Only KS6 and Graphene AO-2 were cycled in combination with this electrolyte composition. The assemble cells consisting of Super P Li displayed too high cell impedance, probably due to the use of a different separator which is incompatible with the given electrolyte. The data obtained for galvanostatic cyling using *high-voltage current program* are presented as capacity diagrams in Figure 4.11 and Figure 4.12 for KS6 and Graphene AO-2, respectively. The corresponding C_{eff} values, calculated using equation (2.4), and the standard deviations are given in Table 4.5.

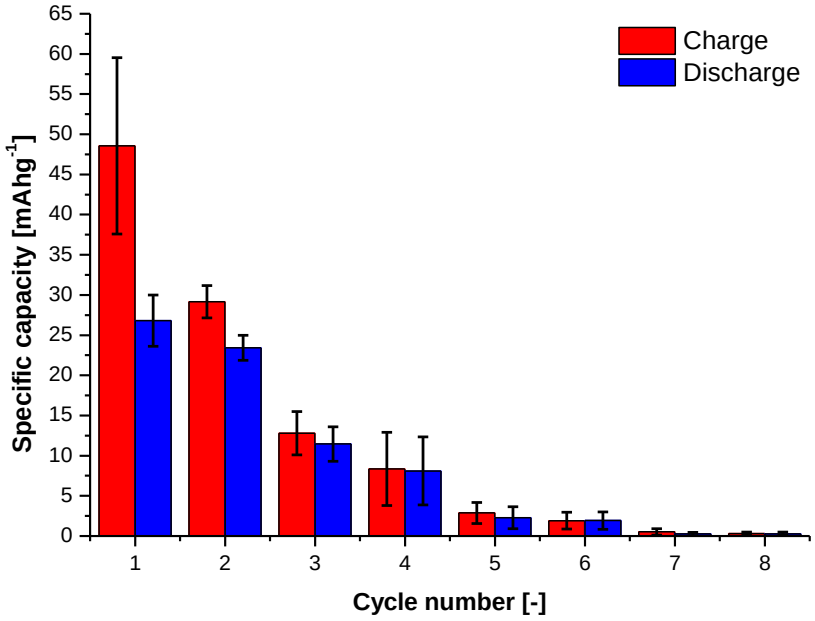

Figure 4.11: Specific capacity diagram presented as average specific charge capacity (red) and specific discharge capacity (blue) for cycled coin cell combinations of KS6 and 1:1 vol% EC/DMC 1 M $LiPF_6$ (KS6_1/1), using high-voltage current program.

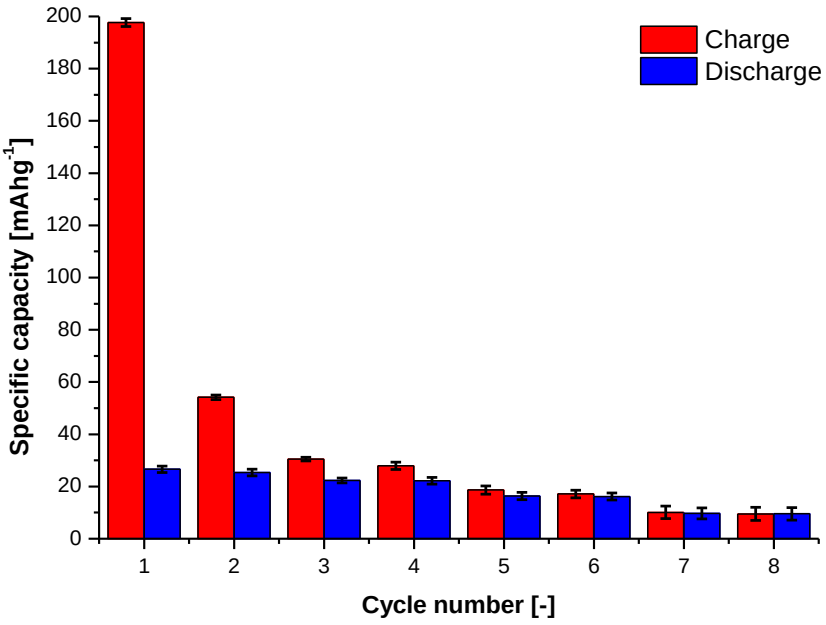

Figure 4.12: Specific capacity diagram presented as average specific charge capacity (red) and specific discharge capacity (blue) for cycled coin cell combinations of Graphene AO-2 and 1:1 vol% EC/DMC 1 M $LiPF_6$ (AO-2_1/1), using high-voltage current program..

The capacity diagrams show a different electrochemical behavior for the two carbon materials. KS6 obtain a capacity value of 48.6±11.0 $mAhg^{-1}$ in contrast to the value of Graphene AO-2 being 197.6±1.5$mAhg^{-1}$ for the 1st charge step. In the following discharge step they behave very similar, 23.4±1.6 $mAhg^{-1}$ for KS6 and 26.6±1.2 $mAhg^{-1}$ for Graphene AO-2. The results for Graphene AO-2 in the subsequent cycles show quite large and stable capacity values at high current densities. Obtaining values of 18.6±1.6 $mAhg^{-1}$ for the 5th charge step and 16.4±1.4 $mAhg^{-1}$ for 5th discharge step.

Table 4.5: Average values for C_{eff}, including standard deviation, for electrodes consisting of KS6 and Graphene AO-2 cycled in an electrolyte of 1:1 vol% EC/DMC 1 M $LiPF_6$.

	KS6	**Graphene AO-2**
Cycle number	*C_{eff} [%]*	*C_{eff} [%]*
1	56.5±5.7	13.5±0.7
2	80.3±0.6	46.8±2.6
3	89.9±2.1	73.3±1.8
4	98.1±2.2	79.5±1.9

The calculated C_{eff} values, given in Table 4.5, display same trends as observed in Table 4.4.

4.2.2.3 30:70 vol% EC/DMC 1 M $LiPF_6$ 1 wt% THFIPB

The effect of adding the anion receptor, THFIPB on the electrode cycling performance was studied for all three carbon materials being cycled using *high-voltage current program*. The measured specific capacity values are presented in Figure 4.13, Figure 4.14 and Figure 4.15 for KS6, Graphene AO-2 and Super P Li, respectively. Based on these diagrams, C_{eff} was calculated using equation (2.4), and the values obtained are given in Table 4.6 along with values for standard deviation.

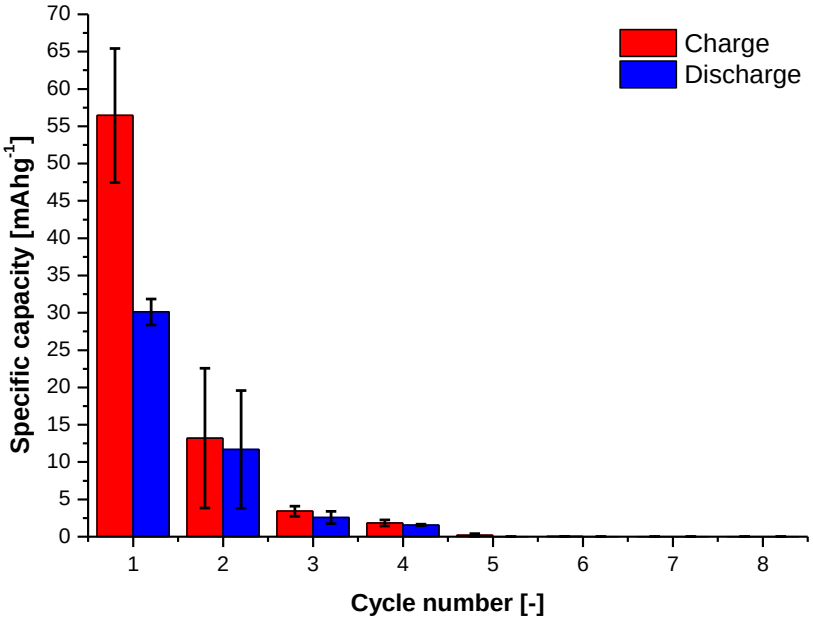

Figure 4.13: Specific capacity diagram presented as average specific charge capacity (red) and specific discharge capacity (blue) for cycled coin cell combinations of KS6 and 30:70 vol% EC/DMC 1 M $LiPF_6$ 1 wt% THFIPB (KS6_AR30/70), using high-voltage current program.

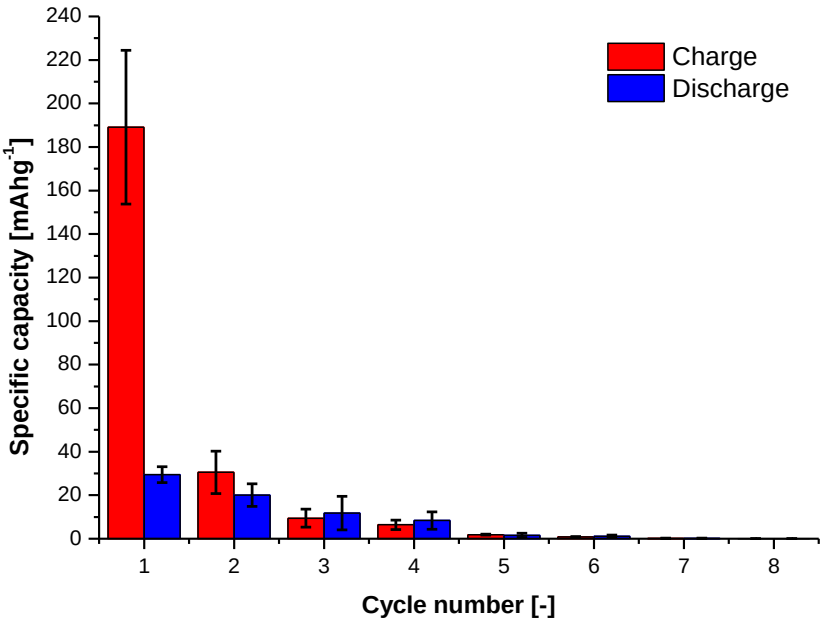

Figure 4.14: Specific capacity diagram presented as average specific charge capacity (red) and specific discharge capacity (blue) for cycled coin cell combinations of Graphene AO-2 and 30:70 vol% EC/DMC 1 M $LiPF_6$ 1 wt% THFIPB (AO-2_AR30/70), using high-voltage current program.

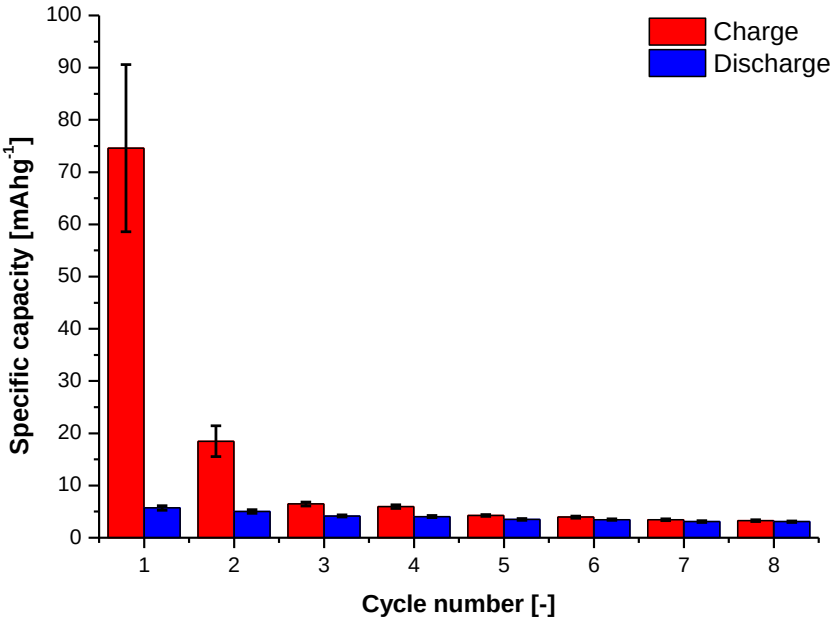

Figure 4.15: Specific capacity diagram presented as average specific charge capacity (red) and specific discharge capacity (blue) for cycled coin cell combinations of Super P Li and 30:70 vol% EC/DMC 1 M $LiPF_6$ 1 wt% THFIPB (SP_AR30/70), using high-voltage current program.

The cells with Graphene AO-2 is the one obtaining the highest 1st charge capacity value of 189.1±35.4 $mAhg^{-1}$, while KS6 has a 1st charge capacity of 56.5±9.0 $mAhg^{-1}$, and Super P Li 74.6±16.0 $mAhg^{-1}$. In the following discharge step Graphene AO-2 displays a capacity value of 29.4±3.6 $mAhg^{-1}$, KS6 equals 30.1±1.7 $mAhg^{-1}$ and Super P Li a value of 5.7±0.4 $mAhg^{-1}$. The discharge capacity for Super P Li are more stable in subsequent cycles compared to KS6 and Graphene AO-2.

Table 4.6: Average values for C_{eff}, including standard deviation, for electrodes consisting of KS6, Graphene AO-2 and Super P Li cycled in an electrolyte of 30:70 vol% EC/DMC 1 M $LiPF_6$ 1 wt% THFIPB.

	KS6	**Graphene AO-2**	**Super P Li**
Cycle number	*C_{eff} [%]*	*C_{eff} [%]*	*C_{eff} [%]*
1	54.4±6.7	20.1±5.4	8.1±2.3
2	90.9±3.2	70.5±5.2	28.1±6.5
3	73.9±10.9	68.2±17.9	64.6±2.0
4	90.1±20.8	92.5±6.6	67.8±2.4
5	NA	NA	82.3±0.9
6	NA	NA	87.8±0.8
7	NA	NA	89.0±0.8
8	NA	NA	93.9±0.6

Comparing the C_{eff} values for cells containing the same type of carbon electrode, same electrolyte, while the only difference is the addition of THFIPB, Table 4.4 and Table 4.6, respectively show no clear changes in behavior.

4.2.2.4 1:1 vol% EC/DMC 1 M $LiPF_6$ 1 wt% THFIPB

Coin cells with KS6 and Graphene AO-2 were cycled with *high-voltage current program*. The capacity values obtained are provided in Figure 4.16 and Figure 4.17, respectively. No cells with Super P Li were cycled due to the same reason as explained in section 4.2.2.2. Based on these capacity diagrams, C_{eff} was calculated using equation (2.4). The calculated values along with standard deviation are given in Table 4.7.

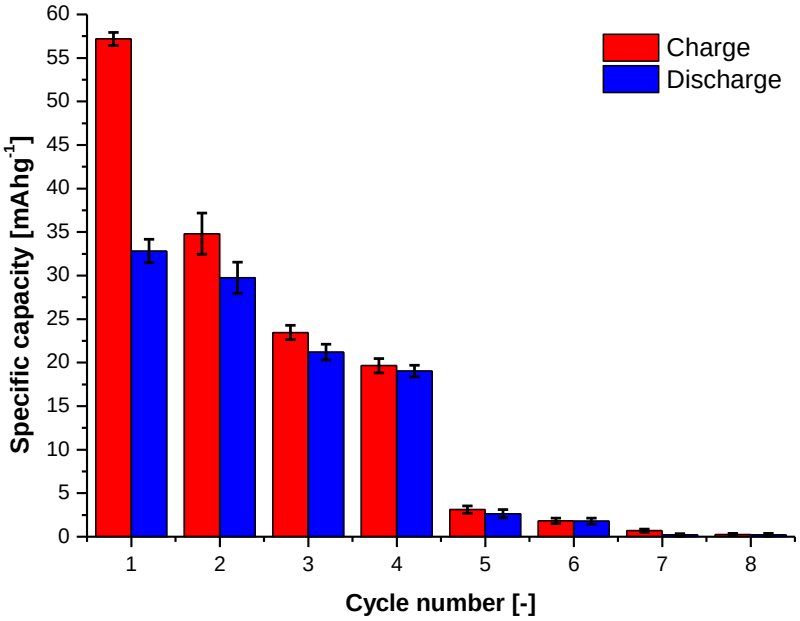

Figure 4.16: Specific capacity diagram presented as average specific charge capacity (red) and specific discharge capacity (blue) for cycled coin cell combinations of KS6 and 1:1 vol% EC/DMC 1 M $LiPF_6$ 1 wt% THFIPB (KS6_AR1/1), using high-voltage current program.

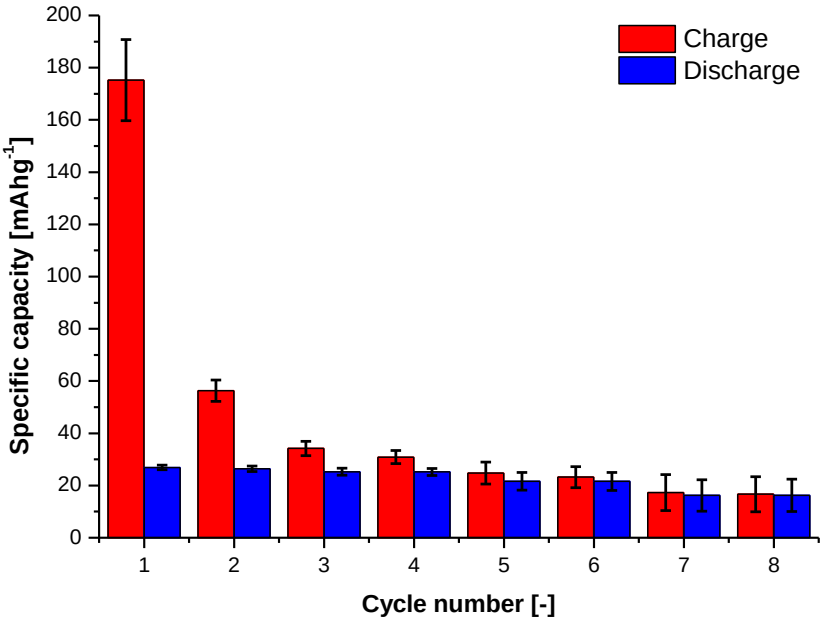

Figure 4.17: Specific capacity diagram presented as average specific charge capacity (red) and specific discharge capacity (blue) for cycled coin cell combinations of Graphene AO-2 and 1:1 vol% EC/DMC 1 M $LiPF_6$ 1 wt% THFIPB (AO-2_AR1/1), using high-voltage current program.

Based on the capacity diagrams just provided, it is observed that KS6 has a 1st cycle charge and discharge capacity equal 57.2±0.7 $mAhg^{-1}$ and 32.8±1.3 $mAhg^{-1}$, respectively. In the case of Graphene AO-2, the measured 1st charge capacity was found to be 173.5±15.5 $mAhg^{-1}$, and discharge capacity was found to be 26.9±0.9 $mAhg^{-1}$. The cells cycled with and without THFIPB added to the electrolyte behaves very similar regarding the capacities obtained in each system during both charge and discharge.

Table 4.7: Average values for C_{eff}, including standard deviation, for electrodes consisting of KS6 and Graphene AO-2 cycled in an electrolyte of 1:1 vol% EC/DMC 1 M $LiPF_6$ 1 wt% THFIPB.

	KS6	**Graphene AO-2**
Cycle number	*C_{eff} [%]*	*C_{eff} [%]*
1	57.4±1.8	15.5±1.4
2	85.5±0.7	47.1±2.7
3	90.3±0.8	74.1±2.9
4	96.8±0.8	81.7±2.7
5	84.3±3.9	87.7±1.3
6	97.3±3.8	93.3±1.6

The same trend as shown in Table 4.5 is observed in the above table. Taking into consideration the standard deviation values, there is no difference in the C_{eff} values for either KS6 or Graphene AO-2 cycled in an electrolyte with composition of 1:1 vol% EC/DMC 1 M $LiPF_6$ and 1:1 vol% EC/DMC 1 M $LiPF_6$ 1 wt% THFIPB.

4.2.3 Cyclic voltammetry

Cyclic voltammetry was conducted in order to investigate the potentials at which the high-voltage reactions are taking place at the various carbon electrodes, in addition to reveal eventually overpotentials related to each process. The measured current values are only of interest to explain changes in subsequent cycles for a given system, not for comparison between different cell systems, because of the dependence on the specific electrode structure and morphology.

All CV curves presented in the next three sections are plotted with cell voltage on the x-axis and the current density, based on the geometric electrode area, on the y-axis. Some curves have been smoothed using Kalman filter, due to small signal-to-noise ratio in the

measured raw data. This only apply to 3-E cells cycled using Parstat 4200. The figures that follow will present the curves being smoothed rather than the curve based on the raw data, and will be indicated in the figure text. For comparison, the 1st cycle curve based on the raw data along with the smoothed curve are plotted together and given in **Appendix D**.

4.2.3.1 High-voltage operation in 30:70 vol% EC/DMC 1 M $LiPF_6$

The 1st cycle CVs recorded for each carbon material tested by *high-voltage CV program* are provided in Figure 4.18, the black square represents a magnified section, given in Figure 4.19. Due to problems with cycling of the KS6 electrode, the result previously obtained by the author [71] is included for comparison. In addition, Figure 4.20 and Figure 4.21 provide all cycles conducted for KS6 and Graphene AO-2, respectively.

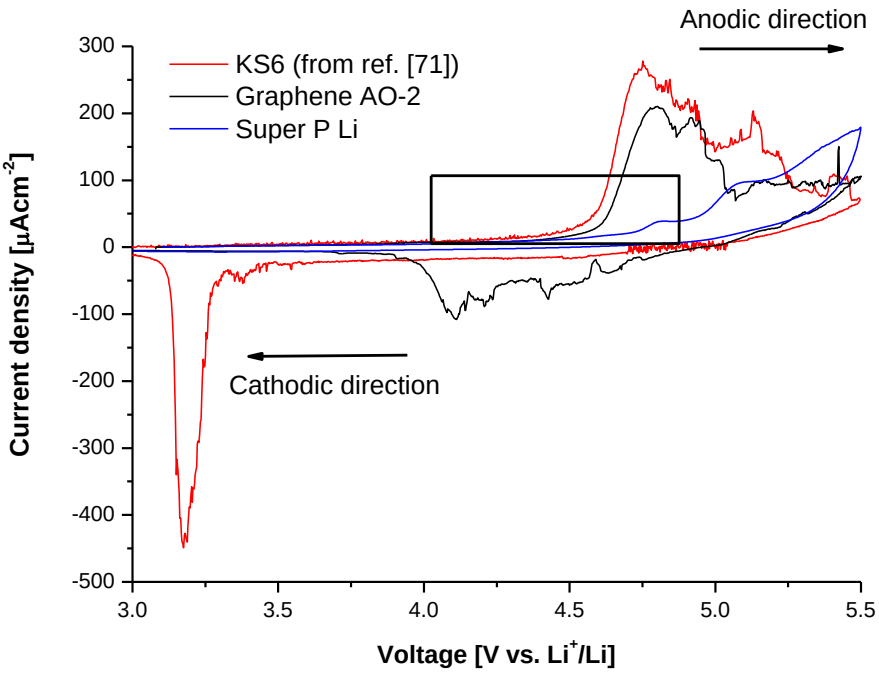

Figure 4.18: Cyclic voltammograms providing the 1st cycle of three cell combinations, containing 30:70 vol% EC/DMC 1 M $LiPF_6$ characterized by carbon material (cell KS6_30/70_CV1, AO-2_30/70_3 and SP_30/70_1). The curves were obtained using high-voltage CV program.

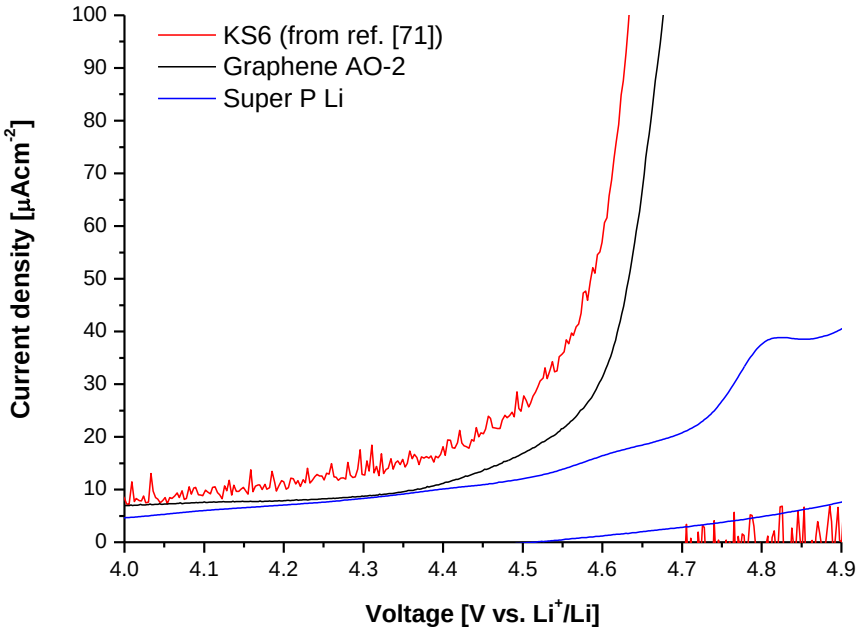

Figure 4.19: Cyclic voltammograms providing the 1st cycle of three cell combinations, containing 30:70 vol% EC/DMC 1 M $LiPF_6$ characterized by carbon material (cell KS6_30/70_CV1, AO-2_30/70_3 and SP_30/70_1). The curves were obtained using high-voltage CV program, but only the voltage region of 4.0-4.9 V vs. Li^+/Li is included.

Several peaks are appearing in all three CV curves as observed in Figure 4.18. The most striking difference, when taking into account peaks appearing in both scanning directions is the absences of a cathodic peak for Super P Li.

The onset oxidation voltage for each carbon material was estimated based on the curves given in Figure 4.19. The voltage was set equal to the intersect with a line at 35 µAcm^{-2} (current density were the slope of all three curves has started to increase significantly), corresponding to a voltage of 4.55 V vs. Li^+/Li for KS6, 4.61 V vs. Li^+/Li for Graphene AO-2 and 4.78 V vs. Li^+/Li for Super P Li. Rather being exact determined onset oxidation potentials, these values are more of an indication of the relative differences in electrochemical activity upon high-voltage operation.

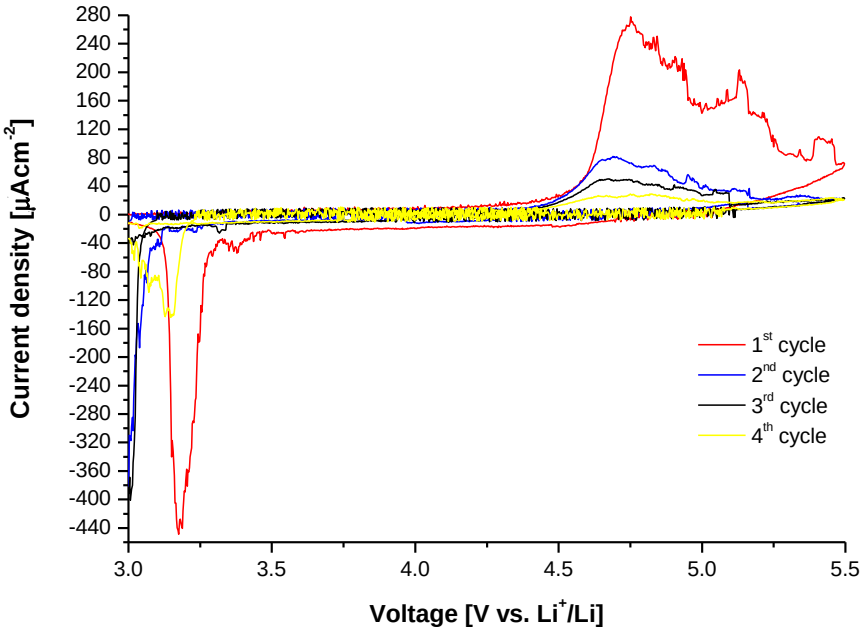

Figure 4.20: Cyclic voltammograms providing all cycles for KS6 in combination with 30:70 vol% EC/DMC 1 M $LiPF_6$ (cell KS6_30/70_CV1) from [71]. The curves were obtained using high-voltage CV program.

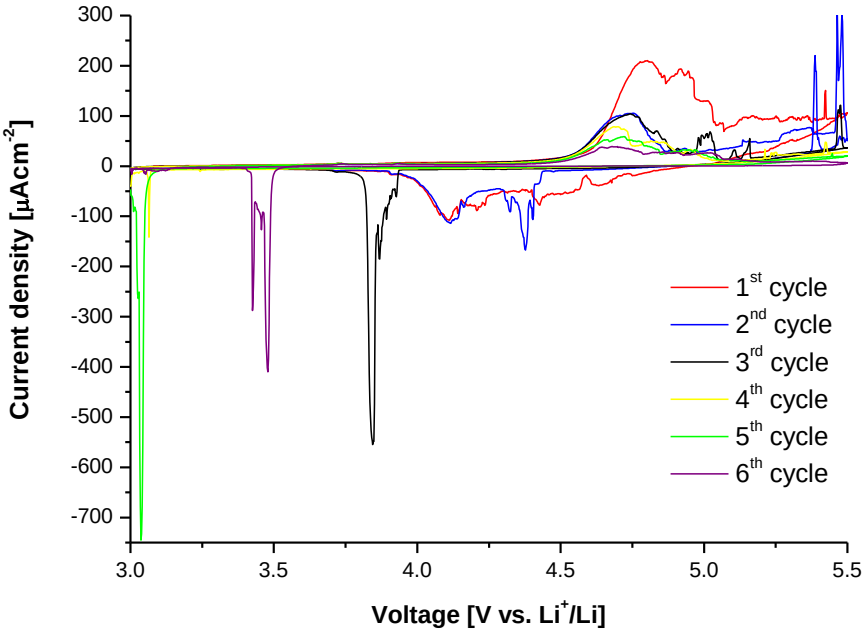

Figure 4.21: Cyclic voltammograms providing all cycles for Graphene AO-2 in combination with 30:70 vol% EC/DMC 1 M $LiPF_6$ (cell AO-2_30/70_3). The curves were obtained using high-voltage CV program.

Upon continuing cycling, the curves related to KS6 and Graphene AO-2 show similar behavior for the two materials. Given in Figure 4.20 and Figure 4.21, respectively. With increasing cycle number, the current density related to the anodic peaks decreases significantly, and the cathodic peaks are shifted towards lower voltages except from the cathodic peak in 4^{th} cycle for KS6 and 6^{th} cycle for Graphene AO-2. Decreasing current density and shift in catholic peak position clearly indicates increased overpotential towards anion intercalation/deintercalation.

4.2.3.2 Operation at different cut-off voltages in 30:70 vol% EC/DMC 1 M $LiPF_6$

For more extensive investigation of the overpotentials related to the high-voltage electrochemical reactions, additional cells were cycled at different cut-off voltages. Figure 4.22 provide the 1^{st} cycle of a cell consisting of Super P Li cycled to a lower cathodic cut-off voltage of 1.5 V vs. Li^+/Li. Figure 4.23 and Figure 4.24 provide the 1^{st} cycle CV curves for cycling to a lower anodic cut-off voltage of 4.7 V vs. Li^+/Li for KS6 and Graphene AO-2, respectively. For comparison, each of the following figures also display the CV curve obtained using *high-voltage CV program*. In addition, Figure 4.25 and Figure 4.26 provide all cycles conducted for KS6 and Graphene AO-2, respectively.

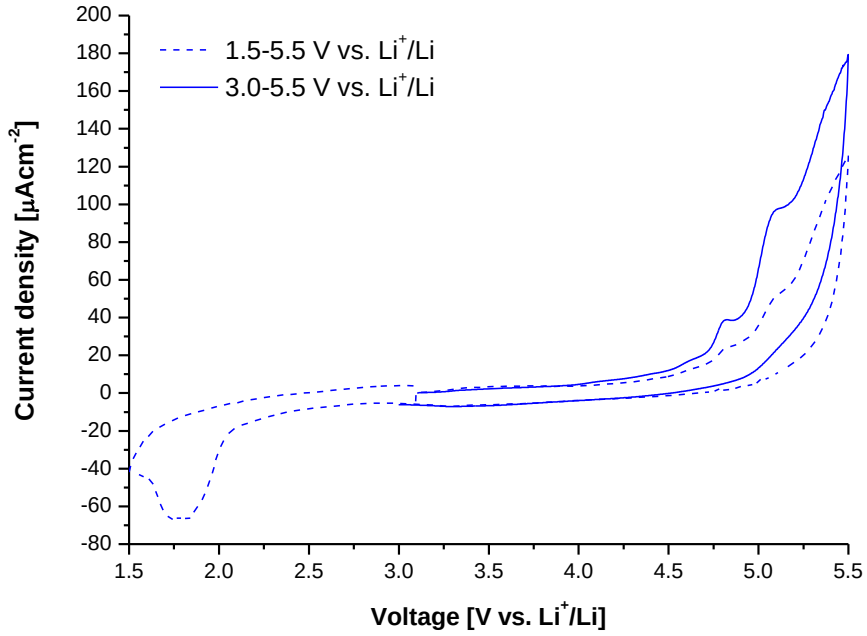

Figure 4.22: Cyclic voltammograms providing the 1st cycle of cells with Super P Li in 30:70 vol% EC/DMC 1 M $LiPF_6$, cycled in different potential regions (cell SP_30/70_1 and SP_30/70_2).

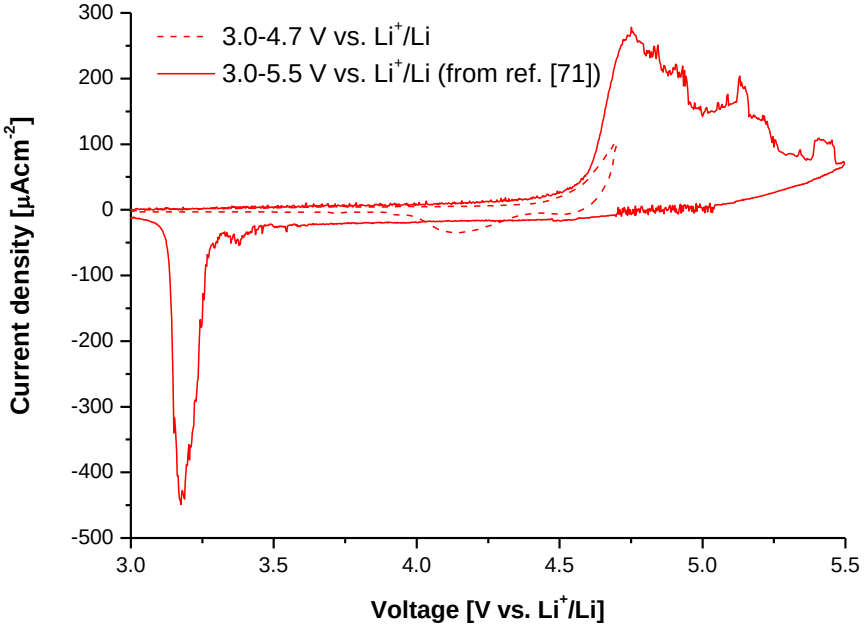

Figure 4.23: Cyclic voltammograms providing the 1st cycle of cells with KS6 in 30:70 vol% EC/DMC 1 M $LiPF_6$ cycled in different potential regions (cell KS6_30/70_CV1 and KS6_30/70_2).

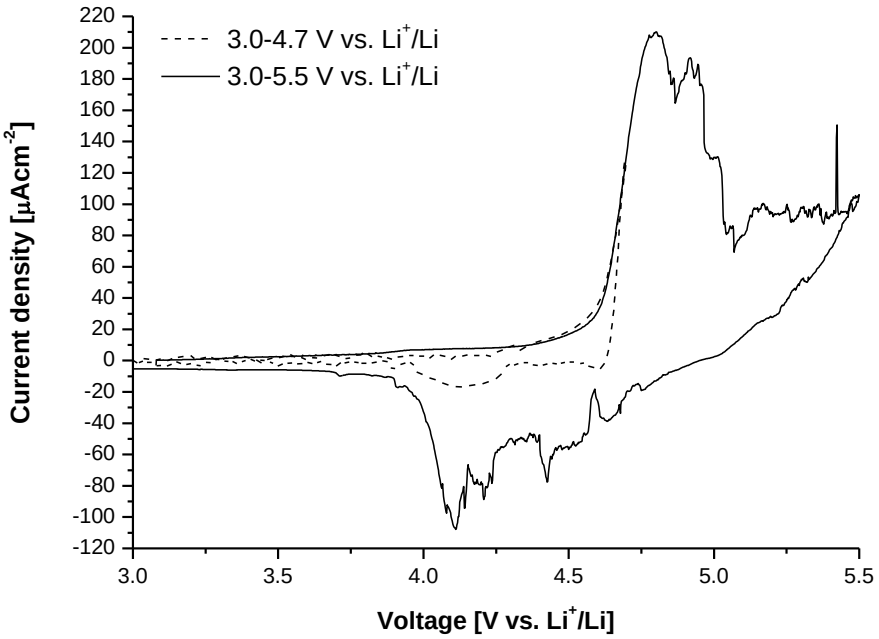

Figure 4.24: Cyclic voltammograms providing the 1st cycle of cells with Graphene AO-2 in 30:70 vol% EC/DMC 1 M $LiPF_6$ cycled in different potential regions (cell AO-2_30/70_3 and AO-2_30/70_2). The dotted line was smoothed using Kalman filter.

Figure 4.22 clearly shows the appearance of a cathodic peak in the system with Super P Li at 1.78 V vs. Li^+/Li. Comparison with the cathodic peak positions for KS6 and Graphene AO-2, all cell cycled to 5.5 V vs. Li^+/Li, reveal a larger overpotential for anion deintercalation in Super P Li. Additional observation for Super P Li is that the anodic peaks are not overlapping, even though the electrodes obtain similar electrode characteristics.

In the system with a KS6 electrode operating at lower anodic cut-off voltage, Figure 4.23, there is a large shift in the cathodic peak position upon the reverse scan, when the anodic cut-off voltage was set to 4.7 V vs. Li^+/Li instead of 5.5 V vs. Li^+/Li. In contrast, no distinct shift in the peak positions was observed for Graphene AO-2 when cycled to 4.7 V vs. Li^+/Li, Figure 4.24.

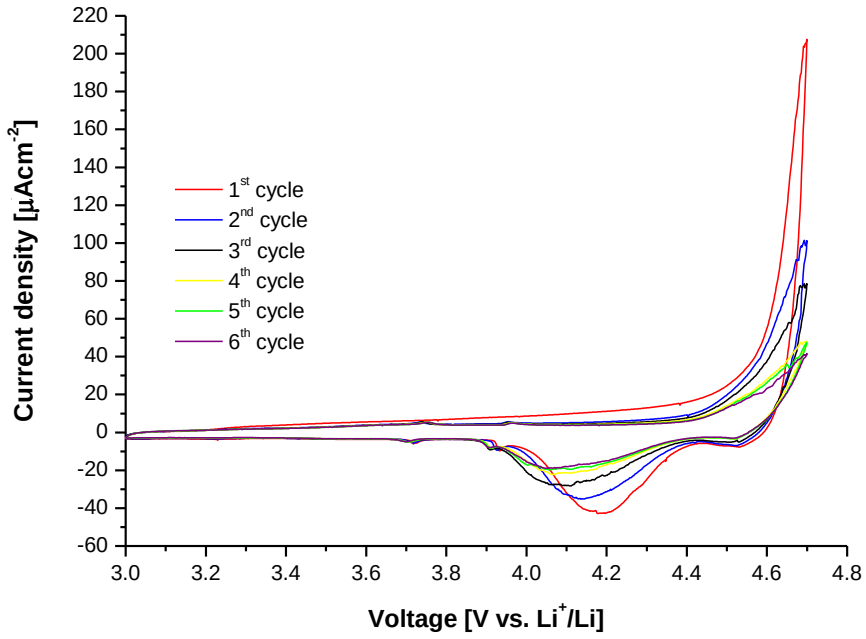

Figure 4.25: Cyclic voltammograms providing all cycles for the with the composition of KS6 in 30:70 vol% EC/DMC 1 M $LiPF_6$ (cell KS6_30/70_2).

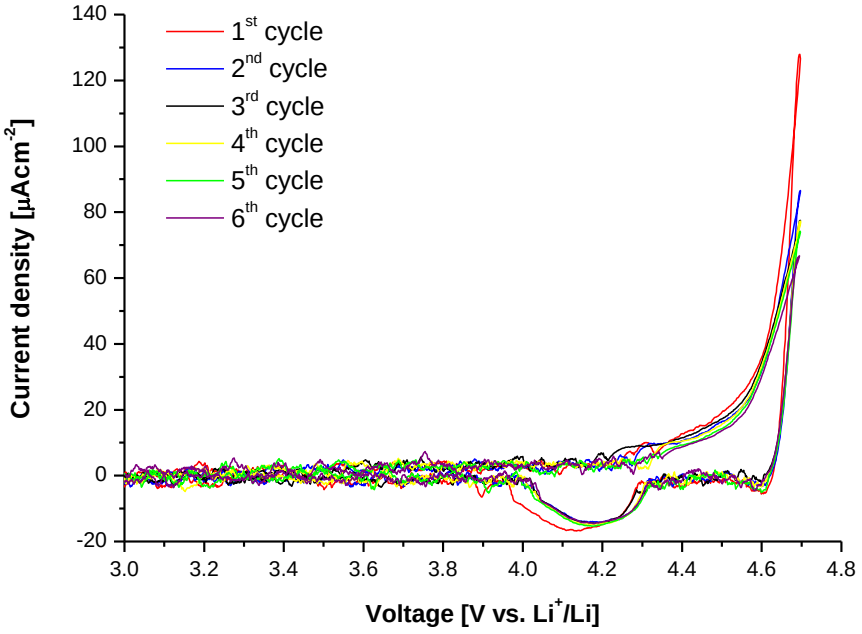

Figure 4.26: Cyclic voltammograms providing all cycles for the cell with the composition of Graphene AO-2 in 30:70 vol% EC/DMC 1 M $LiPF_6$ (cell AO-2_30/70_2). All curves were smoothed using Kalman filter.

For continuous cycling of KS6, provided in Figure 4.25, there is observed a clear decrease in current density related to the anodic peak, and the cathodic peak shifts slightly towards more cathodic voltages when the number of cycles increases. In contrast, there is no shift in the cathodic peak position and the anodic current density does only slightly decrease upon cycling, in the case of Graphene AO-2, see Figure 4.26

4.2.3.3 Operation in various electrolyte compositions

Attempts have been made to study how different electrolyte compositions are affecting the cell system stability, by investigating onset oxidation potential and overpotentials related to the cycling. The experimental matrix gave the overview of the different combinations of carbon material and electrolyte being tested using *high-voltage CV program*. In the following figures, the 1st cycle CV curve will be provided for each carbon material. For comparison, the CV curves presented in Figure 4.18 will also be included. Starting with the curves for KS6 given in Figure 4.27, continuing with Graphene AO-2 given in Figure 4.28, with a close up provided in Figure 4.29, and at the end the curves obtained for Super P Li will be given in Figure 4.30.

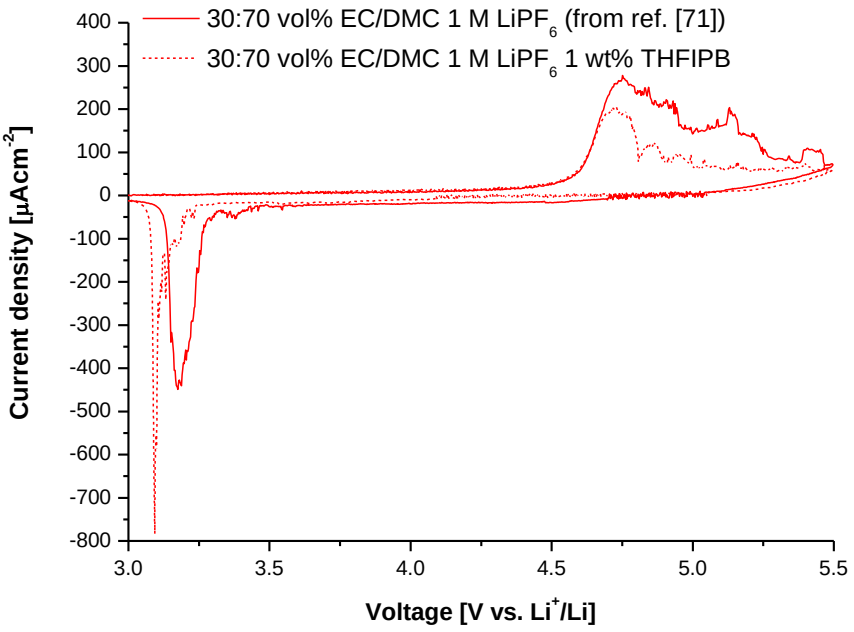

Figure 4.27: Cyclic voltammograms providing the 1st cycle of two cell combinations consisting of KS6 electrodes characterized by electrolyte composition (cell KS6_30/70_CV1 and KS6_AR30/70_ 1). The curves were obtained using high-voltage CV program.

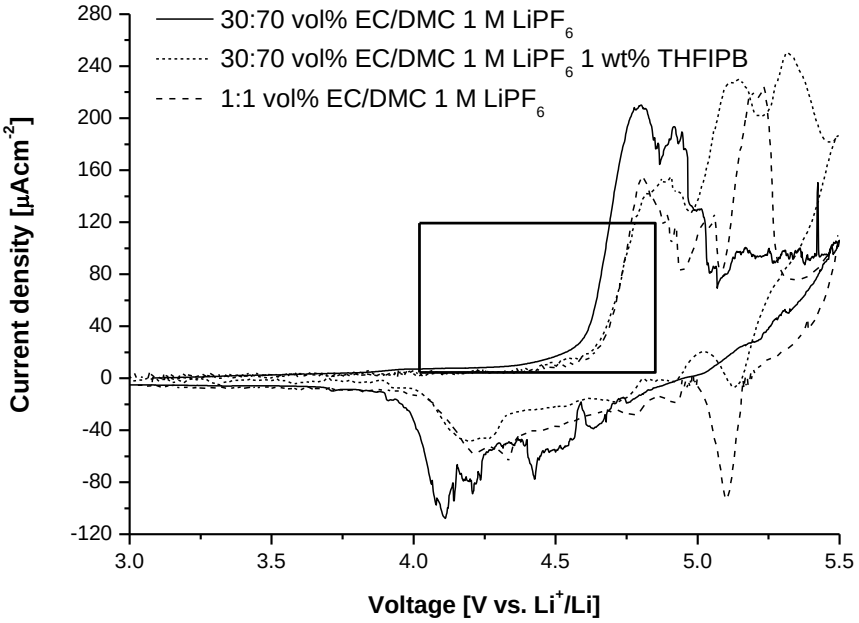

Figure 4.28: Cyclic voltammograms providing the 1st cycle of two cell combinations consisting of Graphene AO-2 electrodes characterized by electrolyte composition (cell AO-2_30/70_3, AO-2_AR30/70_1 and AO-2_1/1_2). The dotted line was smoothed using Kalman filter (cell AO-2_AR30/70_1). The curves were obtained using high-voltage CV program.

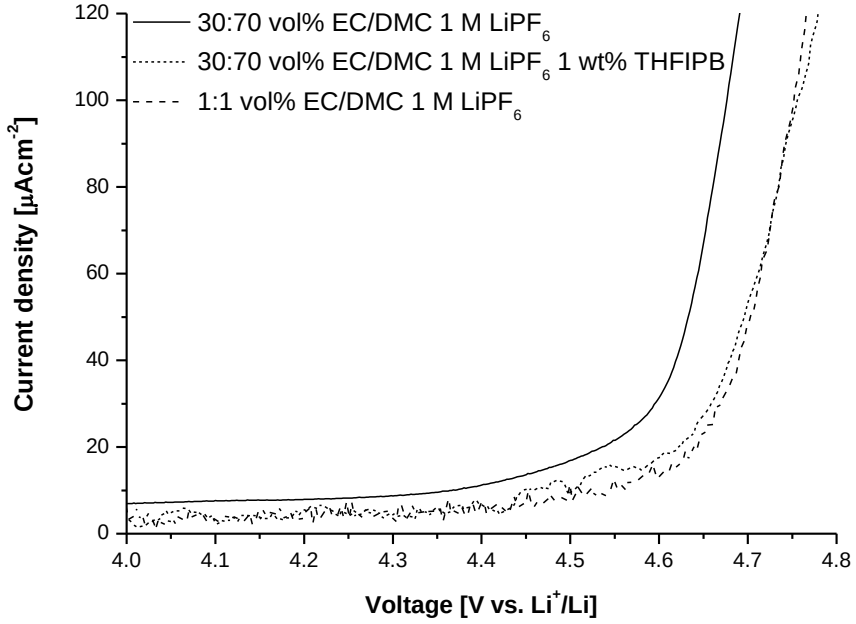

Figure 4.29: Cyclic voltammograms providing the 1st cycle of two cell combinations consisting of Graphene AO-2 electrodes characterized by electrolyte composition (cell AO-2_30/70_3, AO-2_AR30/70_1 and AO-2_1/1_2). The dotted line was smoothed using Kalman filter (cell AO-2_AR30/70_1). The curves were obtained using high-voltage CV program, only the voltage region of 4.0-4.8 V vs. Li+/Li is included.

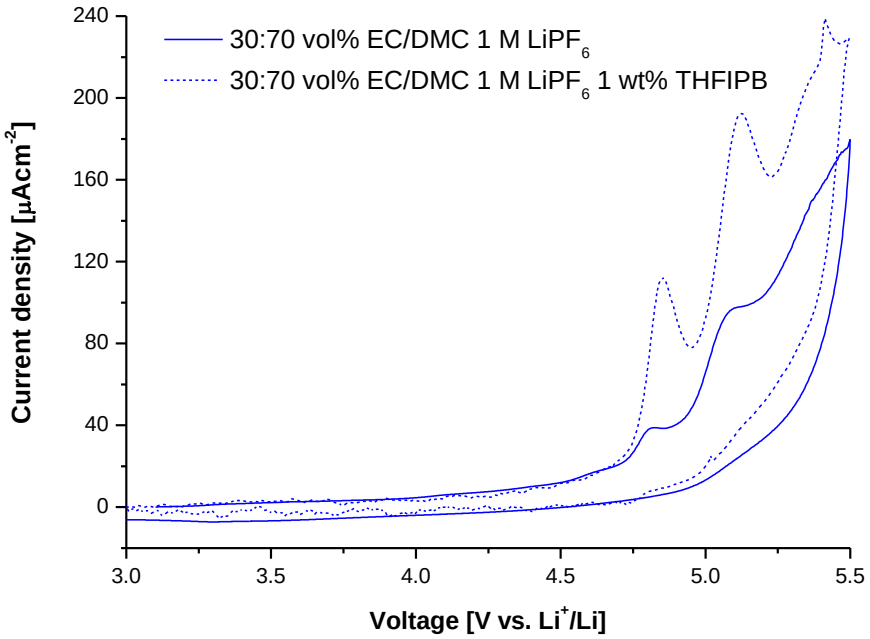

Figure 4.30: Cyclic voltammograms providing the 1st cycle of two cell combinations consisting of Super P Li electrodes characterized by electrolyte composition (cell SP_30/70_1 and SP_AR30/70_1). The curves were obtained using high-voltage CV program.

Addition of THFIPB to a cell system consisting of KS6 did not contribute to any significantly shifts in the anodic peak positions. Same is observed in the case of Super P Li. On the other hand, both addition of AR and utilizing a more viscous electrolyte did result in a slightly shift in the oxidation potentials for the systems consisting Graphene AO-2 electrode in combination with 30:70 vol% EC/DMC 1 M $LiPF_6$ 1 wt% THFIPB and 1:1 vol% EC/DMC 1 M $LiPF_6$, compared to 30:70 vol% EC/DMC 1 M $LiPF_6$, Figure 4.29.

4.2.4 *In situ* X-ray diffraction

In situ XRD measurements were conducted for the two crystalline carbon materials, KS6 and Graphene AO-2. Before presenting the results from these measurements in section ***In situ* X-ray diffraction spectra**, there will be focus on the results from the galvanostatic cycling only.

4.2.4.1 Galvanostatic cycling

Electrode characteristics for tested kapton electrodes along with the electrochemical data obtained for 1st cycle using the *high-voltage current program*, in an electrolyte with the composition of composition of 30:70 vol% EC/DMC 1 M $LiPF_6$ are information summarized in Table 4.8.

Table 4.8: Electrode properties for various types of kapton electrodes and the electrochemical data obtained after galvanostatic cycling.

	Thickness carbon layer [µm]	**Weight active material [mg]**	**1st charge specific capacity [$mAhg^{-1}$]**	**1st discharge specific capacity [$mAhg^{-1}$]**	**C_{eff} [%]**
KS6_30/70 (#1) kapton/carbon	88	11.2	236	23	9.8
KS6_30/70 (#2) kapton/carbon	69	9.0	198	29	14.4
KS6_30/70 kapton/gold	67	11.6	61	28	45.5

From the information provided in the above table there is observed a clear difference between the two types of kapton electrodes, especially with respect to 1st charge specific capacity value. There is reason to believe that additional reactions are taking place at the electrode using carbon coated kapton film as current collector material. Based on these observations only the results from the *in situ* XRD measurements using kapton electrodes coated with gold will be presented in the following section.

4.2.4.2 *In situ* X-ray diffraction spectra

The conducted *in situ* XRD measurements combined galvanostatic cycling and XRD analysis. Figure 4.31 provide the galvanostatic curve for the study of KS6 exposed to an electrolyte with the composition of 30:70 vol% EC/DMC 1 M $LiPF_6$ being cycled galvanostatically with the *high-voltage current program*. The potential curve is presented

as voltage vs. time, displaying only the first four cycles. Included in the figure are several points corresponding to various XRD scans, and these scans along with several others are presented as a 3D plot in Figure 4.32. Only the first two cycles are included in the 3D plot due to short cycling time compared to scanning time. Figure 4.33 provide the potential curve and Figure 4.34 the 3D plot for *in situ* XRD analysis of Graphene AO-2, presented in the same way as the results for KS6.

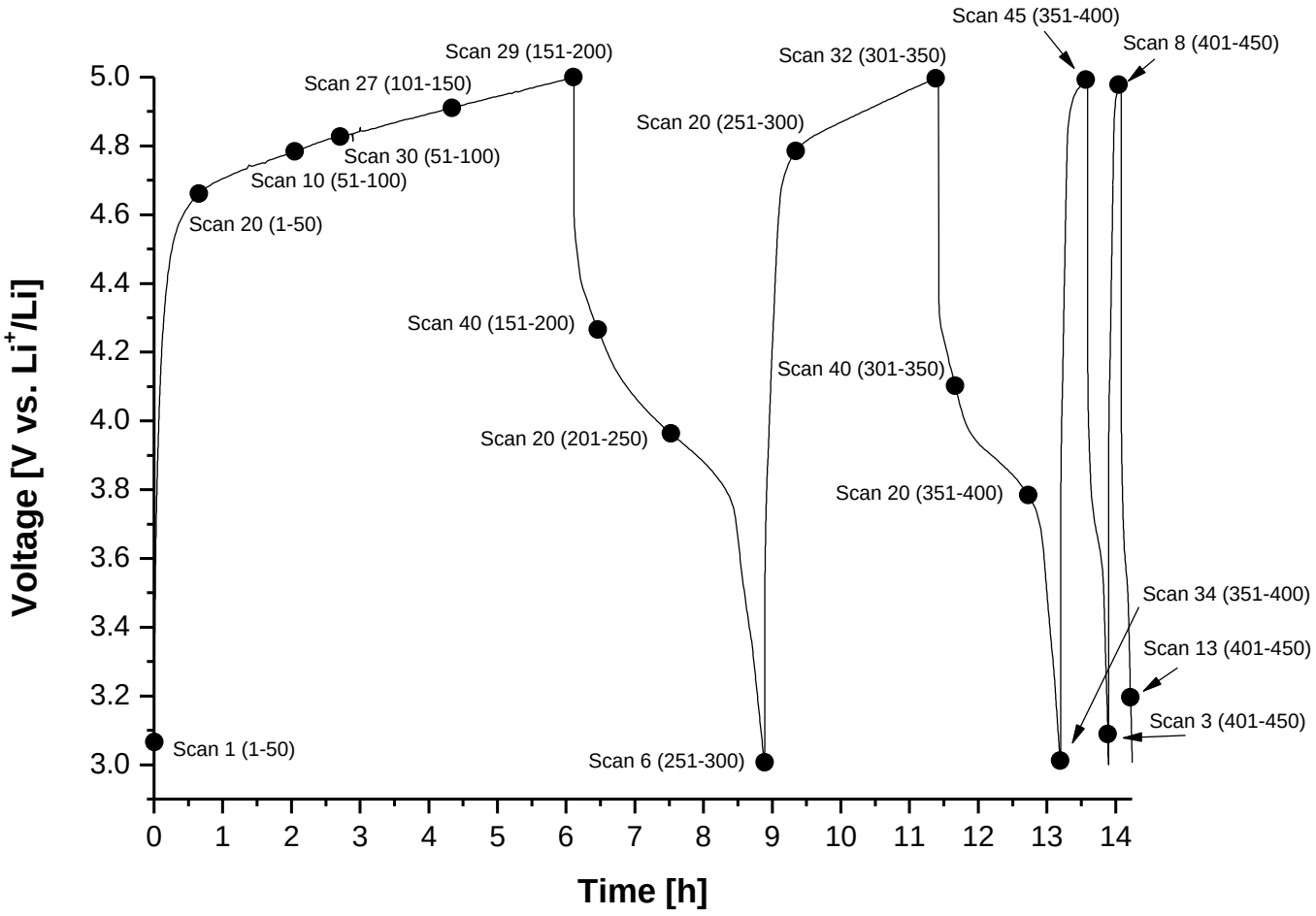

Figure 4.31: Potential vs. time during galvanostatic cycling for KS6 (cell KS6_30/70_XRD3) in 30:70 vol% EC/DMC 1 M $LiPF_6$ using high-voltage current program. Only the first four cycles are provided, included in the curve are points corresponding to various XRD scans.

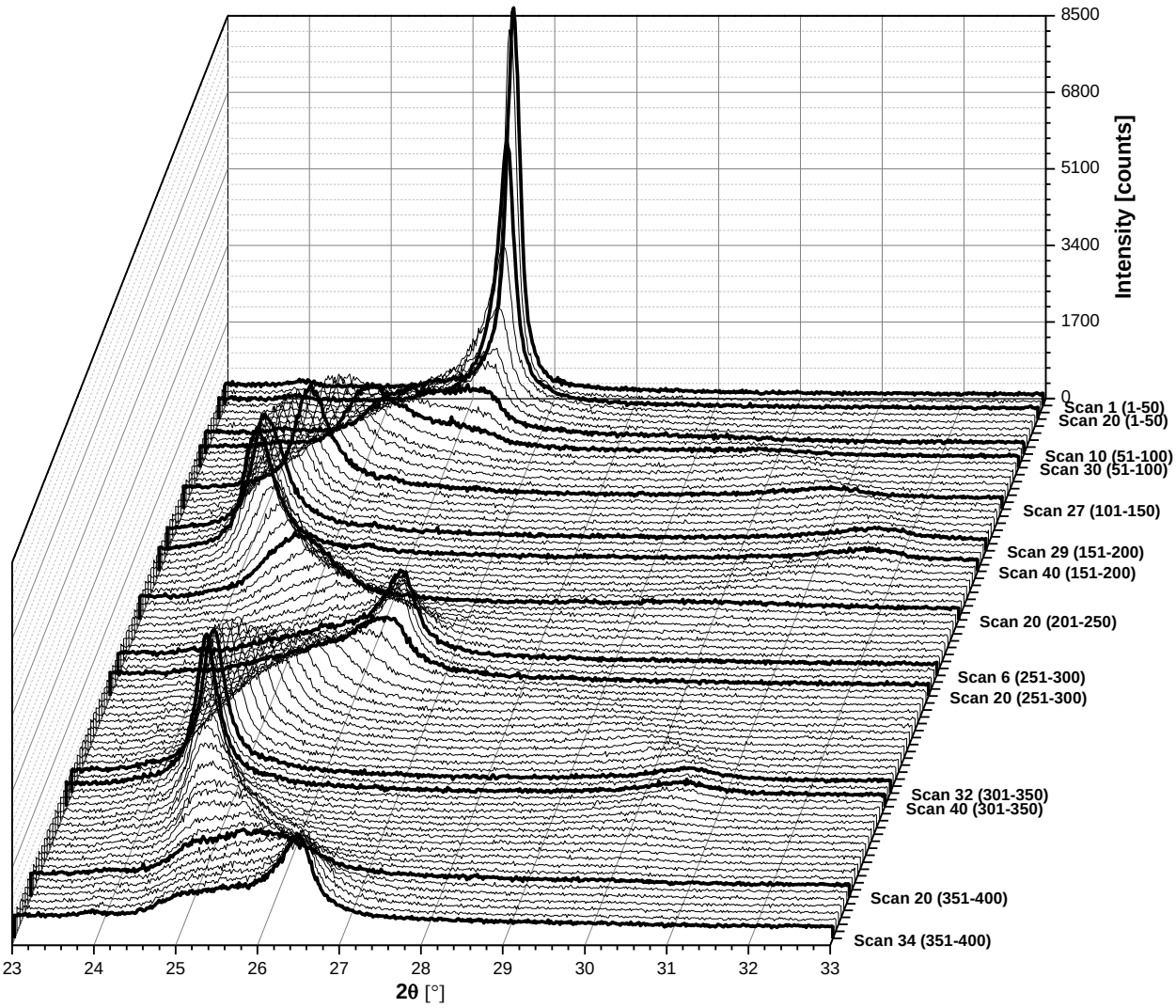

Figure 4.32: 3D plot showing how the XRD spectra is changing upon cycling of KS6 (cell KS6_30/70_XRD3) in 30:70 vol% EC/DMC 1 M $LiPF_6$ using high-voltage current program

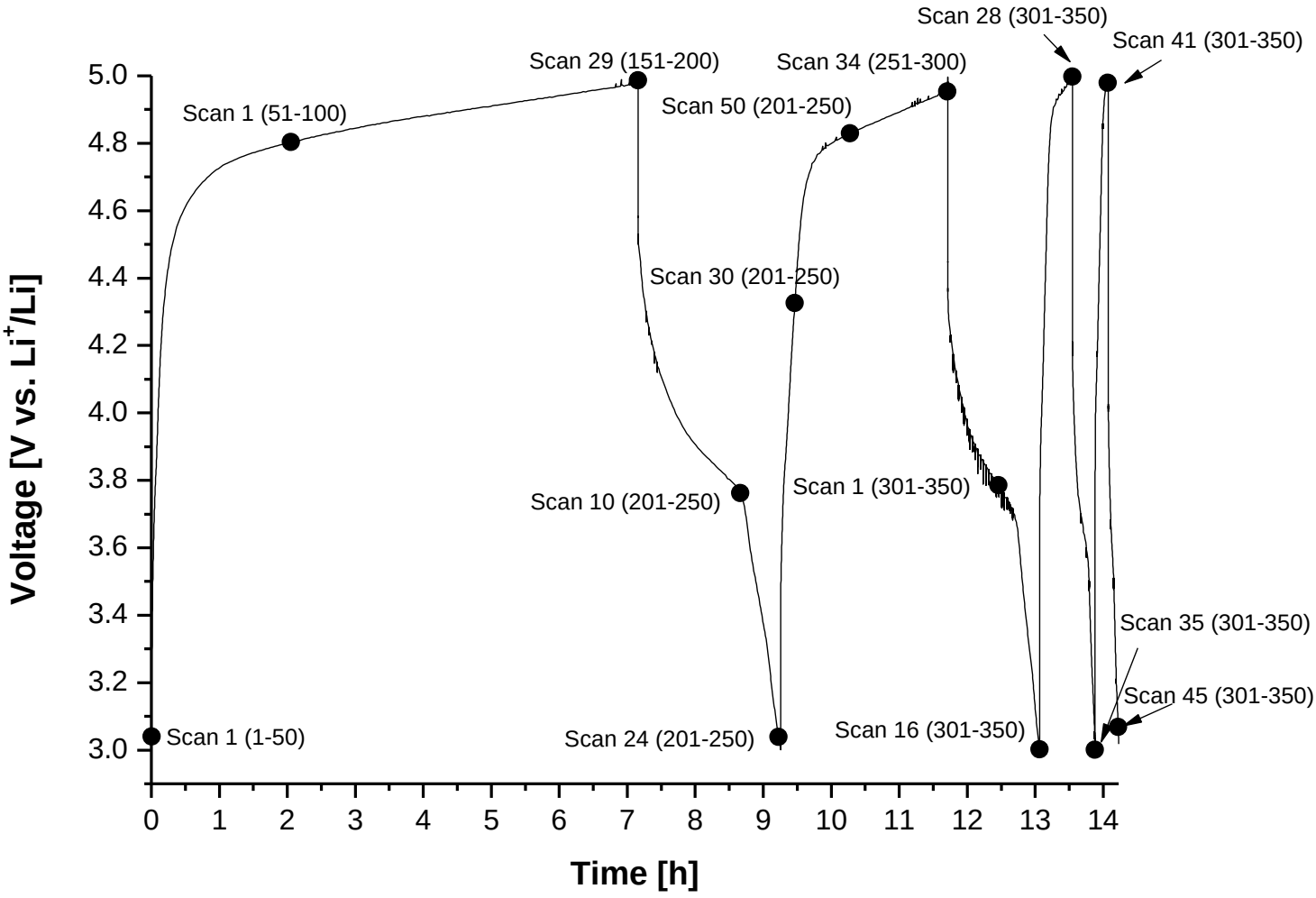

Figure 4.33: Potential vs. time during galvanostatic cycling for Graphene AO-2 (cell AO-2_30/70_XRD1) in 30:70 vol% EC/DMC 1 M $LiPF_6$ using high-voltage current program. Only the first four cycles are provided, included in the curve are points corresponding to various XRD scans.

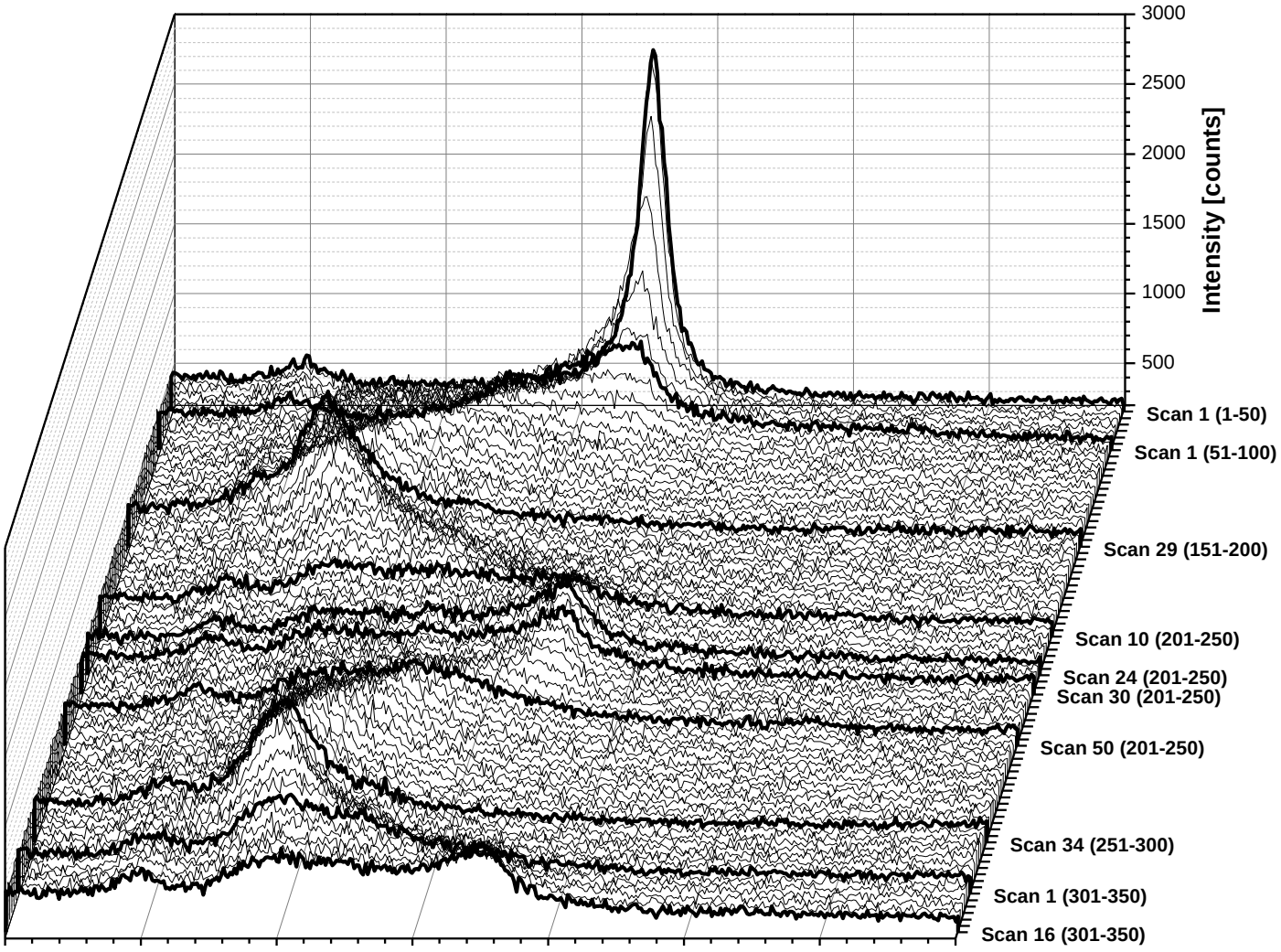

Figure 4.34: 3D plot showing how the XRD spectra is changing upon cycling of Graphene AO-2 (cell AO-2_30/70_XRD1) in 30:70 vol% EC/DMC 1 M $LiPF_6$ using high-voltage current program.

Several observations are made based on the above potential curves and 3D plots. For the cell with KS6:

- Only reduction in peak intensity during scan 1 (1-50) to scan 20 (1-50). The initial peak has vanished by scan 10 (51-100), corresponding to 4.78 V vs. Li^+/Li, and being replaced by a double peak located at lower scattering angles. Meaning that upon charging the peak related to the interplanar distance starts to shift towards lower scattering angles.
- At scan 30 (51-100) a diffraction peak which corresponds to staged phase appears in the spectra at scattering angle equal 30°, corresponding to a voltage of 4.83 V vs. Li^+/Li. Upon further charging, this peak was shifted towards higher scattering angles.
- Scan 27 (101-150) which corresponds to a voltage of 4.91 V vs. Li^+/Li indicate the formation of a stage 4 intercalated carbon structure, meaning that after every fourth carbon layer there is one layer consisting of anions.
- When the cell reached fully charged state, at scan 29 (151-200), the peaks obtained the opposite behavior. The peak related to the (002) planes shifted towards its initial position, while the peak which corresponds to staged phase being shifted towards lower scattering angles. At scan 20 (201-250), which equals a voltage of 3.96 V vs. Li^+/Li, this additional diffraction peak had almost vanished.
- Comparison of the initial peak and the peak at fully discharge in the 4^{th} cycle, given in Figure 4.35, corresponding to scan 13 (401-450), reveal a change in peak shape. The peak at fully discharge has a much lower intensity compared to the initial peak, in addition to a shoulder appearing at lower scattering angles.

Comparing Figure 4.32 with Figure 4.34, it is easily observed that the signal-to-noise ratio is less in the spectra recorded for Graphene AO-2, due to the different defined scanning program (same scan rate as KS6, but different scanning range). This make it more challenging to interpret the data, and impossible to observe any appearance of a diffraction peak which corresponds to stage phase in the spectra. However, some information can be determined from the data:

- There is a shift in peak position of the peak related to the (002) plane upon charging, and this peak return to the scattering angles corresponding to initial position at fully discharge. However, as in the case of KS6, the intensity is thus much smaller and the peak shape differ from the initial one.

- Studying the shape of the peak at scan 16 (301-350), which indicates fully discharge in the fourth cycle, reveal an even larger change in peak shape compared to KS6. The peak shape is given in Figure 4.36.

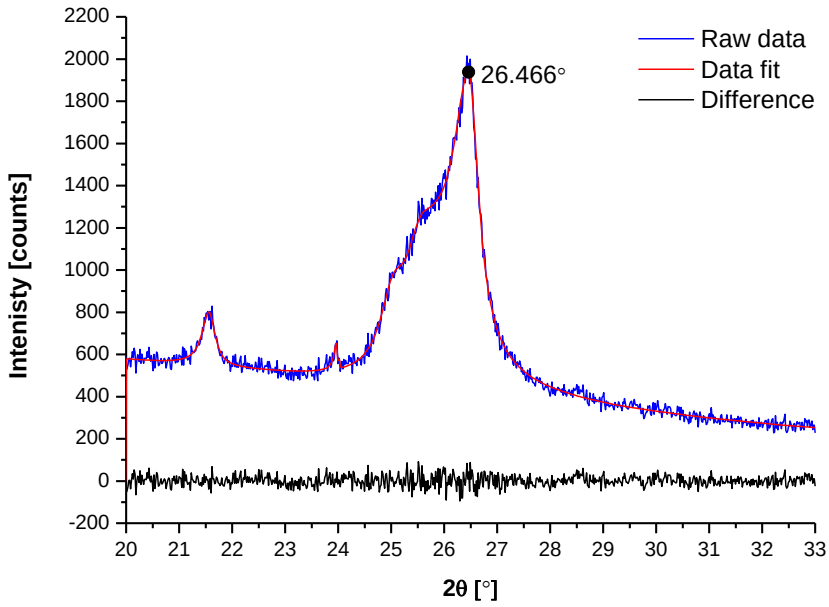

Figure 4.35: XRD spectra for scan 13 (401-450) obtained for KS6 (blue), displayed together with the fit curve (red) and the difference (black). Peak position and value are indicated in the curve.

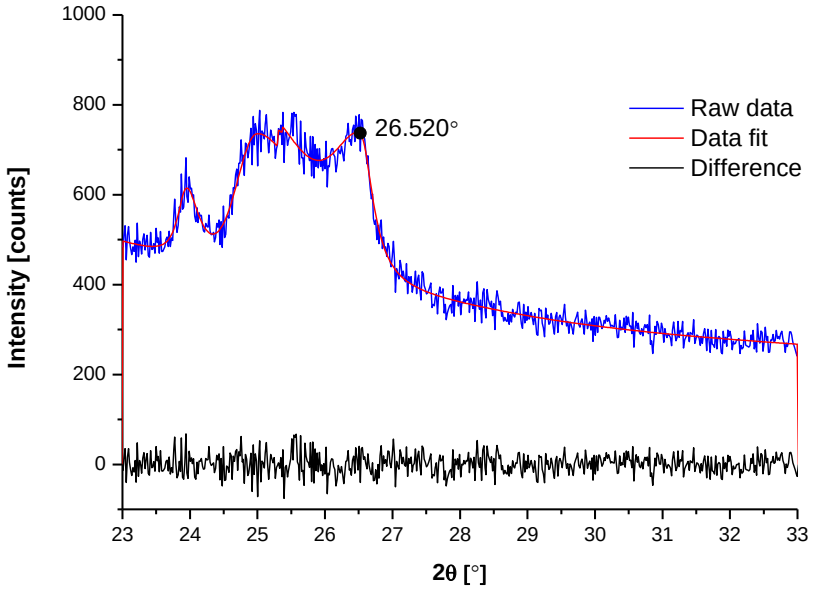

Figure 4.36: XRD spectra for scan 45 (401-450) obtained for Graphene AO-2 (blue), displayed together with the fit curve (red) and the difference (black). Peak position and value are indicated in the curve.

The observed shift in diffraction peak corresponding to the (002) planes, gives a clear indication of an increase in interlayer distance, for both types of carbon materials. Based on the peak position, measured using TOPAS software, the d_{002} value was calculated for initial, 1st charge for each carbon material adopting Braggs law (2.6). The calculated values are provided in Table 4.9. This was done in order to investigate the expansion in the carbon structure due to intercalation of anions.

Table 4.9: Measured $2\theta_{002}$ values, calculated d_{002} values[9], and the relative increase in d_{002} upon galvanostatic cycling.

		KS6	**Graphene AO-2**
Initial	$2\theta_{002}$ [°]	26.521	26.534
	d_{002} [Å]	3.358	3.357
1st charge	$2\theta_{002}$ [°]	24.172	24.439
	d_{002} [Å]	3.679	3.639
Relative increase in d_{002} [%] from initial to 1st charge		9.55	8.43

Observation of an additional peak in the 3D plot for KS6, indicate staged anion intercalation, and the stage index was calculated using equation (2.8), for scan 29 (151-200), corresponding to fully charge in 1st cycle. The calculated value is provided in Table 4.10.

Table 4.10: Calculated stage index for 1st fully charge for a cell consisting of KS6 in an electrolyte consisting of 30:70 vol% EC/DMC 1 M $LiPF_6$ cycled using high-voltage current program.

		KS6
1st charge	$2\theta_{00n}$ [°]	24.172
	$2\theta_{00(n+1)}$ [°]	31.689
Stage index (n)		3.29

4.2.4.3 Scanning electron microscopy

The electrodes being cycled galvanostatically and studied with XRD, were also studied using SEM. With focus on investigating any structural changes due to the anion

[9] Parameters used in the calculations: λ=1.54060 Å and n=1.

intercalation these electrodes were washed prior analysis to remove any electrolyte decomposition products on the surface. The micrographs are provided in Figure 4.37, in addition to images of pristine electrodes for comparison.

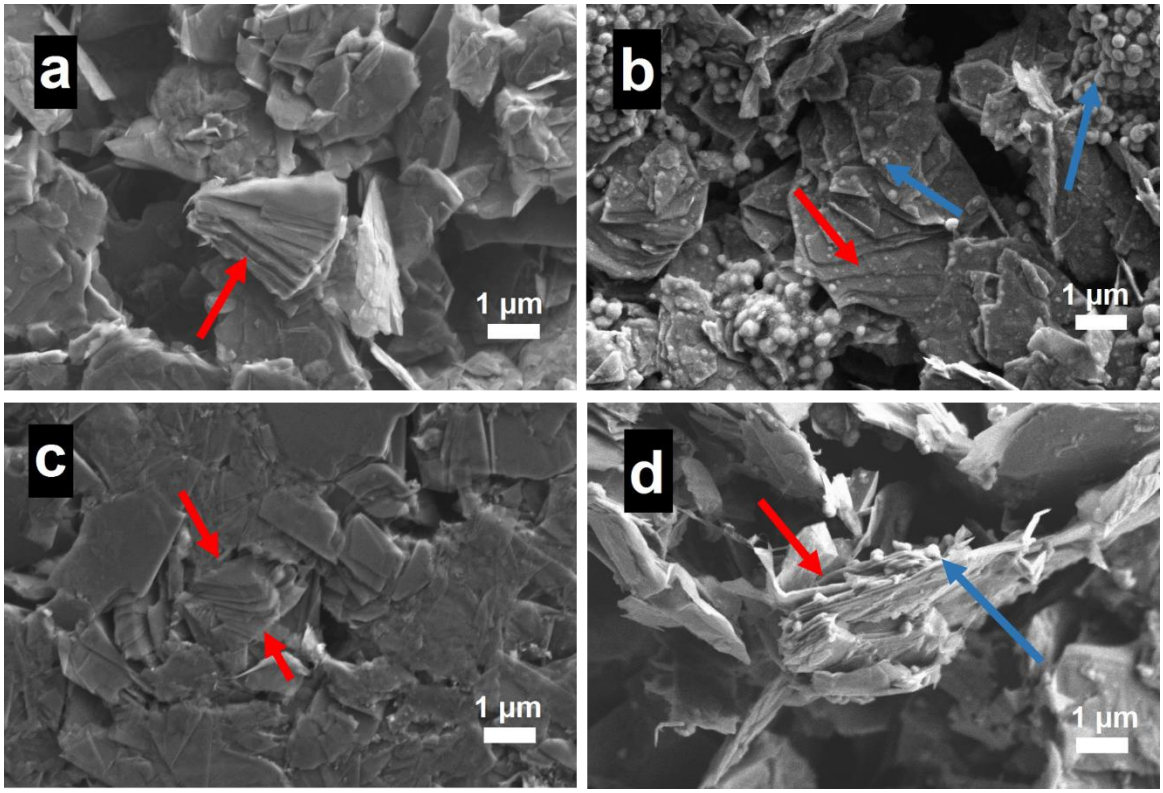

*Figure 4.37: Scanning electron microscopy images: **a** pristine electrode containing 90 wt% KS6 and 10 wt% PVDF, **b** cycled electrode containing 90 wt% KS6 and 10 wt% PVDF (cell KS6_30/70_XRD3), **c** pristine electrode containing 90 wt% Graphene AO-2 and 10 wt% PVDF, and **d** cycled electrode containing 90 wt% Graphene AO-2 and 10 wt% PVDF (cell AO-2_30/70_XRD1). All micrographs were obtained using secondary electron detector, working distance equal 6.1-6.5 mm, and an accelerating voltage of 3.0 kV.*

After galvanostatic cycling, the same macroscopic layered structure was observed as in the pristine electrode, indicated by red arrows. In addition, for both cycled electrodes, the appearance of spherical white spots on both basal planes and edge planes were observed, indicated by blue arrows in the image.

5 Discussion

It is clear from all presented results that the studied carbon materials become electrochemical active in $LiPF_6$ based organic carbonate electrolytes at operation voltage above 4.7 V vs. Li^+/Li. In the following discussion, anion intercalation and electrolyte oxidation are the two high-voltage electrochemical reactions of interest. Upon charging, both reactions take place at the electrode, while only anion deintercalation is occurring in the following discharge step.

The first part of the chapter will provide the basis for understanding of how the various materials behavior is related to powder properties and electrode characteristics, and will be used in the further discussions where the three materials behavior will be compared. Furthermore, in order to make the comparison easier the chapter will then be divided into sections based on the electrolyte composition. First, cycling and testing results for carbon electrodes exposed to electrolyte 30:70 vol% EC/DMC 1 M $LiPF_6$. Thereafter, *in situ* XRD and SEM will be evaluated in order to improve the understanding of the findings from the electrochemical cycling. Second, discussion of the behavior of the three carbon materials tested in combination with additional electrolyte compositions; 1:1 vol% EC/DMC 1 M $LiPF_6$, 30:70 vol% EC/DMC 1 M $LiPF_6$ 1 wt% THFIPB, and 1:1 vol% EC/DMC 1M $LiPF_6$ 1 wt% THFIPB. Additional electrolytes were tested for comparison of the the carbon electrode and electrolyte stability, by changing electrolyte viscosity and adding anion receptor.

5.1 Carbon characterization

In addition to the results from the characterization of carbon powders presented in section 4.1, additional information are given in Table 5.1. The values for Brunauer-Emmett-Teller (BET) specific surface area were measured as a part of a previous study by the author [71]. Analysis of carbon materials using Raman spectroscopy displays two characteristic bands, D and G bands, and their intensity allows an estimation of the crystallite size in the surface layer of any carbon sample [72]. Super P Li and Graphene AO-2 were studied using Raman spectroscopy in the work of Sætnan [73]. The measured D- and G-band intensity and the calculated L_a values are provided in Table 5.1.

Table 5.1: Measured BET specific surface area, L_a values calculated based on values of intensity of D and G bands, measured using Raman spectroscopy, and L_a value for KS6 from literature.

	BET specific surface area [71] [m^2g^{-1}]	**I_D [-]**	**I_G [-]**	**L_a [Å]**
KS6	20	-	-	475 (XRD) [62], 210 (Raman) [62]
Graphene AO-2	19-25	107	341.5	309 [73]
Super P Li	60	192.7	219.4	110 [73]

All information obtained for the three carbon materials clearly show that KS6 and Graphene AO-2 are highly crystalline powders, having close to ideal graphitic structure. This is shown by the interlayer spacing, and large values of L_c and L_a, given in Table 4.1 and Table 5.1. Differences were observed in particle shape and size. On the other hand, Super P Li display less crystallinity by obtaining a relatively large interlayer spacing, small value for L_c, and a particle size in nano-range. Consistent with the presented parameter values characterizing carbon black, see chapter 2.2.5. Table 5.1 displays a relatively large L_a value for Super P Li. Considering the crystallite orientation in a carbon black particle, Figure 2.9, large L_a value indicate a large fraction of basal planes in the particle surface. Since lithium ions intercalates only through defect sites in basal planes, as described in section 2.1.2, there is reason to believe that anions do intercalate the Super P Li electrodes, thus in a less extent compared to graphite.

There were no observable differences in the full scan XRD spectra for the KS6 and Graphene AO-2 powders at low scattering angles, Figure 4.2, thus it seems that the Graphene AO-2 powder, which producers claim to be graphene multilayer powder, mainly consists of graphite-like particles. Since the powder was observed to easily disperse in the solvent during electrode preparation, the powder was expected to contain graphene oxide. However, the assumption of fully graphitic powder is based on the fact that graphene oxide powders would result in a diffraction peak at scattering angles of ~11°, measured in previous research in the field of graphene materials [74, 75]. In order to get more information about the Graphene AO-2 powder, and how the crystal structure differs from KS6 further investigations need to be conducted.

The measured values of BET surface area of pure carbon powders, given in Table 5.1, are in accordance with the technical data in the case of KS6 and Super P Li. In contrast, for Graphene AO-2, the producer state 100 m^2g^{-1}, while the measured value is significantly

lower (19-25 m^2g^{-1}). There is no clear reason why the values differs to such extent, one possible explanation is particle agglomeration during analysis, resulting in a lower measured specific surface area. In following discussions, it will be assumed that Graphene AO-2 has a BET specific surface area of 100 m^2g^{-1}.

Notably, the measured BET values were obtained by analyzing the carbon materials in powder state, while the carbon material behavior has been investigated in the form of casted electrodes. There is reason to believe that the surface area of pure carbon powders differs to some degree when being tape casted into electrodes. This was confirmed by estimating the active electrode area of KS6 and Super P Li electrode, given in Table 4.3. Both electrodes display a surface area of approximately 66% of the BET area of the powders, given in Table 5.1. A reasonable value when taking into consideration the particle arrangement in the electrode, resulting in surface area losses due to e.g. contact points between particles and the addition of binder. In the following discussion using the differences in BET surface areas for the three carbon materials to explain the observed electrochemical behavior, seem to be a good assumption.

5.2 30:70 vol% EC/DMC 1 M $LiPF_6$

Carbon material behavior and stability have been most extensively studied in combination with electrolyte containing 30:70 vol% EC/DMC 1 M $LiPF_6$.

5.2.1 Potential curves

For all three carbon materials, no clear plateaus were observed in the potential curves upon cycling at high voltages, Figure 4.5, Figure 4.6, and Figure 4.7. Based on the observations it is impossible to state whether anions are intercalating forming staged phases, which is easily observable in the case of Li^+-ions intercalating graphite, see Figure 2.3, or like Seel and Dahn [11] observed and verified in their study of anion intercalation into graphite.

5.2.2 Specific capacity diagrams

The measured discharge capacity values are larger than zero, indicating some degree of reversibility in all three carbon systems and clearly state that anions are intercalating/deintercalating the carbon structures upon cycling at high voltages.

In their study of carbon blacks, Zheng et al. [32] obtained results showing small but stable capacity values, due to limited anion intercalation. The capacity diagram for Super P Li, Figure 4.10, displays values of the same order. This behavior is reflected by the powder characteristics, discussed in section 5.1; the large fraction of basal planes at the particle surface limits the anion intercalation, hence result in low discharge capacity values. However, the anion intercalation does not seems to be affected upon continuous cycling, as shown by the equal height of the blue bars presented in Figure 4.10. This stable behavior might be explained by the formation of a film on the electrode surface being easily penetrable for the anions.

On the other hand, relatively large initial discharge capacities were observed for the crystalline materials KS6 and Graphene AO-2, as presented in Figure 4.8 and Figure 4.9, respectively. The measured initial discharge values for KS6 and Graphene AO-2, equaled 30.7±4.2 $mAhg^{-1}$ and 27.9±1.1 $mAhg^{-1}$, respectively. These values are in good agreement with the 1st discharge capacity reported in the work of Ishihara et al. [43], for carbon materials obtaining similar (002) distance as calculated for KS6 and Graphene AO-2, Table 4.1. These values are in the order of six times larger than for Super P Li, which is related to the differences in crystallite orientation for the three carbons, being more accessible for anions in the case of graphitic carbon, section 2.2.5. Previous studies also report higher capacity values obtained in the case of graphitic carbons. Seel and Dahn [11] obtained a capacity value of 140 $mAhg^{-1}$ related to anion intercalation in graphite, when they used an oxidation stable electrolyte and the cell was cycled to 5.5 V vs. Li^+/Li. However, there is reason to believe that even higher initial discharge capacity values would be obtained for Graphene AO-2 and KS6 using a higher anodic cut-off voltage, e.g. 5.5 V vs. Li^+/Li, and observation made in the work of Ishihara and coworkers [43].

While the initial discharge capacity values measured for KS6 and Graphene AO-2 were in the same order, the two cell systems displayed large differences in initial charge capacity values. For Graphene AO-2, a value of 167.6±14.4 $mAhg^{-1}$ was measured, which is higher than the reported capacity related to anion intercalation, corresponding to 140 $mAhg^{-1}$ [11].

This thus clearly indicates electrolyte oxidation at the electrode surface upon charging. A much lower initial charge capacity was reported for KS6, 52.2±10.3, while the estimated C_{eff} also predicts electrolyte decomposition in this system by obtaining a value less than 100%, Table 4.4. Compared to the C_{eff} value for Graphene AO-2, this clearly shows that the system containing KS6 electrode displays a more reversible behavior. The observed difference in C_{eff} indicates more electrolyte oxidation on Graphene AO-2 compared to KS6 during charging. Super P Li shows an initial charge capacity of 71.8±27.9 $mAhg^{-1}$, which is in agreement with the relative BET surface area. These observations correlate well with the results from the work of Zheng and coworkers [32], which reported an initial charge capacity increase with increasing surface area, since increased surface area provide more active sites for the electrolyte oxidation reaction.

However, it has to be pointed out the y-errors for the initial cycle of Super P Li, shown in Figure 4.10, indicate a quite large uncertainty in the measured charge capacity. This is due to one parallel which displayed a very low 1^{st} charge capacity. All three Super P Li electrodes, in each parallel, obtained similar electrode properties, as given in Table 4.2. One possible explanation for this different behavior is related to the carbon particle arrangement. It is highly possible that there are structural differences within one electrode cast, and parts of the electrode might be containing more agglomerated particles. This hinders the electrolyte to get in direct contact with all parts of the electrode. A second possible explanation is that some parts of the electrode layer might have lost contact with the current collector, due to the very brittle properties of the Super P Li casts which made them very difficult to handle in the cell assembly.

5.2.3 Cyclic voltammograms

Upon cycling to 4.78 V vs. Li^+/Li, Super P Li shows the most stable behavior, while KS6 and Graphene AO-2 become active at lower voltages, 4.55 V vs. Li^+/Li and 4.61 V vs. Li^+/Li, respectively. It has to be stressed that there are some uncertainties is these values, pointed out in section 4.2.3.1. However, the estimated values do correlate reasonably well with results from other studies. For graphite with particles in the size of 6 µm and an interlayer distance equal 3.35 Å, exposed to an electrolyte composed of 1:2 wt% EC/DMC 1 M $LiPF_6$, Ishihara et al. [43] reported an onset oxidation potential of approximately 4.5

V vs. Li^+/Li. While in the case of Super P Li, several studies on carbon blacks show values for onset oxidation potential in the order of 4.6-4.8 V vs. Li^+/Li [32, 50].

The variations between the behaviors of the three carbon materials is even larger when taking into consideration the cathodic direction, seen in Figure 4.18. The most striking difference is the absence of a cathodic peak for Super P Li in the defined voltage region. Including the results from cycling to lower cathodic cut-off voltage, Figure 4.22, a peak appears in the initial CV curve. Indicating a relatively large overpotential towards anion deintercalation in Super P Li when being operated to a potential of 5.5 V vs. Li^+/Li. The observed overpotential is larger than what was observed in the study of Syzedk and coworkers [9] in their investigation of carbon black, Super P exposed to 30:70 vol% EC/DMC 1 M $LiPF_6$, which might be due to the lower anodic cut-off voltage set in their testing program (4.9 V vs. Li^+/Li). However, the peak appearance are in accordance with the observed discharge capacities, both results showing that anions are deintercalating from the carbon black structure and not all being left in the structure upon discharging.

Worth mentioning, there is observed a clear difference in current density for the two curves provided in Figure 4.23. Same explanation as mentioned previous in section 5.2.2 , used to describe differences in capacity, might also explain the observable differences in the CV curves.

Like Super P Li, both KS6 and Graphene AO-2 display a relatively large overpotential towards anion deintercalation, taking into consideration several cycles up to a voltage of 5.5 V vs. Li^+/Li, as observed in Figure 4.20 and Figure 4.21, respectively. However, the differences in overpotential towards anion deintercalation differs in the 1st cycle, Figure 4.23 for KS6 and Figure 4.24 for Graphene AO-2. It seems like the relatively low BET surface area for KS6 is related to the large overpotential for anion deintercalation, which might be attributed to: i) larger fraction of the electrode surface is covered by decomposition products, or ii) a thicker film is formed on the surface. However, when taken into consideration the continuous cycling, the two materials display very similar behavior; in general an increased overpotential for anion deintercalation and decreased anodic current, with increasing cycle number, due to continuously electrolyte oxidation; film formation preventing anions from intercalating/deintercalating. However there are some cathodic which deviates from the expected behavior, the peak is positioned at higher voltages than in the previous cycle. Because of the limited voltage range there are some

cathodic peaks positioned close to the lower cut-off voltage, there is reason to believe that anions remain in the structure and contribute to a higher concentration of anions in the following cycle. Higher concentration of anions might probably lead to a lower overvoltage for deintercalation and thus the cathodic peak is shifted towards higher voltages, corresponding to 4^{th} cycle in Figure 4.20, and 6^{th} cycle in Figure 4.21.

Another observation worth to be mentioned, is the very noisy CV curves in the case of Graphene AO-2, observed in Figure 4.20. Compared with the results of Märkle et al. [7], they claimed that a noisy current signal was attributed to electrical contact losses between carbon/carbon particles or carbon particles/current collector, due to electrode exfoliaton. Thus affecting the electrode stability negatively and not being favorable in terms of high-voltage operation.

Cycling KS6 and Graphene AO-2 at lower cut-off voltages, set to 4.7 V vs. Li^+/Li display in general a much lower overpotential towards anion deintercalation for both systems, Figure 4.23 and Figure 4.24, respectively. The much lower overpotential observed is related to the less extent of electrolyte oxidation at 4.7 V vs. Li^+/Li compared to operation at 5.5 V vs. Li^+/Li (clearly observable for the initial cycle in the case of KS6, while Graphene AO- 2 show a less overpotential in 2^{nd} cycle, see Figure 4.26).

Based on the above observations, the onset potential, just below 4.7 V vs. Li^+/Li might then mainly be related to anion intercalation. This is in accordance with previous investigation of anion intercalation mechanism, reporting an intercalation potential in the region of 4.5-4.7 V vs. Li^+/Li [11, 38, 43].

Upon continuous cycling of both types of carbon electrodes, the faster decrease in anodic current density in combination with a small shift in cathodic peak position for KS6 compared to Graphene AO-2, provided in Figure 4.25 and Figure 4.26, respectively, display a much larger degree of reversibility, and thus stability of the system containing Graphene AO-2.

5.2.4 *In situ* X-ray diffraction

The conducted *in situ* XRD measurements show similar behavior of KS6 and Graphene AO-2. Upon charging to 4.7-4.8 V vs. Li^+/Li, both materials have started to intercalate anions. Explaining the observable discharge capacities presented in Figure 4.8 and Figure

4.9, respectively. The verification of anion intercalation is based on the observed shift in peak position towards lower scattering angles for the diffraction peak corresponding to (002) planes, which is in accordance with observations in the work of Seel and Dahn [11]. When fully charged, corresponding to a specific capacity of 140 $mAhg^{-1}$, they measured a relative increase in d_{002} from initial state to a value of 16.7 %, introducing more stresses on the carbon structure compared to a fully lithiated graphite, reasonable due to the size differences between the two types of ions. Table 4.9 shows that KS6 and Graphene AO-2 were not exposed to stresses in the same extent as in the initial cycle, Graphene AO-2 less than KS6.

However, at fully discharge the initial peak did not reappear with the same intensity and width for any of the two materials. After four completed cycles, the peak shape differed even more. Seel and Dahn [11] observed a peak broadening during the initial cycle which they claimed to be due to anions being trapped in the carbon structure. The results with KS6, given in Figure 4.35, and Graphene AO-2, given in Figure 4.36, display discharge peaks consisting of multiple peaks, with different positions and width. Indicating both uniform and non-uniform strains in the carbon structures as described in theory and illustrated in Figure 2.14. These strains might very likely be due to entrapping of anions in the carbon structure, indicating that anions do not intercalate fully reversible in either KS6 or Graphene AO-2. Regarding stability related to anion intercalation, the discharge peak for Graphene AO-2 show larger structural changes compared to KS6 and thus seem more affected by the intercalation process.

5.2.4.1 Details about anion intercalation in KS6

Mainly due to a larger signal-to-noise ratio for the data obtained for KS6 compared to Graphene AO-2, Figure 4.32 and Figure 4.34, respectively, more details about the intercalation process could be revealed for KS6.

Anion intercalation was clearly indicated by the replacement of the initial peak by a double peak, corresponding to a voltage of 4.78 V vs. Li^+/Li. In the previous study of graphite in EMS by Seel and Dahn [11], they observed a stage phase starting to form at 4.84 V vs. Li^+/Li due to the appearance of a new diffraction peak in the XRD spectra. This peak also corresponded to the two-phase region in the differential capacity curve, obtained from the galvanostatic cycling. Likewise, the formation of staged phases started to appear at a

voltage of 4.83 V vs. Li^+/Li for KS6. While KS6 obtained a stage index 4 at 4.91 V vs. Li^+/Li, while Seel and Dahn [11] reported a stage 4 at 4.8 V vs. Li^+/Li for graphite in cycled in EC/DEC 3 M $LiPF_6$ and the appearance of a stage 3 at 5.0 V vs. Li^+/Li.

In the first cycle at fully charge, KS6 obtained a stage index of 3.29, see Table 4.9. A much lower stage index was obtained in the system with graphite exposed to EMS based electrolyte, corresponding to a stage 2 at 5.55 V vs. Li^+/Li. The various stage indexes reflects the different charge capacity values obtained in the two systems; 61 $mAhg^{-1}$ for KS6 and 140 $mAhg^{-1}$ for graphite cycled inn EMS. As mentioned in section 5.2.2, there is reason to believe that the charge capacities measured for KS6 could be increased to some extent by defining the anodic cut-off voltage to a value larger than 5.0 V vs. Li^+/Li. However, a capacity of 140 $mAhg^{-1}$ is thus not expected, since EC/DMC based electrolytes will decompose at lower potentials than EMS; sulfone based electrolytes have shown to obtain oxidation potentials around 5.5 V vs. Li^+/Li [1].

5.2.4.2 Kapton electrodes

This section provide observations which are related to the practical implementation of the *in situ* XRD measurements, using the *in situ* XRD cell described in section 3.4.3, rather than being essential for understanding the behavior of the carbon materials.

Comparison of the two types of kapton electrodes being used in the *in situ* XRD cell, information provided in Table 4.8, clearly show a difference in both electrode characteristic and cycling behavior. The electrode cast onto gold coated kapton shows a much lower 1^{st} charge capacity relative to the two other cycled electrodes, consisting of a kapton/carbon film conductive film as current collector. However, since the specific discharge capacity is observed to be almost identical for the three electrodes, the most likely explanation for this significantly large difference in 1^{st} charge capacity is related to the current collector material.

Small parts of the current collector is exposed to the electrolyte, and there is reason to believe that the conductive carbon layer becomes electrochemically active upon cycling. *In situ* XRD analysis of kapton/carbon material only (the results are not included in this report) revealed no changes in the XRD spectra related to the d_{002} spacing. In contrast, a shift in peak position corresponding to the (002) planes in an electrode consisting of the same

current collector material and KS6 was observed. These observations clearly indicate that the conductive carbon layer in the current collector material becomes electrochemical active towards electrolyte oxidation, also explaining the large charge capacity in the initial cycle. For eventually further *in situ* XRD measurements, these findings need to be taken into consideration in order to obtain more reliable results.

5.2.5 Scanning electron microscopy

Anions do only partly deintercalate the carbon structures of KS6 and Graphene AO-2 upon cycling at high voltages. Compared to the observations of exfoliation in the work of Märkle et al. [10], the presented micrographs, Figure 4.37, did not shown any sign of structural degradation. However, since the XRD results revealed a significantly change in peak shape at discharge, in particular for Graphene AO-2, there is reason to believe that both materials are subjected to structural degradation. These changes are thus in such small range that they are not observable with the SEM microscope applied.

However, the micrographs presented, Figure 4.37, also revealed the presence of electrolyte decomposition products on KS6 and Graphene AO-2, appearing on both on basal plane and edge plane. However, the micrographs cannot give any indication of the extent of electrolyte decomposition, since both electrodes was washed with DMC prior analysis. Observations of these spherical white particles on the surface, similar to what was observed by Märkle et al. [7], only confirm the electrolyte decomposition as one of the high-voltage processes.

5.3 Various electrolyte compositions

The stability of Graphene AO-2, KS6 and Super P Li operating in various electrolyte compositions will be discussed below.

5.3.1 Graphene AO-2

As Table 4.2 clearly shows, the Graphene AO-2 electrodes vary in thickness, but have similar pore fraction and density. There is reason to believe that this difference is the cause

to the lower discharge capacities obtained for the system using the thick Graphene AO-2 electrode. Increased thickness of electrode leads to a larger distance for the anions to diffuse in the porous electrodes, thus preventing full utilization of the electrode. On the other hand, in the discussion of differences in behavior of Super P Li electrodes, possessing the same values of thickness, loading and pore fraction, the importance of electrode structure on the cycling behavior was emphasized, section 5.2.2 and 5.2.3. Both of the above mentioned observations state how largely dependent the carbon material behavior is on the electrode.

Taking into consideration how the electrode thickness affects the measured capacity values, only systems using the similar electrode were selected in order to determine the effect of the anion receptor on the galvanostatic cycling behavior. The capacity diagrams, Figure 4.9 vs. Figure 4.14, and Figure 4.12 vs. Figure 4.17, did not show any changes in cycling behavior upon adding of THFIPB. However, the oxidation potential determined for the three cell systems, Figure 4.29, reveal a slight increase in the electrolyte stability window. The increased oxidation potential for electrolyte 1:1 vol% EC/DMC 1 M $LiPF_6$ can be explained by the relatively higher concentration of EC, making it more viscous and thus reducing the ion mobility. In contrast to the galvanostatic cycling, electrodes with different thickness were used, and the observable shift in oxidation potential might be explained by this electrode difference, which does influence on the current and voltage. However, the improvement of the system stability upon adding anion receptor might be related to the formation of an anion-anion receptor complex, thus increasing the overpotential towards anion intercalation.

5.3.2 KS6 and Super P Li

Comparison of the electrode characteristics for KS6 electrodes show no significant differences, Table 4.2, making the comparison less challenging. However, the results from both galvanostatic cycling and testing by CV did not reveal any large differences in the electrode behavior.

In contrast, the cycled Super P Li electrodes obtain slightly different properties, Table 4.2. There is not observed any significant changes in either capacity value, reversibility or electrolyte stability upon adding THFIPB to the electrolyte, relative to cycling in an electrolyte with the composition of 30:70 vol% EC/DMC 1 M $LiPF_6$. However, in the research field on anion receptors, an improvement of the anode is reported, described in

section 2.2.1.3. Since the operation of Super P Li neither gets improved or worsened by adding THFIPB to the electrolyte, in a practical Li-ion battery the anion receptor will thus contribute to an improvement of the total cell performance.

5.4 Additional remarks

The comparison of behavior of KS6, Graphene AO-2 and Super P Li operating at high-voltages, is based on the observations from the cycling of pure carbon electrodes. In a real Li-ion battery cathode, the carbon needs to cooperate with the active material, described in detail in section 2.2.4. This could possibly result in a different behavior of the conductive carbon additive compared to what have been observed in this study.

However, there is another battery technology that use pure carbon electrode as both anode and cathode, the dual-carbon cell. While the current SOA Li-ion battery only intercalates Li^+-ions, the operation of a dual-carbon cell rely on the intercalation of cations in the negative electrode and anions in the positive, upon charging. In a cell system consisting of the electrolyte salt, $LiPF_6$, the charge stored in the positive electrode is dependent on the intercalation of PF_6^--ions in the carbon structure. There is some studies available related to research in the field of dual-carbon cells [11, 43, 76, 77], and very recently a company announced their plans of commercialize this battery technology [78]. The results obtained in this work might not only be of importance in the development of the high-voltage Li-ion batteries, but also in the development of the dual-carbon cell.

6 Conclusions

In this work, three candidate materials as conductive carbon additives in high-voltage Li-ion battery cathodes were investigated by electrochemical techniques. The materials included in the study were the commercially available conductive additives, fine graphite powder, KS6 and carbon black Super P Li. In addition, the multilayer graphene powder, Graphene AO-2 was investigated.

The powder characterization suggested that Graphene AO-2 contains graphitic particles rather than multilayer graphene. The particle size was observed to appear more flaky with a wide particle size distribution. Super P Li was confirmed to be a carbon black type of carbon, with small particle size and larger interlayer spacing, relative to graphite.

The results from galvanostatic cycling and cyclic voltammetry clearly show that all three studied carbon conductive additives become electrochemically active upon high-voltage cycling; subject to both electrolyte oxidation and anion intercalation. In combination with the most extensively studied electrolyte composition, 30:70 vol% EC/DMC 1 M $LiPF_6$, a direct relation between the measured specific capacities from cycling to 5.0 V vs. Li^+/Li, and the BET specific surface area and crystallinity of the carbon materials was observed. A larger BET surface area resulted in higher values of charge capacity, while the graphitic carbons had a higher discharge capacity. Upon continuous galvanostatic cycling at higher current densities, Super P Li displayed a small but stable discharge capacity, indicating reversible anion intercalation. According to the cyclic voltammograms recorded at even higher voltages, 5.5 V vs. Li^+/Li, the cathodic reduction peak appeared at very low voltages, around 1.78 V vs. Li^+/Li indicating high overpotential for anion deintercalation. However, for operation voltages below 4.7 V vs. Li^+/Li, Super P Li appears as the most stable conductive additive, due to a lower anodic current compared to KS6 and Graphene AO-2. With a cut-off voltage of 4.7 V vs. Li^+/Li, the Graphene AO-2 material displays better reversibility compared to KS6, with the anodic current mainly attributed to the anion intercalation. For operation at 5.5 V vs. Li^+/Li, the electrolyte oxidation process got more pronounced compared to cycling at 4.7 V vs. Li^+/Li, and both KS6 and Graphene AO-2 displayed rather poor reversibility.

In situ XRD results indicated only partly reversible anion intercalation for both KS6 and Graphene AO-2 when being cycled galvanostatically to a voltage of 5.0 V vs. Li^+/Li, and

less structural stability of Graphene AO-2 compared to KS6 was observed. The latter was also indicated by a significantly higher level of noise in the cyclic voltammograms for Graphene AO-2 with a cut-off voltage of 5.5 V vs. Li^+/Li. The *in situ* XRD results also showed the formation of staged phases in KS6 upon anion intercalation, starting at a voltage of 4.83 V vs. Li^+/Li. Intercalation in the initial cycle resulted in a stage index of 3.29 which corresponded to a discharge capacity of 27.8 $mAhg^{-1}$.

There were no observable improvements of either the stability of KS6 or Super P Li upon adding anion receptor to the electrolyte. However, a small increase in the electrolyte stability window was shown with the Graphene AO-2 electrode when changing to a more viscous electrolyte (1:1 vol% EC/DMC 1M $LiPF_6$) or adding anion receptor to the electrolyte.

7 Further work

The results from this study reveal some information about the carbon stability at high voltages. However, there are several more aspects of the carbon behavior that need to be considered and identified to obtain even deeper understanding of their operation at high potentials. Proposed work that can be conducted in order to improve or supplementing the testing methods used in this study, are stated below.

- The presented results clearly state the strong relationship between cycling results and electrode characteristics/structure. Improvement of electrode casting technique; varying slurry viscosity, thickness, and amount of binder, might give more comparable results.
- There are observed some variation in the results obtained for a given system and uncertainties in the measured data, indicated by relatively large values of standard deviations. Several more cells should be tested in order to check the reproducibility of the data and the cycling program should be improved to get more accuracy in the collected data.
- More detailed examination of the *in situ* XRD results, especially with respect to the peak shape observed at fully discharge. Conduct another *in situ* XRD experiment with Graphene AO-2 in order to increase the signal-to-noise ratio, which possible reveal more information about the anion intercalation process.
- Study the impedance evolution at different state of charge (SOC) and after several cycles by conducting electrochemical impedance spectroscopy (EIS). The results might reveal any changes in electrode impedance due to electrolyte oxidation products and exfoliation.
- Conduct additional high frequency EIS for a cell consisting of Graphene AO-2 electrode, in order to estimate the active electrode area. Compare with the estimated electrode areas for KS6 and Super P Li electrodes, might give some indication on the BET specific surface area for Graphnene AO-2.
- Use some chemical characterization techniques in order to study the electrolyte oxidation products deposited on the electrode surface upon cycling, to get a better understanding on how the carbon particles are affected; ionic and electric barrier.
- The results presented in this work are focusing on the initial cycles. The behavior of the three carbon materials might differ upon long-term cycling. Thus, it is important to conduct long-term cycling at constant current in order to investigate the behavior of the

three carbon materials, which corresponds to the operation of a practical rechargeable battery.

- Mix the various carbon materials with active cathode material to form a practical Li-ion battery cathode. Cycle these electrodes in order to observe the differences in behavior of the conductive carbon additive carbon in pure carbon electrodes and in combination with active material.
- Alternative to the point above, simulate the performance of a real composite cathode in order to study the conductive carbon network in a real electrode geometry using an inert active cathode material, e.g. like alumina powder used in the work of La Mantia et al. [38].

References

1. Hu M, Pang XL, Zhou Z. *Recent progress in high-voltage lithium ion batteries*. Journal of Power Sources. 2013;237:229-42.
2. Béguin F, Frackowiak Eb. *Carbons for electrochemical energy storage and conversion systems*. Boca Raton: CRC Press; 2010. xii, 517 s. : ill p.
3. Tarascon JM, Armand M. *Issues and challenges facing rechargeable lithium batteries*. Nature. 2001;414(6861):359-67.
4. Ogasawara T, Debart A, Holzapfel M, Novak P, Bruce PG. *Rechargeable Li2O2 electrode for lithium batteries*. Journal of the American Chemical Society. 2006;128(4):1390-3.
5. Scrosati B, Garche J. *Lithium batteries: Status, prospects and future*. Journal of Power Sources. 2010;195(9):2419-30.
6. Hamann CH, Hamnett A, Vielstich W. *Electrochemistry*. Weinheim: Wiley; 2007. XVIII, 531 s. : ill. p.
7. Markle W, Colin JF, Goers D, Spahr ME, Novak P. *In situ X-ray diffraction study of different graphites in a propylene carbonate based electrolyte at very positive potentials*. Electrochimica Acta. 2010;55(17):4964-9.
8. Li J, Klopsch R, Stan MC, Nowak S, Kunze M, Winter M, et al. *Synthesis and electrochemical performance of the high voltage cathode material Li Li0.2Mn0.56Ni0.16Co0.08 O-2 with improved rate capability*. Journal of Power Sources. 2011;196(10):4821-5.
9. Syzdek J, Marcinek M, Kostecki R. *Electrochemical activity of carbon blacks in LiPF6-based organic electrolytes*. Journal of Power Sources. 2014;245:739-44.
10. Markle W, Tran N, Goers D, Spahr ME, Novak P. *The influence of electrolyte and graphite type on the PF6- intercalation behaviour at high potentials*. Carbon. 2009;47(11):2727-32.
11. Seel JA, Dahn JR. *Electrochemical intercalation of PF6 into graphite*. Journal of the Electrochemical Society. 2000;147(3):892-8.
12. *When was the Battery Invented?* [06.12.2013]. Available from: http://batteryuniversity.com/learn/article/when_was_the_battery_invented.
13. *Li-ion cell* [21.11.2013]. Available from: http://research.chem.psu.edu/axsgroup/Ran/research/energystorage.html.
14. *Lithium-ion Batteries An Introduction* 2009 [31.08.2013]. Available from: http://www.agmbatteries.com/documents/Lithium-ion_technology.pdf.
15. Winter M, Besenhard JO, Spahr ME, Novak P. *Insertion electrode materials for rechargeable lithium batteries*. Advanced Materials. 1998;10(10):725-63.
16. Megahed S, Scrosati B. *LITHIUM-ION RECHARGEABLE BATTERIES*. Journal of Power Sources. 1994;51(1-2):79-104.
17. Dahn JR. *PHASE-DIAGRAM OF LIXC6*. Physical Review B. 1991;44(17):9170-7.
18. Mattson IR. *Stability of the Graphite Electrode for Li-ion Batteries*: Norwegian University of Science and Technology; 2013.
19. Sun X, Lee HS, Yang XQ, McBreen J. *A new additive for lithium battery electrolytes based on an alkyl borate compound*. Journal of the Electrochemical Society. 2002;149(3):A355-A9.
20. Xu K. *Nonaqueous liquid electrolytes for lithium-based rechargeable batteries*. Chemical Reviews. 2004;104(10):4303-417.
21. Peled E, Golodnitsky D, Ulus A, Yufit V. *Effect of carbon substrate on SEI composition and morphology*. Electrochimica Acta. 2004;50(2-3):391-5.
22. Aravindan V, Gnanaraj J, Madhavi S, Liu HK. *Lithium-Ion Conducting Electrolyte Salts for Lithium Batteries*. Chemistry-a European Journal. 2011;17(51):14326-46.
23. Zhang SS. *A review on electrolyte additives for lithium-ion batteries*. Journal of Power Sources. 2006;162(2):1379-94.

24. Qin Y, Chen ZH, Lee HS, Yang XQ, Amine K. *Effect of Anion Receptor Additives on Electrochemical Performance of Lithium-Ion Batteries*. Journal of Physical Chemistry C. 2010;114(35):15202-6.
25. Reddy VP, Blanco M, Bugga R. *Boron-based anion receptors in lithium-ion and metal-air batteries*. Journal of Power Sources. 2014;247:813-20.
26. Foss CEL. *Thermal stability and electrochemical performance of graphite anodes in Li-ion batteries*. Trondheim: Norges teknisk-naturvitenskapelige universitet; 2014. VIII, 139 s. : ill. p.
27. Etacheri V, Marom R, Elazari R, Salitra G, Aurbach D. *Challenges in the development of advanced Li-ion batteries: a review*. Energy & Environmental Science. 2011;4(9):3243-62.
28. Chung SY, Bloking JT, Chiang YM. *Electronically conductive phospho-olivines as lithium storage electrodes*. Nature Materials. 2002;1(2):123-8.
29. Chen YH, Wang CW, Liu G, Song XY, Battaglia VS, Sastry AM. *Selection of conductive additives in Li-ion battery cathodes - A numerical study*. Journal of the Electrochemical Society. 2007;154(10):A978-A86.
30. Zheng HH, Yang RZ, Liu G, Song XY, Battaglia VS. *Cooperation between Active Material, Polymeric Binder and Conductive Carbon Additive in Lithium Ion Battery Cathode*. Journal of Physical Chemistry C. 2012;116(7):4875-82.
31. Hong JK, Lee JH, Oh SM. *Effect of carbon additive on electrochemical performance of LiCoO2 composite cathodes*. Journal of Power Sources. 2002;111(1):90-6.
32. Zheng JM, Xiao J, Xu W, Chen XL, Gu M, Li XH, et al. *Surface and structural stabilities of carbon additives in high voltage lithium ion batteries*. Journal of Power Sources. 2013;227:211-7.
33. Inagaki M. *New carbons: control of structure and functions*. Amsterdam: Elsevier Science; 2000. 1 online resource (ix, 229 s.) : ill p.
34. Sørlie M, Øye HA. *Cathodes in aluminium electrolysis*. Düsseldorf: Aluminium-Verlag; 2010. X, 662 s. : ill. p.
35. Besenhard JO. *Handbook of battery materials*. Weinheim: Wiley-VCH; 1999. XXVI, 618 s. : ill. p.
36. *Morphology of carbon black* [15.06.2014]. Available from: https://www.tut.fi/ms/muo/vert/7_raw_materials_and_compounds/fillers_cb_morphology.htm.
37. *Carbon powders for Lithium battery systems* [16.12.2013]. Available from: http://www.timcal.com/scopi/group/timcal/timcal.nsf/pagesref/MCOA-7S6K2K/$File/Brochure_Carbon_Powders_for_Lithium_Battery_Systems.pdf.
38. La Mantia F, Huggins RA, Cui Y. *Oxidation processes on conducting carbon additives for lithium-ion batteries*. Journal of Applied Electrochemistry. 2013;43(1):1-7.
39. Cheon SE, Kwon CW, Kim DB, Hong SJ, Kim HT, Kim SW. *Effect of binary conductive agents in LiCoO2 cathode on performances of lithium ion polymer battery*. Electrochimica Acta. 2000;46(4):599-605.
40. Spahr ME, Novak P, Haas O, Nesper R. *Cycling performance of novel lithium insertion electrode materials based on the Li-Ni-Mn-O system*. Journal of Power Sources. 1997;68(2):629-33.
41. Jiang RY, Cui CY, Ma HY. *Using graphene nanosheets as a conductive additive to enhance the rate performance of spinel LiMn2O4 cathode material*. Physical Chemistry Chemical Physics. 2013;15(17):6406-15.
42. Kucinskis G, Bajars G, Kleperis J. *Graphene in lithium ion battery cathode materials: A review*. Journal of Power Sources. 2013;240:66-79.
43. Ishihara T, Koga M, Matsumoto H, Yoshio M. *Electrochemical intercalation of hexafluorophosphate anion into various carbons for cathode of dual-carbon rechargeable battery*. Electrochemical and Solid State Letters. 2007;10(3):A74-A6.
44. Xu K, von Cresce A. *Interfacing electrolytes with electrodes in Li ion batteries*. Journal of Materials Chemistry. 2011;21(27):9849-64.
45. von Cresce A, Xu K. *Electrolyte Additive in Support of 5 V Li Ion Chemistry*. Journal of the Electrochemical Society. 2011;158(3):A337-A42.

46. Goodenough JB, Kim Y. *Challenges for Rechargeable Li Batteries*. Chemistry of Materials. 2010;22(3):587-603.
47. Joho F, Novak P. *SNIFTIRS investigation of the oxidative decomposition of organic-carbonate-based electrolytes for lithium-ion cells*. Electrochimica Acta. 2000;45(21):3589-99.
48. Xing LD, Li WS, Wang CY, Gu FL, Xu MQ, Tan CL, et al. *Theoretical Investigations on Oxidative Stability of Solvents and Oxidative Decomposition Mechanism of Ethylene Carbonate for Lithium Ion Battery Use*. Journal of Physical Chemistry B. 2009;113(52):16596-602.
49. Yang L, Ravdel B, Lucht BL. *Electrolyte Reactions with the Surface of High Voltage LiNi0.5Mn1.5O4 Cathodes for Lithium-Ion Batteries*. Electrochemical and Solid State Letters. 2010;13(8):A95-A7.
50. Xu W, Chen XL, Ding F, Xiao J, Wang DY, Pan AQ, et al. *Reinvestigation on the state-of-the-art nonaqueous carbonate electrolytes for 5 V Li-ion battery applications*. Journal of Power Sources. 2012;213:304-16.
51. Kerlau M, Kostecki R. *Interfacial impedance study of Li-ion composite cathodes during aging at elevated temperatures*. Journal of the Electrochemical Society. 2006;153(9):A1644-A8.
52. Kerlau M, Reimer JA, Cairns EJ. *Layered nickel oxide-based cathodes for lithium cells: Analysis of performance loss mechanisms*. Journal of the Electrochemical Society. 2005;152(8):A1629-A32.
53. Orazem ME, Tribollet B. *Electrochemical impedance spectroscopy*. Hoboken, N.J.: Wiley; 2008. xxxi, 523 s. : ill p.
54. *AC impedance in electrochemical systems*. 2013.
55. Harrington DA. *Electrochemical Impedance Spectroscopy*. 2004.
56. *Basics of Electrochemical Impedance Spectroscopy*: Gamry Instrument; [cited 30.06.2014]. Available from: http://www.gamry.com/application-notes/basics-of-electrochemical-impedance-spectroscopy/.
57. Tennyson W. *X-ray Diffraction - The Basics Followed by a few examples of Data Analysis*.
58. Callister WD, Rethwisch DG. *Materials science and engineering*. Hoboken, N.J.: Wiley; 2011. XXIII, 885, [81] s. : ill. p.
59. Connolly JR. *Introduction Quantitative X-Ray Diffraction Methods*. 2009.
60. Tolchard. J.R.; Grand T. *TMT4166 Powder X-Ray Diffraction (XRD)*. 2013.
61. Iwashita N, Park CR, Fujimoto H, Shiraishi M, Inagaki M. *Specification for a standard procedure of X-ray diffraction measurements on carbon materials*. Carbon. 2004;42(4):701-14.
62. Buqa H, Wursig A, Goers A, Hardwick LJ, Holzapfel M, Novak P, et al. *Behaviour of highly crystalline graphites in lithium-ion cells with propylene carbonate containing electrolytes*. Journal of Power Sources. 2005;146(1-2):134-41.
63. *Graphene Nanopowder* [16.12.2013]. Available from: https://graphene-supermarket.com/Graphene-Nanopowder-8-nm-Flakes-25-g.html.
64. *Electrochemical Test Cell ECC-Ref* [02.06.2014]. Available from: http://el-cell.com/wp-content/uploads/manuals/ECC_REF_manual.pdf.
65. Zhou HT, Einarsrud MA, Vullum-Bruer F. *In situ X-ray diffraction and electrochemical impedance spectroscopy of a nanoporous Li2FeSiO4/C cathode during the initial charge/discharge cycle of a Li-ion battery*. Journal of Power Sources. 2013;238:478-84.
66. Leriche JB, Hamelet S, Shu J, Morcrette M, Masquelier C, Ouvrard G, et al. *An Electrochemical Cell for Operando Study of Lithium Batteries Using Synchrotron Radiation*. Journal of the Electrochemical Society. 2010;157(5):A606-A10.
67. Zhou H. *Nanostructured cathode materials for Li-ion batteries*. Trondheim: Norges teknisk-naturvitenskapelige universitet; 2013. VI, 151 s. : ill. p.
68. Lide DR. *CRC handbook of chemistry and physics: a ready-reference book of chemical and physical data*. Boca Raton, Fla.: Taylor & Francis; 2005. 1 b. (flere pag.) : fig. p.
69. *Poly(vinylidene fluoride)* Sigma-Aldrich [28.06.2014]. Available from: http://www.sigmaaldrich.com/catalog/product/aldrich/182702?lang=en&region=NO.
70. Laheaar A, Kurig H, Janes A, Lust E. *LiPF6 based ethylene carbonate-dimethyl carbonate electrolyte for high power density electrical double layer capacitor*. Electrochimica Acta. 2009;54(19):4587-94.

71. Nilssen BE. *Stability of Conductive Carbon Additive in high Voltage Lithium Ion Battery* Norwegian University of Science and Technology; 2013.
72. Tuinstra F, Koenig JL. *RAMAN SPECTRUM OF GRAPHITE*. Journal of Chemical Physics. 1970;53(3):1126-&.
73. Sætnan M. *Investigation of Routes for Improving the Rate Capability of Electrodes in Li-ion Batteries*: Norwegian University of Science and Technology; 2014.
74. Cui P, Lee J, Hwang E, Lee H. *One-pot reduction of graphene oxide at subzero temperatures*. Chemical Communications. 2011;47(45):12370-2.
75. Lian PC, Zhu XF, Liang SZ, Li Z, Yang WS, Wang HH. *Large reversible capacity of high quality graphene sheets as an anode material for lithium-ion batteries*. Electrochimica Acta. 2010;55(12):3909-14.
76. Carlin RT, Delong HC, Fuller J, Trulove PC. *DUAL INTERCALATING MOLTEN ELECTROLYTE BATTERIES*. Journal of the Electrochemical Society. 1994;141(7):L73-L6.
77. Santhanam R, Noel M. *Electrochemical intercalation of cationic and anionic species from a lithium perchlorate-propylene carbonate system - a rocking-chair type of dual-intercalation system*. Journal of Power Sources. 1998;76(2):147-52.
78. *Path to market* PowerJapan Plus [23.06.2014]. Available from: http://powerjapanplus.com/battery/market/.
79. *Ethylene carbonate* Sigma-Aldrich [20.06.2014]. Available from: http://www.sigmaaldrich.com/catalog/product/sial/676802?lang=en&region=NO.
80. *Dimethyl carbonate* Sigma-Aldrich [20.06.2014]. Available from: http://www.sigmaaldrich.com/catalog/product/sial/517127?lang=en&region=NO.
81. *Lithium hexafluorophosphate* Sigma-Aldrich; [20.06.2014]. Available from: http://www.sigmaaldrich.com/catalog/product/aldrich/201146?lang=en&region=NO.

Appendix A Slurry preparation

All electrode casts were prepared with the same concentration: 90 wt% carbon powder and 10 wt% binder. In the slurry preparation, different amounts of solvent were added in order to obtain right slurry viscosity. An overview of the exact amounts of carbon, binder and solvent used for the different electrode slurries are provided in Table A.1. Obtaining the right viscosity is the most critical part of the preparation and playing with the amount of solvent was necessary to get a slurry characterized by "only slightly moving in the beaker". As described in section 3.2, the procedure consists of several steps where the purpose of planetary milling is to obtain a homogeneously mixed slurry. Some of the prepared slurries were too viscous after this mixing step, and more solvent needed to be added to the slurry transferred from the Al_2O_3 jar. Based on this, the exact amounts of solvent are given as two separate values. Since several slurries were prepared, attempts were made in order to avoid adding extra solvent to the slurry after planetary milling, and hence probably obtain a more homogenously mixed slurry.

Assuming the ratio between carbon powder, binder and solvent is the same in the Al_2O_3 jar used for planetary milling, and the slurry transferred from the jar. The expected total amount of solvent needed to obtain the right viscosity right after planetary milling, of a slurry containing the given amounts of carbon powder and binder, was calculated based on the amount of extra solvent added to the slurry transferred from the jar. These values are also included in Table A.1.

Table A.1: Overview of the actual amounts of carbon powder, PVDF binder, NMP solvent added to the slurry before and after planetary milling, in order to obtain an electrode slurry with the right viscosity.

		Carbon powder [g]	**PVDF [g]**	**NMP before planetary milling [g]**	**Slurry transferred to Erlendmeyer flask [g]**	**NMP after planetary milling [g]**	**Expected amount NMP before planetary milling [g]**
KS6	*Cast 1*	5.00	0.5550	13.01	-	-	13.01
	Cast 2	10.00	1.1110	23.00	24.23	1.00	(23.00+1.41 =) 24.41
	Cast 3	10.00	1.1112	25.16	-	-	25.16
Graphene AO-2	*Cast 1*	5.00	0.5554	13.50	14.85	6.86	(13.50+8.80 =) 22.30
Super P Li	*Cast 1*	5.01	0.5564	50.10	47.3	20.8	(50.10+24.47 =) 74.57
	Cast 2	5.00	0.5550	65.00	60.62	7.08	(65.00+8.24 =) 73.24
	Cast 3	3.01	0.3334	40.31	-	-	40.31

Appendix B Electrolyte preparation

Different electrolytes were prepared and an overview is given in Table 3.2. The amounts needed of each electrolyte component to obtain the wanted composition were calculated using equation (B.1) – (B.2), based on the values in Table B.1. For the electrolyte preparation, the different amounts mixed are given Table B.2.

$$V_{tot.\mathrm{sol.}} = V_{EC} + V_{DMC} = \frac{m_{EC}}{\rho_{EC}} + \frac{m_{DMC}}{\rho_{DMC}} = 0.3V_{tot.\mathrm{sol.}} + 0.7V_{tot.\mathrm{sol.}} \quad \text{(B.1)}$$

$$m_{LiPF_6} = \left(\frac{M_{m,LiPF_6} C_{LiPF_6} V_{tot.sol.}}{1 - \left(C_{LiPF_6} M_{m,LiPF_6} / \rho_{LiPF_6} \right)} \right) \quad \text{(B.2)}$$

Table B.1: Physical data for EC, DMC and $LiPF_6$.

Parameter	
Density EC (ρ_{EC})	1.321 gcm^{-3} [79]
Density DMC (ρ_{DMC})	1.069 gcm^{-3} [80]
Density $LiPF_6$ (ρ_{LiPF6})	1.5 gcm^{-3} [81]
Molar mass $LiPF_6$ ($M_{m,LiPF6}$)	151.9 $gmol^{-1}$ [81]

Table B.2: Overview of the actual amounts of EC, DMC, $LiPF_6$, and THFIPB mixed in order to obtain the defined electrolyte composition.

Electrolyte number	**EC [g]**	**DMC [g]**	**$LiPF_6$ [g]**	**THFIPB [g]**
30/70 nr 1	1.1889	2.2449	0.5070	-
30/70 nr 2	2.3778	4.4898	1.0140	-
30/70 nr 3	1.1889	2.2449	0.5070	-
AR30/70 nr 1	5.0 (total amount of EC+DMC+$LiPF_6$)			0.0505
AR1/1 nr 1	5.0 (total amount of EC+DMC+$LiPF_6$)			0.0505

Appendix C Data fit X-ray diffraction spectra

In order to obtain peak positions and values for FWHM from XRD spectra, TOPAS software was used to fit the raw data obtained during the XRD analysis. The curve fit along with raw data and the difference between the two curves are provided in Figure C.1 - Figure C.3 and Figure C.4 - Figure C.8 for carbon powder characterization and *in situ* XRD measurements, respectively.

Carbon powder characterization

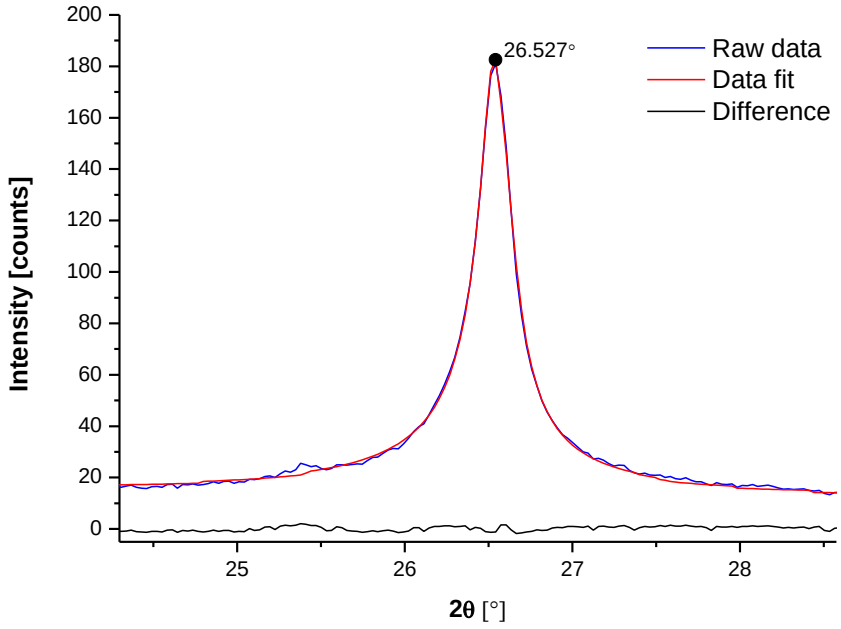

Figure C.1: XRD spectra obtained for KS6 powder (blue) displayed together with the fit curve (red) and the difference (black). Peak position and value are indicated in the curve.

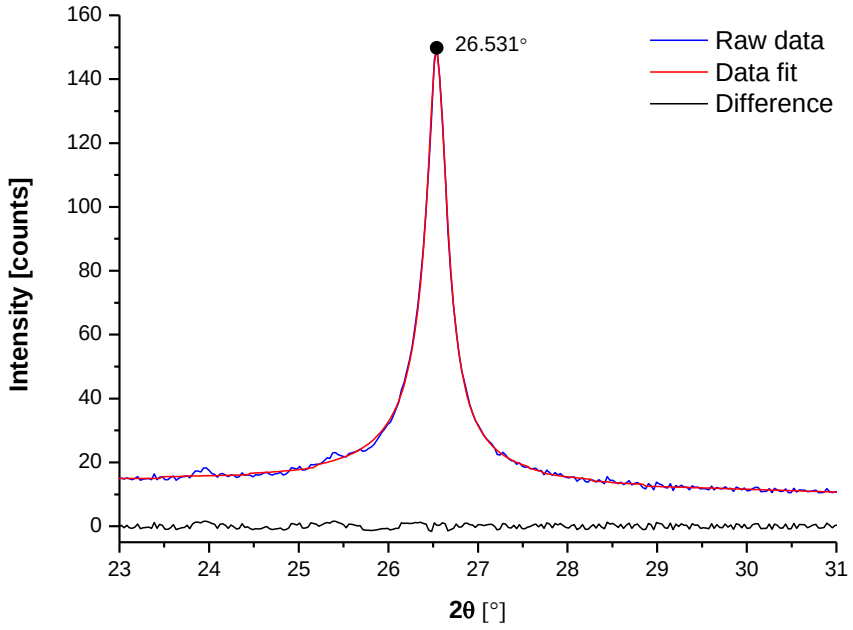

Figure C.2: XRD spectra obtained for Graphene AO-2 powder (blue) displayed together with the fit curve (red) and the difference (black). Peak position and value are indicated in the curve.

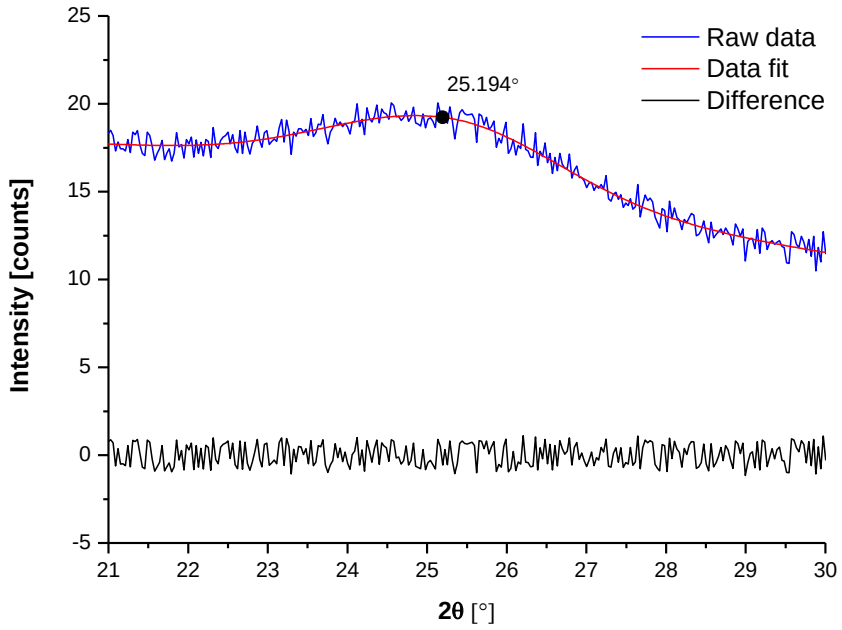

Figure C.3: XRD spectra obtained for Super P Li powder (blue) displayed together with the fit curve (red) and the difference (black). Peak position and value are indicated in the curve.

In situ XRD spectra

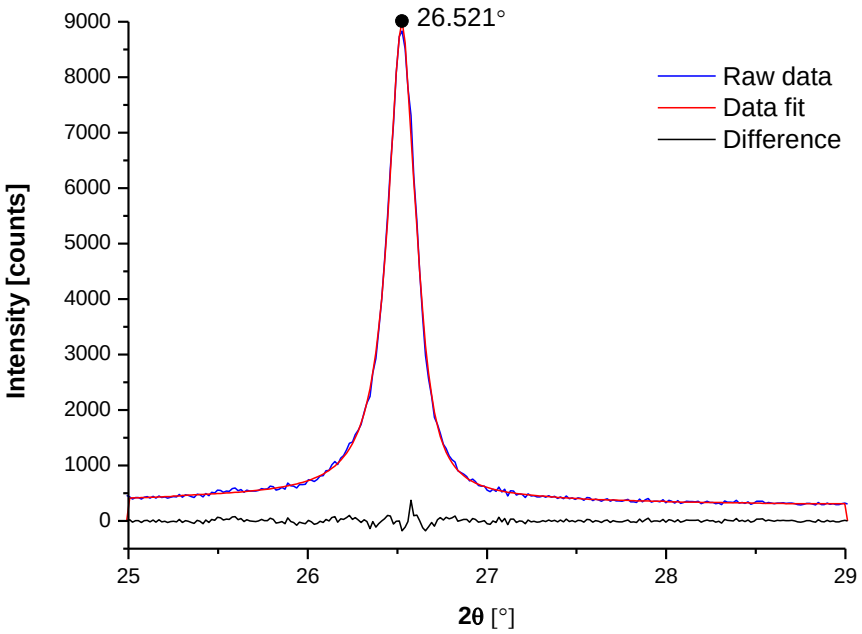

Figure C.4: XRD spectra for scan 1 (1-50) obtained for KS6 (blue) displayed together with the fit curve (red) and the difference (black). Peak position and value are indicated in the curve.

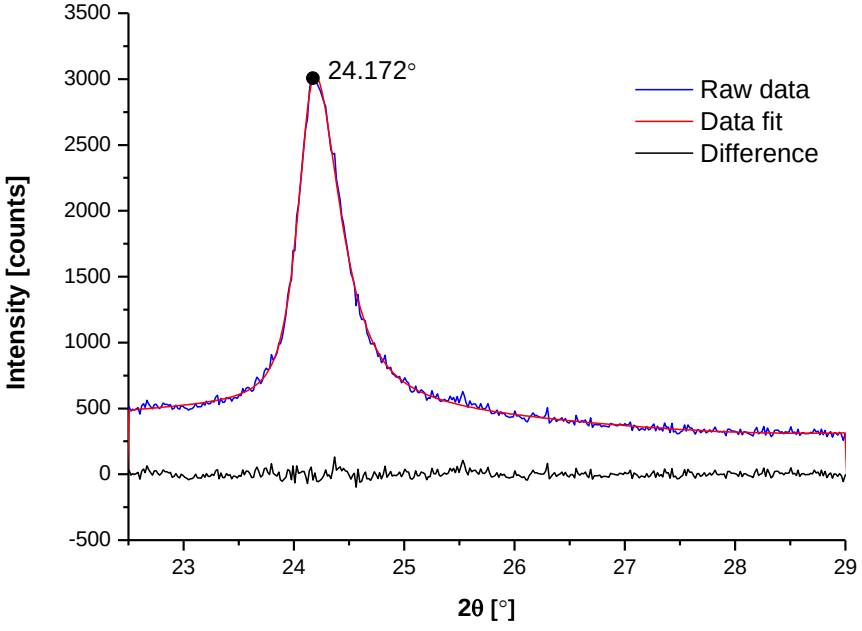

Figure C.5: XRD spectra for scan 29 (151-200), at scattering angles equal (002) planes obtained for KS6 (blue) displayed together with the fit curve (red) and the difference (black). Peak position and value are indicated in the curve.

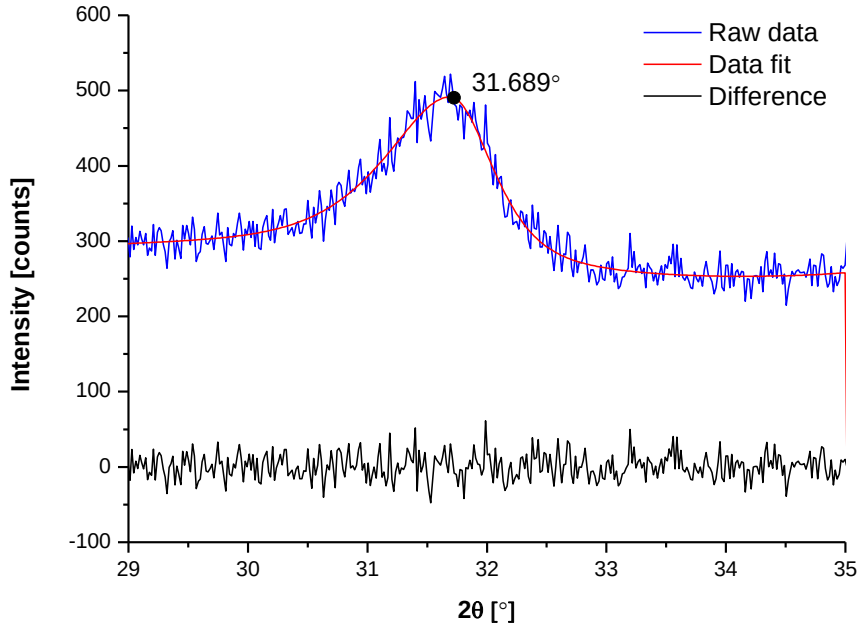

Figure C.6: XRD spectra for scan 29 (151-200), at scattering angles corresponding to diffraction peak related to stage intercalation obtained for KS6 (blue) displayed together with the fit curve (red) and the difference (black). Peak position and value are indicated in the curve.

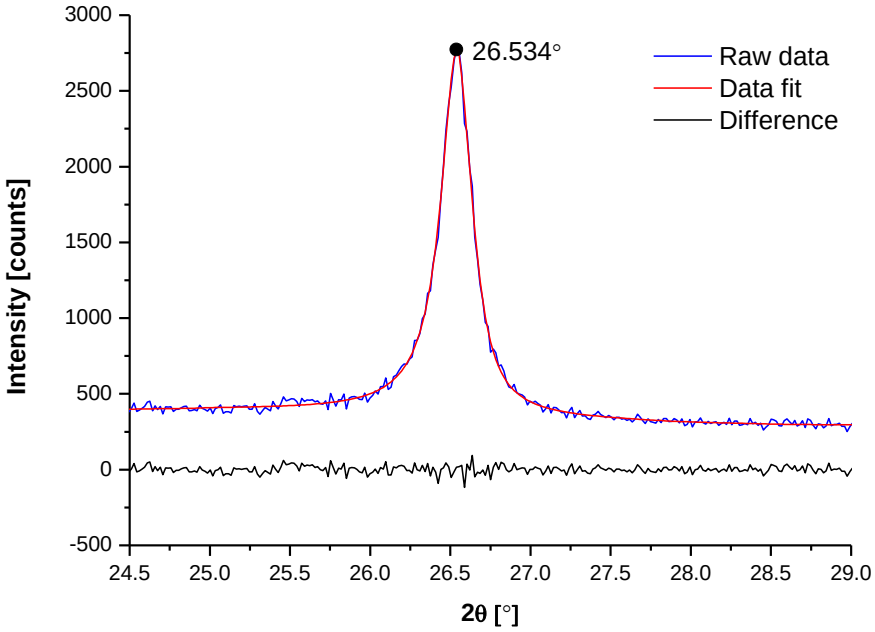

Figure C.7: XRD spectra for scan 1 (1-50) obtained for Graphene AO-2 (blue) displayed together with the fit curve (red) and the difference (black). Peak position and value are indicated in the curve.

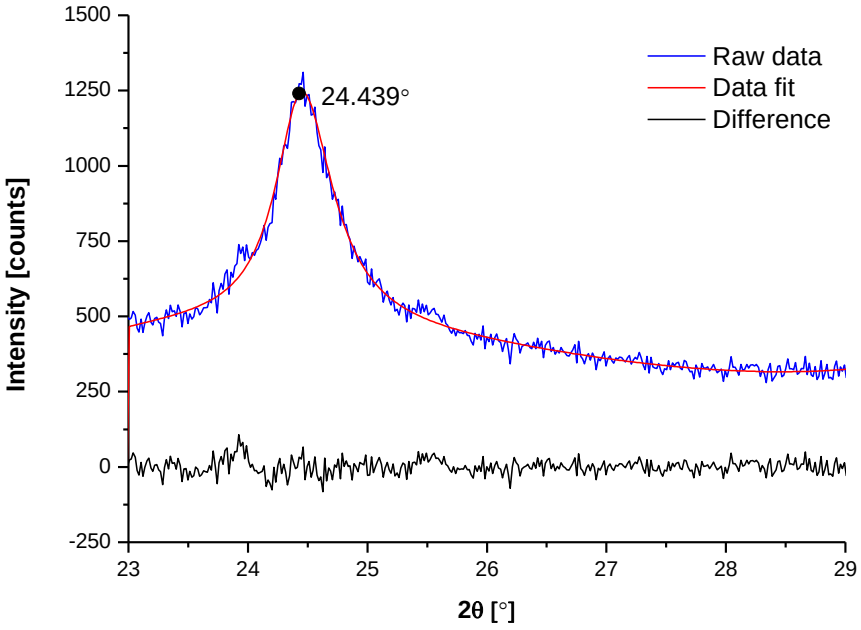

Figure C.8: XRD spectra for scan 29 (151-200) obtained for Graphene AO-2 (blue) displayed together with the fit curve (red) and the difference (black). Peak position and value are indicated in the curve.

Appendix D Curve smoothing – cyclic voltammograms

CV curves obtained using Parstat 4000 potentiostat were smoothed using Kalman filter, due to too large signal to noise ratio. Both raw data and the corresponding smoothed curve for 1st cycle are provided in Figure D.1 - Figure D.3.

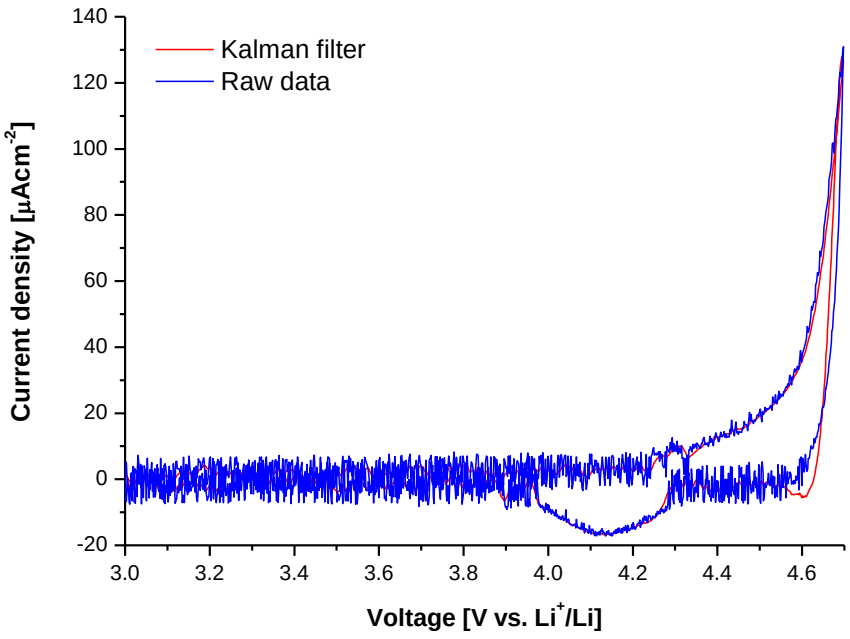

Figure D.1: Cyclic voltammograms providing the 1st cycle of Graphene AO-2 exposed to 30:70 vol% EC/DMC 1 M $LiPF_6$ (cell AO-2_30/70_2) based on the raw data (blue) and the smoothed curve using Kalman filter (red).

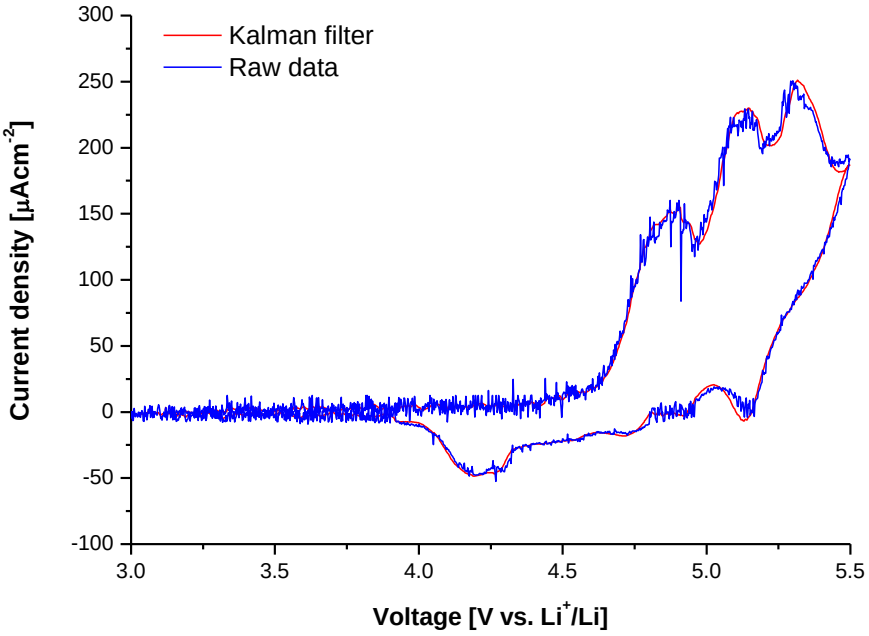

Figure D.2: Cyclic voltammograms providing the 1st cycle of Graphene AO-2 exposed to 30:70 vol% EC/DMC 1 M $LiPF_6$ 1 wt% THFIPB (cell AO-2_AR30/70_1) based on the raw data (blue) and the smoothed curve using Kalman filter (red).

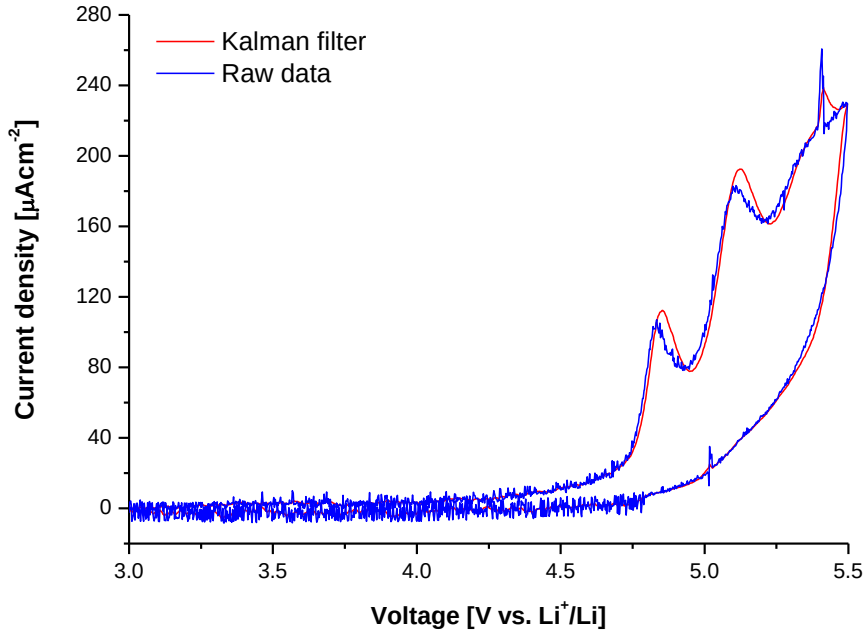

Figure D.3: Cyclic voltammograms providing the 1st cycle of Super P Li exposed to 30:70 vol% EC/DMC 1 M $LiPF_6$ 1 wt% THFIPB (cell SP_AR30/70_1) based on the raw data (blue) and the smoothed curve using Kalman filter (red).